# UNCOOLED THERMAL IMAGING

## Arrays, Systems, and Applications

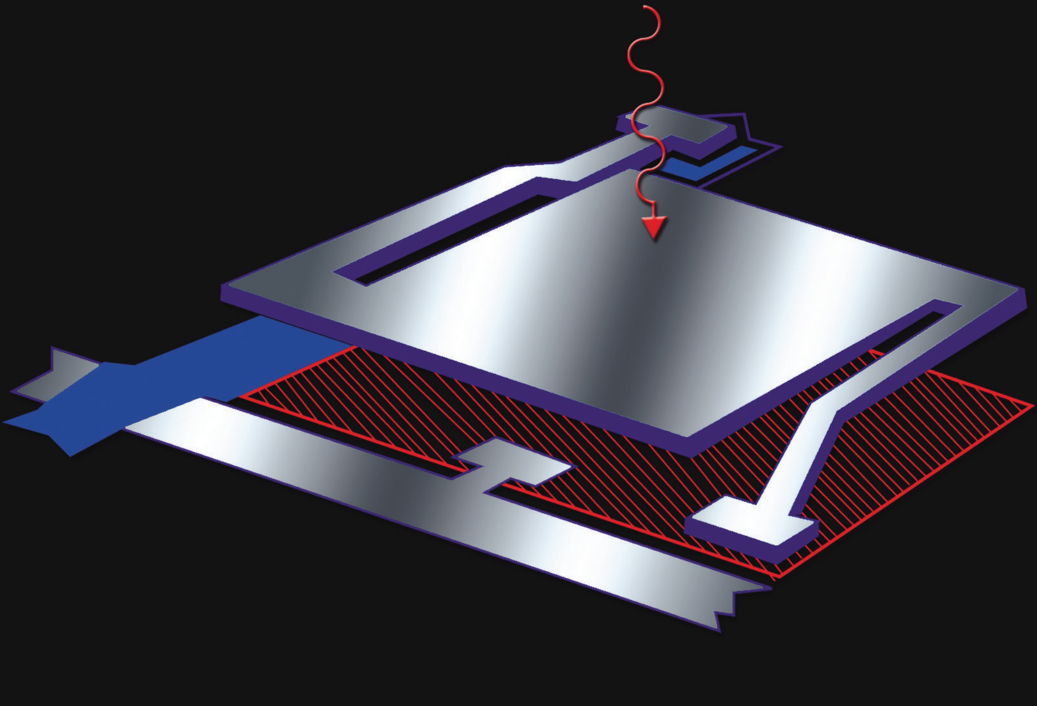

Paul W. Kruse

# UNCOOLED
# THERMAL IMAGING

## Arrays, Systems, and Applications

# Tutorial Texts Series

- *Uncooled Thermal Imaging Arrays, Systems, and Applications*, Paul W. Kruse, Vol. TT51
- *Fundamentals of Antennas*, Christos G. Christodoulou and Parveen Wahid, Vol. TT50
- *Basics of Spectroscopy*, David W. Ball, Vol. TT49
- *Optical Design Fundamentals for Infrared Systems*, *Second Edition*, Max J. Riedl, Vol. TT48
- *Resolution Enhancement Techniques in Optical Lithography*, Alfred Kwok-Kit Wong, Vol. TT47
- *Copper Interconnect Technology*, Christoph Steinbrüchel and Barry L. Chin, Vol. TT46
- *Optical Design for Visual Systems*, Bruce H. Walker, Vol. TT45
- *Fundamentals of Contamination Control*, Alan C. Tribble, Vol. TT44
- *Evolutionary Computation Principles and Practice for Signal Processing*, David Fogel, Vol. TT43
- *Infrared Optics and Zoom Lenses,* Allen Mann, Vol. TT42
- *Introduction to Adaptive Optics,* Robert K. Tyson, Vol. TT41
- *Fractal and Wavelet Image Compression Techniques,* Stephen Welstead, Vol. TT40
- *Analysis of Sampled Imaging Systems,* R. H. Vollmerhausen and R. G. Driggers, Vol. TT39
- *Tissue Optics Light Scattering Methods and Instruments for Medical Diagnosis*, Valery Tuchin, Vol. TT38
- *Fundamentos de Electro-Óptica para Ingenieros,* Glenn D. Boreman, translated by Javier Alda, Vol. TT37
- *Infrared Design Examples,* William L. Wolfe, Vol. TT36
- *Sensor and Data Fusion Concepts and Applications, Second Edition*, L. A. Klein, Vol. TT35
- *Practical Applications of Infrared Thermal Sensing and Imaging Equipment, Second Edition*, Herbert Kaplan, Vol. TT34
- *Fundamentals of Machine Vision*, Harley R. Myler, Vol. TT33
- *Design and Mounting of Prisms and Small Mirrors in Optical Instruments*, Paul R. Yoder, Jr., Vol. TT32
- *Basic Electro-Optics for Electrical Engineers,* Glenn D. Boreman, Vol. TT31
- *Optical Engineering Fundamentals,* Bruce H. Walker, Vol. TT30
- *Introduction to Radiometry,* William L. Wolfe, Vol. TT29
- *Lithography Process Control*, Harry J. Levinson, Vol. TT28
- *An Introduction to Interpretation of Graphic Images,* Sergey Ablameyko, Vol. TT27
- *Thermal Infrared Characterization of Ground Targets and Backgrounds,* P. Jacobs, Vol. TT26
- *Introduction to Imaging Spectrometers,* William L. Wolfe, Vol. TT25
- *Introduction to Infrared System Design,* William L. Wolfe, Vol. TT24
- *Introduction to Computer-based Imaging Systems,* D. Sinha, E. R. Dougherty, Vol. TT23
- *Optical Communication Receiver Design,* Stephen B. Alexander, Vol. TT22
- *Mounting Lenses in Optical Instruments,* Paul R. Yoder, Jr., Vol. TT21
- *Optical Design Fundamentals for Infrared Systems,* Max J. Riedl, Vol. TT20
- *An Introduction to Real-Time Imaging,* Edward R. Dougherty, Phillip A. Laplante, Vol. TT19
- *Introduction to Wavefront Sensors,* Joseph M. Geary, Vol. TT18
- *Integration of Lasers and Fiber Optics into Robotic Systems,* J. A. Marszalec, E. A. Marszalec, Vol. TT17
- *An Introduction to Nonlinear Image Processing,* E. R. Dougherty, J. Astola, Vol. TT16
- *Introduction to Optical Testing,* Joseph M. Geary, Vol. TT15
- *Image Formation in Low-Voltage Scanning Electron Microscopy,* L. Reimer, Vol. TT12
- *Diazonaphthoquinone-based Resists,* Ralph Dammel, Vol. TT11
- *Infrared Window and Dome Materials,* Daniel C. Harris, Vol. TT10
- *An Introduction to Morphological Image Processing,* Edward R. Dougherty, Vol. TT9
- *An Introduction to Optics in Computers,* Henri H. Arsenault, Yunlong Sheng, Vol. TT8
- *Digital Image Compression Techniques,* Majid Rabbani, Paul W. Jones, Vol. TT7
- *Aberration Theory Made Simple,* Virendra N. Mahajan, Vol. TT6
- *Single-Frequency Semiconductor Lasers,* Jens Buus, Vol. TT5

# UNCOOLED THERMAL IMAGING

## Arrays, Systems, and Applications

Paul W. Kruse

Tutorial Texts in Optical Engineering
Volume TT51

SPIE
PRESS

Bellingham, Washington  USA

Library of Congress Cataloging-in-Publication Data

Kruse, Paul W.
Uncooled thermal imaging arrays, systems and applications / Paul W. Kruse
p. cm. — (Tutorial texts in optical engineering ; v. TT 51)
Includes bibliographical references and index.
ISBN 0-8194-4122-8
1. Infrared imaging. 2. Thermography. 3. Imaging systems. I. Title. II. Series.

TA1570 .K78 2001
621.36'2—dc21 2001020471
CIP

Published by

SPIE—The International Society for Optical Engineering
P.O. Box 10
Bellingham, Washington 98227-0010
Phone: 360/676-3290
Fax: 360/647-1445
Email: spie@spie.org
WWW: www.spie.org

Copyright © 2001 The Society of Photo-Optical Instrumentation Engineers

All rights reserved. No part of this publication may be reproduced or distributed in any form or by any means without written permission of the publisher.

Printed in the United States of America.

Cover figure: Microbolometer pixel structure. From R. A. Wood, “Monolithic silicon microbolometer arrays,” Chapter 3 of *Uncooled Infrared Imaging Arrays and Systems, Semiconductors and Semimetals 47,* P. W. Kruse and D. D. Skatrud, eds., Academic Press, San Diego (1997). Used with premission.

# Introduction to the Series

The Tutorial Texts series was initiated in 1989 as a way to make the material presented in SPIE short courses available to those who couldn't attend and to provide a reference book for those who could. Typically, short course notes are developed with the thought in mind that supporting material will be presented verbally to complement the notes, which are generally written in summary form, highlight key technical topics, and are not intended as stand-alone documents. Additionally, the figures, tables, and other graphically formatted information included with the notes require further explanation given in the instructor's lecture. As stand-alone documents, short course notes do not generally serve the student or reader well.

Many of the Tutorial Texts have thus started as short course notes subsequently expanded into books. The goal of the series is to provide readers with books that cover focused technical interest areas in a tutorial fashion. What separates the books in this series from other technical monographs and textbooks is the way in which the material is presented. Keeping in mind the tutorial nature of the series, many of the topics presented in these texts are followed by detailed examples that further explain the concepts presented. Many pictures and illustrations are included with each text, and where appropriate tabular reference data are also included.

To date, the texts published in this series have encompassed a wide range of topics, from geometrical optics to optical detectors to image processing. Each proposal is evaluated to determine the relevance of the proposed topic. This initial reviewing process has been very helpful to authors in identifying, early in the writing process, the need for additional material or other changes in approach that serve to strengthen the text. Once a manuscript is completed, it is peer reviewed to ensure that chapters communicate accurately the essential ingredients of the processes and technologies under discussion.

During the past nine years, my predecessor, Donald C. O'Shea, has done an excellent job in building the Tutorial Texts series, which now numbers over fifty books. It has expanded to include not only texts developed by short course instructors but also those written by other topic experts. It is my goal to maintain the style and quality of books in the series, and to further expand the topic areas to include emerging as well as mature subjects in optics, photonics, and imaging.

*Arthur R. Weeks, Jr.*
*Invivo Research Inc. and University of Central Florida*

*This book is dedicated to my*
*wife, Margaret M. Kruse,*
*the mother of our nine children*
*and grandmother of sixteen.*

# Contents

**List of Figures xiii**

**List of Tables xv**

**Preface xvii**

## Chapter 1 An Overview of Uncooled Thermal Imaging Detection Mechanisms and Their Figures of Merit / 1

1.1 Terminology / 1
1.2 Detection Mechanisms / 2
    1.2.1 Photon detection mechanisms / 2
    1.2.2 Thermal detection mechanisms / 4
        1.2.2.1 Resistive bolometer / 4
        1.2.2.2 Pyroelectric effect / 5
        1.2.2.3 Field-enhanced pyroelectric effect/ferroelectric bolometer / 5
        1.2.2.4 Thermoelectric effect/radiation thermocouple / 5
    1.2.3 Wave interaction effects / 6
1.3 Figures of Merit / 6
    1.3.1 Responsivity / 7
    1.3.2 Noise equivalent power and D* / 7
    1.3.3 Noise equivalent temperature difference / 8
    1.3.4 Minimum resolvable temperature difference / 9
    1.3.5 Thermal response time / 9
References / 10

## Chapter 2 Fundamental Limits / 11

2.1 Introduction / 11
2.2 Photon Noise Limitations of Thermal Detectors / 12
2.3 Temperature Fluctuation Noise in Thermal Detectors / 14
2.4 Temperature Fluctuation Noise Limit to Focal Plane Array Performance / 20
2.5 Background Fluctuation Noise Limit to Focal Plane Array Performance / 20
2.6 Discussion / 22
References / 23

## Chapter 3 Thermoelectric Arrays / 25

3.1 Introduction / 25
3.2 The Heat Flow Equation / 27
3.3 Responsivity / 29
3.4 Noise / 30
3.5 D* / 30
3.6 Noise Equivalent Temperature Difference / 30
3.7 Pixel Design Optimization / 31
References / 32

**Chapter 4 Resistive Bolometers / 33**

4.1 Introduction / 33
4.2 Responsivity / 34
    4.2.1 Case I: No Joulean heating; constant bias / 34
    4.2.2 Case II: Joulean heating; constant bias / 35
    4.2.3 Case III: Joulean heating; pulsed bias / 40
4.3 Noise / 42
4.4 Noise Equivalent Temperature Difference / 44
4.5 Choice of Resistive Materials / 45
    4.5.1 Vanadium oxide / 45
    4.5.2 Amorphous silicon / 46
    4.5.3 Thermistor materials / 47
    4.5.4 Titanium / 47
    4.5.5 P-N junction diodes / 47
References / 48

**Chapter 5 Pyroelectric Arrays / 49**

5.1 Introduction / 49
5.2 The Heat Flow Equation / 51
5.3 Responsivity / 52
5.4 Johnson Noise / 54
5.5 Temperature Fluctuation Noise / 55
5.6 Noise Equivalent Temperature Difference / 55
References / 56

**Chapter 6 State of the Art and Technical Trends / 57**

6.1 Introduction / 57
6.2 Resistive Bolometer Arrays and Their Applications in Thermal Imagers and Imaging Radiometers / 57
    6.2.1 The Honeywell silicon microstructure resistive bolometer array and thermal imager / 57

    - 6.2.2 Improvements on the Honeywell VOx 240 × 332 pixel bolometer array / 63
        - 6.2.2.1 Increase in fill factor / 63
        - 6.2.2.2 CMOS ROIC / 63
        - 6.2.2.3 Smaller pixels / 63
        - 6.2.2.4 640 × 480 pixel arrays / 64
        - 6.2.2.5 160 × 120 pixel arrays / 64
        - 6.2.2.6 Removal of temperature stabilizer / 64
    - 6.2.3 Use of amorphous silicon rather than vanadium oxide as the resistive material / 64
    - 6.2.4 Use of diodes rather than resistive materials / 65
    - 6.2.5 Thermal imagers employing uncooled VOx bolometer arrays / 65
    - 6.2.6 Imaging radiometers based on 320 × 240 pixel uncooled VOx bolometers / 65
    - 6.2.7 Summary / 67
- 6.3 Pyroelectric and Ferroelectric Bolometer Uncooled Arrays and Thermal Imagers that Employ Them / 67
    - 6.3.1 Introduction / 67
    - 6.3.2 The Texas Instruments (now Raytheon) hybrid ferroelectric bolometer array and imagers / 68
    - 6.3.3 Monolithic pyroelectric array development / 72
- 6.4 Uncooled Thermoelectric Arrays and Thermal Imagers and Imaging Radiometers that Employ Them / 72
    - 6.4.1 Introduction / 72
    - 6.4.2 Monolithic linear arrays / 73
    - 6.4.3 Imaging radiometer employing linear thermoelectric arrays / 75
- 6.5 Status and Trends of Uncooled Arrays / 77
    - 6.5.1 Status and trends of uncooled arrays for military systems / 77
    - 6.5.2 Status and trends of commercial uncooled arrays and systems / 78

References / 79

**Chapter 7 Choosing the Proper Technical Approach for a Given Application / 83**

- 7.1 Introduction / 83
- 7.2 Thermal Imaging Applications / 83
- 7.3 Comparison of the Principal Types of Uncooled Thermal Detectors / 86

**Index / 89**

# List of Figures

**Figure 2-1.** Photon noise-limited D* of thermal detectors as a function of detector temperature $T_1$ and background temperature $T_2$. Viewing angle of 2π steradians and unit absorptivity. From P.W. Kruse, L.D. McGlauchlin, and R.B. McQuistan.[1]

**Figure 2-2.** Relative increase in background fluctuation noise limited $D^*_\lambda$ and $D^*(T)$ for photon and thermal detectors achieved by using cold aperture. From P.W. Kruse, L.D. McGlauchlin, and R.B. McQuistan.[1]

**Figure 2-3.** Temperature fluctuation noise limit and background fluctuation noise limit to NETD of uncooled and cryogenic thermal detector focal plane arrays as a function of thermal conductance $G$.

**Figure 2-4.** Dependence of $D^*_\lambda$ and $D^*(T_2)$ on long wavelength limit for thermal and photon detectors. From F.J. Low and A.R. Hoffman.[6]

**Figure 3-1.** Radiation thermocouple.

**Figure 3-2.** Monolithic thermoelectric pixel structure.

**Figure 3-3.** Monolithic thermoelectric pixel. From M.C. Foote.[2]

**Figure 4-1.** Microbolometer pixel structure. From R.A. Wood.[2]

**Figure 4-2.** Bolometer circuit.

**Figure 4-3.** Numerical calculations made assuming the parameters in Table 4-1 as discussed in the text. $G_e$, Effective value of thermal conductance of microbolometer to substrate. From R.A. Wood.[2]

**Figure 4-4.** Temperature coefficient of resistance (TCR) versus resistivity for thin films of mixed vanadium oxides. From R.A. Wood.[2]

**Figure 4-5.** Resistance versus temperature for thin films of mixed vanadium oxides. From R.A. Wood.[2]

**Figure 4-6.** Evolution of the TCR as a function of the electrical resistivity of a-Si. From Tissot.[5]

**Figure 5-1.** Ferroelectric monolithic array structure. From R.K. McEwen and P.A. Manning.[12]

**Figure 5-2.** Ferroelectric hybrid array structure. From R.K. McEwen and P.A. Manning.[12]

**Figure 5-3.** Pyroelectric detector responsivity as a function of frequency.

**Figure 6-1.** Illustration of one-level and two-level microbolometer designs. From R.A. Wood.[3]

**Figure 6-2.** Fabrication sequence for two-level microbolometers. From R.A. Wood.[3]

**Figure 6-3.** Construction of a sealed vacuum package for 240 × 336 microbolometer arrays. From R.A. Wood.[3]

**Figure 6-4.** Block diagram of Honeywell uncooled bolometer imager. From R. A. Wood.[3]

**Figure 6-5.** Measured NETD of 240 × 336 two-level microbolometer arrays of Table 6-1. From R.A. Wood.[3]

**Figure 6-6.** The pyroelectric effect.

**Figure 6-7.** Temperature dependence of spontaneous polarization and dielectric permittivity for ferroelectric ceramic barium strontium titanate (BST). From C. M. Hanson et al.[23]

**Figure 6-8.** Pyroelectric material responsivity figure of merit $[\partial E/\partial T)_D = p/\varepsilon\varepsilon_o]$ for a ceramic $Ba_{0\,67}Sr_{0\,33}TiO_3$ (barium strontium titanate) sample 25-μm thick, at two different bias voltages. From C. M. Hanson.[23]

**Figure 6-9.** The Texas Instruments (now Raytheon) hybrid ferroelectric bolometer array. From C. M. Hanson et al.[23]

**Figure 6-10.** Read-out integrated circuit for Texas Instruments (now Raytheon) hybrid ferroelectric array. From C. M. Hanson et al.[23]

**Figure 6-11.** Silicon microstructure monolithic pyroelectric array. From R. K. McEwen and P. A. Manning.[28]

**Figure 6-12.** Four types of uncooled thermopile arrays: (a) Array of type 1 thermopile devices. The 0.6-μm thick device membranes connect to the silicon substrate at the left and right sides. Each pixel has 11 Bi-Te/Bi-Sb-Te thermocouples in series. These long, thin devices were designed to geometrically match a spectrometer. (b) Array of type 2 thermopile devices. The 0.6-μm thick device membranes connect to the silicon substrate at the top and bottom. Each pixel has one Bi-Te/Bi-Sb-Te thermocouple. (c) Array of type 3 thermopile devices. The 0.6-μm thick device membranes connect to the silicon substrates at the top and bottom. Each pixel has five Bi-Te/Bi-Sb-Te thermocouples in series. (d) Array of type 4 thermopile devices. The 0.6-μm thick device membranes connect to the silicon substrate at the top and bottom. Each pixel has one Bi-Te/Bi-Sb-Te thermocouple. From M.C. Foote and E.W. Jones.[30]

**Figure 6-13.** Representative data from the literature showing reported D* values as a function of response time for thin-film thermopile linear arrays. Thermoelectric materials are Bi-Te/Bi-Sb-Te (this work) (ℓ), constantan/chromel (↔), and silicon (↵). The dashed line represents the Foote and Jones results. Its slope indicates D* proportional to the square root of response time, which is typical for thermopiles or bolometers with different geometries and the same material system. From M.C. Foote and E.W. Jones.[30] See Foote and Jones[30] for identification of the numbered data points.

# List of Tables

**Table 1-1.** Classes of infrared detectors.

**Table 3-1.** $Z$ values of thermoelectric junction pairs at 300 K. From M.C. Foote.[2]

**Table 4-1.** Assumed parameter values for Fig. 4-3. From R.A. Wood.[2]

**Table 6-1.** Summary of 240 × 336 two-level microbolometer array parameters. From R.A. Wood.[3]

**Table 6-2.** Summary of performance characteristics of AE-189 microbolometer FPA. From W. Radford et al.[7]

**Table 6-3.** Sanders Lockheed Martin LTC500 thermal imager technical specifications. From T. Breen et al.[16]

**Table 6-4.** Geometry and measured performance of four thermopile arrays shown in Figs. 6-12(a) through (d). From M.C. Foote and E.W. Jones.[30]

**Table 6-5.** Specifications of thermoelectric linear arrays employed in IR SnapShot® imaging radiometer. From P.W. Kruse.[32]

**Table 6-6.** IR SnapShot® imaging radiometer specifications.

**Table 6-7.** Status and trends of military uncooled arrays.

**Table 6-8.** Status and trends of commercial uncooled arrays.

**Table 7-1.** Thermal imaging applications.

**Table 7-2.** Comparison of principal types of uncooled thermal detectors.

# Preface

This SPIE Tutorial Text provides an introduction to the subject of uncooled infrared focal plane arrays and their applications. Like all Tutorial Texts, it is intended as an introduction to the subject for both professionals and students; it is not a comprehensive reference or academic textbook. It is a stand-alone version of the short course "Uncooled IR Focal Plane Arrays" which I have taught at SPIE meetings since 1995.

The term "infrared focal plane array" refers to an assemblage of individual infrared detector picture elements ("pixels") located at the focal plane of an infrared imaging system. Although the definition includes one-dimensional ("linear") arrays as well as two-dimensional arrays, it is frequently applied only to two-dimensional arrays. In this text, the term refers to both types.

The term "uncooled" refers to arrays that are operated without any type of cryogenic system. Thus they operate at the imaging system ambient temperature. If the ambient is unstated, it is assumed to be "room temperature," which refers to 295 K and is frequently rounded off to 300 K.

The development of uncooled infrared focal plane arrays can be traced to the military need to see the battlefield at night without the need for any form of illumination, whether from natural sources (moonlight, starlight, airglow) or from artificial sources. In the United States, it was the Vietnam War that caused the military services to initiate the development of infrared systems that could provide imagery arising from the thermal emission of terrain, vehicles, buildings, and people. The result was the Common Modular FLIR (Forward Looking InfraRed), the development of which was led by the U.S. Army Night Vision Laboratory (now the U.S. Army CECOM Night Vision and Electronic Sensors Directorate). The "Common Mod" FLIR employed a (Hg,Cd)Te (mercury cadmium telluride) linear array that required cooling to 77 K; the temperature of liquid nitrogen at 1 atmosphere pressure. Excellent imagery is obtainable with this FLIR, but it requires a cryogenic system (i.e., a refrigerator), and a mechanical system to scan the scene across the linear array to form a two-dimensional image.

The need for the scanner has been obviated by the development of two-dimensional focal plane arrays. In addition to (Hg,Cd)Te focal plane arrays, today there are many other types, such as InSb (indium antimonide), PtSi (platinum silicide), and GaAs/AlGaAs (gallium arsenide/aluminum gallium arsenide) QWIPs (quantum well imaging photodetectors). All require cryogenic operation, although some do not require cooling to as low as 77 K.

These cryogenic arrays employ photon detection, in which the absorption of an incident photon of sufficient energy frees an electron or hole or both to increase the electrical conductivity or to generate a voltage at a potential barrier internal to the material. However, there is another class of detection mechanism, known as thermal, in which the action of the incident radiation is to slightly increase the temperature of a material, which can be detected, for example, by a change in electrical conductivity (resistance bolometer), generation of a voltage (thermoelectric effect, thermocouple), or change in the electrical polarization (pyroelectric effect). These effects do not require cryogenic operation.

When compared on a pixel basis, uncooled thermal detector arrays in general have a much poorer signal-to-noise ratio than the cryogenic photon detector arrays. On the other hand, a staring detector array can have a much smaller system noise bandwidth than a scanning array. Because it is easier to prepare staring arrays employing uncooled thermal detectors than those employing cryogenic photon detectors, the disparity in performance between the two is reduced. This is especially true if both types are operated at the TV frame rate (30 Hz in the U.S.). Thermal detection mechanisms are generally slower than photon; both are designed to have little degradation in performance at 30 Hz.

The most intensive effort in the development of uncooled infrared imaging arrays and systems has been in the U.S. The initial efforts at Honeywell Technology Center on thin film resistive bolometer arrays and at that part of Texas Instruments that later was acquired by Raytheon on pyroelectric arrays and ferroelectric bolometer arrays began in the late 1970s and early 1980s. These efforts, which were funded by U.S. Army Communication Electronics Command (CECOM) Night Vision and Electronic Sensors Directorate (NVESD) and by Defense Advanced Research Projects Agency (DARPA), were initially under military security restrictions. The work became unclassified in 1992, revealing outstandingly successful efforts by both contractors. Since then the field has flourished; many organizations worldwide have entered the field.

The outline of the text is as follows: the first chapter describes in broad terms the principal uncooled thermal detection mechanisms and the figures of merit used to describe their performance. The second chapter describes the fundamental limits to their performance. It is so placed in order that the theoretical performance of the three most important detection mechanisms, namely, thermoelectric, resistive bolometric and pyroelectric—the subjects of Chapters 3, 4, and 5—can be compared against these fundamental limits.

The above chapters constitute the first of three parts of this text. All except chapter one are highly mathematical, directed toward the reader who is participating in the technical development of uncooled arrays. Chapter 6, the second part, is a state-of-the-art description of uncooled arrays and systems employing them. This information comes from journal articles and SPIE Proceedings; manufacturers' literature is not employed. It is of interest not only to the array developers both also to the user community. The final part, Chapter 7, describes applications and technical trends of uncooled arrays and systems employing them. It is of general interest.

I am greatly indebted to Mrs. Jan Jacobs for typing the manuscript, and to Dr. Marc C. Foote, Prof. William L. Wolfe, and Dr. R. Andrew Wood for their very helpful comments.

Paul W. Kruse
December, 2000

# Chapter 1

# An Overview of Uncooled Thermal Imaging Detection Mechanisms and Their Figures of Merit

## 1.1 Terminology

The subject of this book is uncooled thermal imaging focal plane arrays and systems. In this context, “uncooled” refers to not employing artificial means of reducing the temperature of the infrared array, such as by means of cryogenic solids or liquids, mechanical refrigerators, thermoelectric coolers, or Joule-Thomson coolers. The infrared array operates at the ambient temperature, whatever that might be. If unstated, the temperature is assumed to be “room temperature,” generally considered to be 295 K or 300 K. Some detection mechanisms require the use of temperature stabilizers upon which are mounted the thermal imaging arrays. Although their construction is similar to that of thermoelectric coolers, they maintain the array at or very near room temperature; thus they are not considered to be coolers.

The term “thermal imaging” refers to the ability of the array in its system to image room temperature scenes. Here again, “room temperature” implies 295 K or 300 K. A thermal image of a scene refers to an image of that scene made entirely by detecting the thermal (infrared) radiation emitted by everything in the scene. Thus there is no use of artificial (lamps, lasers) or natural (sunlight, moonlight, starlight, airglow) illumination of the scene. Because “room temperature” radiation has its spectral peak emittance at about 10-µm wavelength, this implies that the spectral response of the thermal imaging array extends beyond 3-µm wavelength; such arrays are usually designed to operate in the 3–5-µm or 8–14-µm atmospheric windows.

The term “focal plane array” as used herein includes not only linear arrays of pixels but also two-dimensional arrays. In the former, the pixels are arranged in a single row or column. In the latter, the pixels are arranged in a matrix of columns and rows. Although some publications reserve the term “focal plane array” to matrix arrays only, that is not true herein.

In general, a focal plane array consists of two parts, the infrared sensitive material and the read-out integrated circuit (ROIC), sometimes referred to as the “substrate.” The ROIC includes the means to electrically address the pixels sequentially. It may also include some form of signal processing, such as amplification, signal integration, and multiplexing. Because these on-chip functions are usually accomplished by analog signal processing, the ROIC may also include an analog-to-digital converter (ADC), in order that the off-chip signal processing electronics can be entirely digital.

Focal plane arrays are characterized as either "hybrid" or "monolithic." A hybrid array consists of two parts made separately, the infrared sensitive material and the ROIC, which are later mechanically and electrically joined; the most frequently used method is that of bump-bonding. Monolithic arrays are made using a silicon integrated circuit process during which the detecting material is deposited as a thin film on the silicon substrate containing the ROIC. The trend is strongly toward monolithic construction for reasons of performance, strength, and cost.

## 1.2 Detection Mechanisms[1]

Methods for detecting electromagnetic radiation fall into three categories, photon detection, thermal detection, and wave interaction detection (see Table 1-1). Each is discussed below.

**Table 1-1.** Classes of infrared detectors.

| Photon | Wave Interaction | Thermal |
|---|---|---|
| Photoconductivity | Optical heterodyne | Bolometer |
| Intrinsic | Photon-assisted tunneling | Metal |
| Extrinsic | Optical parametric | Semiconductor |
| Photovoltaic | Schottky barrier mixer | Superconductor |
| Photoelectromagnetic | Metal-oxide-metal | Ferroelectric |
| Phototransistor | | Hot electron |
| Photon drag | | Thermocouple/thermopile |
| Quantum counter | | Pyroelectric |
| Photoemissive | | Golay cell/gas microphone |
| | | Absorption edge |
| | | Pyromagnetic |
| | | Liquid crystal |
| | | Thermomechanical |

### 1.2.1 Photon detection mechanisms

Photon detection occurs when an incident photon, absorbed by a detecting material, interacts with electrons in the material. These electrons can either be bound to atoms in the material, or free. In most cases, the material is a semiconductor, characterized by a forbidden energy gap. The interaction may give rise to a free hole-electron pair, known as "intrinsic excitation," or to a free electron-bound hole or a free hole-bound electron, known as "extrinsic excitation." The free carrier may stay within the material (internal photoeffect) or may be emitted from the surface of the material (external photoeffect, photoemission).

The interaction of a photon with a bound electron requires that the photon energy exceed a given amount. Depending on the interaction the amount is either that of the forbidden energy gap or the ionization energy of the electron donors or acceptors. The energy of the photon is inversely related to the photon wavelength $\lambda$ through

$$E = hc/\lambda\,; \tag{1.1}$$

where $h$ is Planck's constant, $6.62 \times 10^{-34}$ Joule sec, and $c$ is the speed of light, $3\times10^{10}$ cm/sec. The energy can be expressed in electron volts and the wavelength in microns, resulting in

$$E(\text{eV}) = 1.24/\lambda\,(\mu\text{m})\,. \tag{1.2}$$

Therefore, if the infrared array is to respond to, say, 3–5-µm radiation, the forbidden energy gap or the donor or acceptor excitation energy must not exceed 0.25 eV; response to 8–14-µm radiation requires the energy gap or excitation energy not to exceed 0.09 eV.

In addition to the photoexcited carriers, the semiconductor material contains a background of thermally excited carriers. The concentration of thermally excited carriers depends on the semiconductor temperature, which is 295 K or 300 K for uncooled arrays, and on the forbidden energy gap or donor or acceptor ionization energies, which is either 0.25 eV for 3–5-µm wavelength detection or 0.09 eV for 8–14-µm wavelength detection. This combination of room temperature and long wavelength requirements causes a large background of thermally excited carriers against which the photoexcited carriers must be detected. The problem lies not with the total number of thermally excited carriers but with the fluctuations in that number caused by fluctuations in their generation and recombination rates, termed "g-r noise."

The problem of employing uncooled photon detector arrays for thermal imaging of room temperature scenes is the following:

- The photon detector requires a long wavelength response, extending at least to 5 µm, preferably to 14 µm, to detect radiation from room temperature scenes. This means that the forbidden energy gap or donor or acceptor ionization energy must be no greater than 0.25 eV, preferably no greater than 0.09 eV.
- A small forbidden energy gap or small donor or acceptor ionization energy gives rise to a large g-r noise background against which the photo-excited carriers must be detected.
- Cooling the detector would reduce the g-r noise, but the detector would not meet the uncooled requirement.

It can be shown that g-r noise arising from carrier generation and recombination at donor or acceptor sites exceeds that from intrinsic excitation at the same temperature.[2] Therefore, the most practical approach to an uncooled photon detector is to operate in the 3–5-µm region with intrinsic photoexcitation in a "small-gap" semiconductor such as indium antimonide (InSb), lead selenide (PbSe) or mercury cadmium telluride for which $x$=0.3 ($Hg_{0.7}Cd_{0.3}Te$). It has been shown[3] that InSb operating in the photoconductive or photoelectromagnetic (PEM) mode at room temperature can detect radiation of wavelength less than about 7 µm. It has also been shown that PbSe operating at room temperature can detect radiation of wavelength less than 5 µm. In practice, however, PbSe arrays are mounted on thermoelectric coolers to reduce their temperature about 40 K below room temperature.

It is theoretically possible to operate photon detectors such as InSb in a non-equilibrium mode[4,5] which reduces the cooling requirement, but this has not been shown to be practical.

In summary, uncooled photon detectors find almost no use in thermal imaging of room temperature scenes. They will not be considered further.

## 1.2.2 Thermal detection mechanisms

Thermal detection mechanisms are defined as mechanisms that change some measurable property of a material due to the temperature rise of that material caused by the absorption of electromagnetic radiation. Table 1-1 lists many thermal mechanisms. Of these, the most important are the resistive bolometric effect, the pyroelectric effect and its modification known as either the bias-enhanced pyroelectric effect or the ferroelectric bolometer, and the thermoelectric effect. Although there are many more thermal detection mechanisms and the list continues to grow with time, only those above have been shown to date to be practical. They are the subject of subsequent chapters and are discussed briefly below.

### 1.2.2.1 Resistive bolometer

A resistive bolometer changes its electrical resistance as its temperature rises due to the absorption of electromagnetic radiation. In practice, it is a thin metal or semiconductor film having an absorbing film deposited on it and is usually suspended over a cavity in a substrate to provide thermal isolation, i.e., to minimize heat flow from the film to its surroundings. The electrical resistance of the film is monitored. When incident infrared radiation is absorbed by the film, its temperature rises. If the film is metallic, the resistance increases; if it is semiconducting, the resistance decreases. When the incident radiation is removed, the temperature of the film decreases, causing the resistance to decrease (metallic) or increase (semiconducting).

### 1.2.2.2 Pyroelectric effect

The pyroelectric effect is exhibited by certain materials, usually ferroelectric, which exhibit spontaneous electric polarization that can be measured as a transient electrical charge on opposite faces of a crystal. Neutralization of the surface charge occurs automatically by internal charge flow. If the temperature of the material is changed rapidly, the surface charge will reappear, again to be neutralized. If temporally modulated infrared radiation is absorbed by the material, such as by means of a radiation chopper, an alternating current will flow in an external circuit connected to opposite faces of the material. The amplitude of the current, which flows in the absence of an externally applied voltage, depends on the intensity and rate of change of the absorbed radiation.

The ferroelectric properties of these materials disappear above a given temperature unique to each material, known as the Curie temperature. Because the rate of change with temperature of the ferroelectric polarization is greatest just below the Curie temperature, pyroelectric arrays sometimes employ a thermoelectric temperature stabilizer to maintain the average temperature of the array just below the Curie temperature. If the ferroelectric material is a mixed crystal, such as barium strontium titanate, $Ba_{1-x}Sr_xTiO_3$, the Curie temperature can be adjusted to be room temperature by varying the Ba to Sr ratio during compound synthesis. This approach has been followed in hybrid arrays. Monolithic arrays usually employ ferrroelectric materials whose Curie temperature is well above room temperature. In this case, no temperature stabilizer is required.

### 1.2.2.3 Field-enhanced pyroelectric effect/ferroelectric bolometer

Pyroelectric materials are operated in a capacitive mode. In some of these materials, the dielectric constant changes rapidly over a narrow temperature range on either side of the Curie temperature. This effect can be exploited as an addition to the pyroelectric effect, which increases the signal. Readout of this signal uses the same geometry as that of the pyroelectric effect, but an electrical bias is required. When the pyroelectric and dielectric effects are combined in a single device, it is termed a “field-enhanced pyroelectric detector,” or a “ferroelectric bolometer.” Hybrid ferroelectric arrays are usually operated in this manner.

### 1.2.2.4 Thermoelectric effect/radiation thermocouple

Consider an electrical circuit consisting of two wires of different metals that are mechanically and electrically joined at both ends. Let one wire be cut and a voltmeter inserted in the circuit at that point. If one junction is heated with respect to the other, a voltage will be measured whose magnitude is proportional to the temperature difference between the junctions. This structure is known as a thermocouple; the effect is termed the thermoelectric effect. The thermoelectric properties of the junctions are expressed in terms of the "Seebeck coefficients" of the materials employed; their values can be determined from tables listed in handbooks of material properties. In addition to metals, semiconductors exhibit thermoelectric properties. Their Seebeck coefficients, in general much larger than those of metals, depend on the semiconductor and the sign and concentration of impurity species within it.

Although the thermoelectric voltage from a single junction pair is small, it is possible to connect many junction pairs in series, thereby increasing the voltage in proportion to their number. Such a device is termed a "thermopile."

Radiation thermocouples and radiation thermopiles are used to detect thermal radiation. The thermal mass, i.e., heat capacity, of one or a series of junctions must be very small, and the junctions must be thermally isolated very well. As with resistive bolometers, the signal junctions are usually constructed within a thin film deposited on a bridge over a cavity in the substrate. The reference junctions are deposited directly on the substrate, which acts as a heat sink.

### 1.2.3 Wave interaction effects

The third class of methods for detecting electromagnetic radiation is that of wave interaction (see Table 1-1). In contrast to photon and thermal effects, which depend on the intensity of the incident electromagnetic radiation, wave interaction effects depend on the magnitude of the incident electric field vector. They are the principal methods of coherent detection of microwaves and radio waves. Although efforts have been made to apply the technology to the detection of infrared radiation, none has proven to be of any practical value. They will not be considered further.

## 1.3 Figures of Merit

Although there are many figures of merit that describe the performance of infrared focal plane arrays, those which are of most interest in analyzing the performance of uncooled thermal imaging arrays are the responsivity, noise equivalent power, D*, noise equivalent temperature difference (NETD), minimum resolvable temperature difference (MRTD), and thermal response time. As will be seen, the NETD involves not only the array but also the optics; the MRTD involves not only the array but also the optics, electronics, display, and the human observer. In the following chapters, these figures of merit will be applied, where appropriate, to the principal thermal detection mechanisms.

The definitions of these figures of merit are presented below. All except the MRTD can be applied to a single pixel, to the average of all the pixels in an array, or in histogram form to the distribution of values within an array. The blackbody temperature appropriate to a given measurement must always be specified.

## 1.3.1 Responsivity

The responsivity $\Re$, a function of the blackbody source temperature, is the output signal voltage from a pixel of an array divided by the incident radiant power falling on that pixel, given by

$$\Re = \frac{V_s}{P_o}; \tag{1.3}$$

where $V_s$ is the signal voltage and $P_o$ is the radiant power incident upon the pixel, expressed in watts. If the signal is a current, the responsivity is expressed in amps/watt.

## 1.3.2 Noise equivalent power and D*

The noise equivalent power (NEP), symbolized $P_N$, is the radiant power incident upon a pixel which gives rise to a signal equal to the root mean square (rms) pixel noise within the system bandwidth. It is given by

$$P_N = \frac{V_N}{\Re}; \tag{1.4}$$

where $V_N$ is the rms noise voltage within the system bandwidth. For "white" noise, i.e., noise whose amplitude is frequency independent, the noise voltage depends on the square root of the bandwidth. Also, for most detection mechanisms, including the thermal ones under consideration, the signal-to-noise ratio depends on the square root of the active area of a pixel. (The ratio of the active area of a pixel to the total area of a pixel is known as the "fill factor.") Assuming a fill factor of unity, the figure of merit D* ("dee-star") is defined to be

$$D^* = \frac{(A_D B)^{1/2}\Re}{V_N} = \frac{(A_D B)^{1/2}}{P_N}; \tag{1.5}$$

where $A_D$ is the area of the pixel. If the fill factor $\beta$ is less than unity, $(\beta A_D B)^{1/2}$ appears in the numerator of Eq. (1.5).

The units of D* are cm $\mathrm{Hz}^{1/2}$/watt. Because the response of photon detectors depends on wavelength, D* is expressed for them in two ways: a "spectral D*," symbol $D^*_\lambda$, and a "blackbody D*," symbol D*($T$), where $T$ is the blackbody temperature. For thermal detectors, whose response is nominally independent of wavelength, only D*($T$) is used; it is then represented simply as D*. In reality, thermal detectors do exhibit a wavelength dependence due to the spectral properties of an absorbing layer or of a resonant optical cavity, so it is necessary to specify the blackbody temperature when presenting D* values.

### 1.3.3 Noise equivalent temperature difference

The two equivalent definitions of the noise equivalent temperature difference (NETD) are as follows:

1. The NETD is the change in temperature of a blackbody of infinite lateral extent which, when viewed by a thermal imaging system, causes a change in signal-to-noise ratio of unity in the electrical output of the pixels of a focal plane array, or else of the readout electronics which receives an input signal from the pixels of the array. Whichever it is must be specified.
2. The NETD is the difference in temperature between two side-by-side blackbodies of large lateral extent which, when viewed by a thermal imaging system, gives rise to a difference in signal-to-noise ratio of unity in electrical outputs of the two halves of the array viewing the two blackbodies. These can be measured either at the output of the focal plane array or at the output of the readout electronics. Whichever it is must be specified.

In either definition, the NETD can be expressed as that of a single pixel, or it can be the average of the pixels of an array. The expression for the NETD is

$$NETD = \frac{4F^2 V_N}{\tau_o A_D \Re (\Delta P / \Delta T)_{\lambda_1 - \lambda_2}}, \tag{1.6}$$

where $\tau_o$ is the transmittance of the optics, $A_D$ is the total area of a pixel, and $F$ is given by

$$F = \frac{1}{2 \sin \theta}, \tag{1.7}$$

where $\theta$ is the angle which the marginal ray from the optics makes with the axis of the optics at the focal point of the image. Also, $(\Delta P/\Delta T)_{\lambda_1\text{-}\lambda_2}$ is the change in power per unit area radiated by a blackbody at temperature $T$, with respect to $T$, measured within the spectral band from $\lambda_1$ to $\lambda_2$. The values for $(\Delta P/\Delta T)_{\lambda_1\text{-}\lambda_2}$ for a 295 K blackbody within the 3–5-µm and 8–14-µm intervals, listed by Lloyd,[6] are as follows

$(\Delta P/\Delta T)_{3\text{-}5} = 2.10 \times 10^{-5}$ W/cm$^2$ deg K.
$(\Delta P/\Delta T)_{8\text{-}14} = 2.62 \times 10^{-4}$ W/cm$^2$ deg K.

Note that $F$ is a function of distance from the optics to the scene being viewed, i.e., the focal point of the image is a function of that distance. If the scene is at infinity, the image is at the focal length of the optics, and the following substitution can be made

$$4F^2 = 4(f/D)^2 + 1; \tag{1.8}$$

where $f$ is the focal length of the optics, $D$ is the diameter of the optics, and $(f/D)$ is the focal ratio of the optics.

## 1.3.4 Minimum resolvable temperature difference

The minimum resolvable temperature difference (MRTD) (sometimes referred to as the MRΔT) is a graphical representation of the log temperature versus log spatial frequency measurement of a thermal imaging system. Whereas the NETD is a measure of temperature sensitivity, the MRTD interrelates temperature sensitivity with the spatial details of a target imaged upon an array. The spatial details are expressed in terms of a system modulation transfer function (MTF), comprised of the individual MTFs of the optics, the detector array, the electronics, the display, and the human eye. The spatial frequency is expressed in line pairs per millimeter, where the line pairs alternate hot and cold bars of a standard resolution target that are imaged upon a detector array; the size of a line pair imaged on the array is expressed in millimeters. It can also be expressed in line pairs per milliradian, referring to the angular subtense of one line pair at the focal point.

This subject is extremely complex. The development of an appropriate model of a two-dimensional focal plane array has taken about two decades of research. Accurate measurement of the MRTD of a given infrared imaging system with display requires a standardized human observer with calibrated eyes, such as can be found at the U.S. Army CECOM Night Vision and Electronic Sensors Directorate.

See Holst[7] for a detailed description of MRTD measurement methods.

## 1.3.5 Thermal response time

The thermal response time $\tau_T$ is the time required for the temperature of a pixel to decrease to $1/e$ of its value when thermal radiation from a steady state source falling on the pixel is instantaneously removed. Here, $e$ is the base of the natural logarithms.

It will later be shown that the thermal response time $\tau_T$ for all thermal detection mechanisms is

$$\tau_T = \frac{C}{G}; \tag{1.9}$$

where $C$ is the heat capacity of the pixel and $G$ is the sum of the thermal conductances of all the heat loss mechanisms which remove heat from the pixel. The units of $C$ are joules/deg K; those of $G$ are watts/deg K. Thus the units of $\tau_T$ are seconds.

## References

1. P.W. Kruse, "The photon detection process," Chapter 2 of *Optical and Infrared Detectors*, *Topics in Applied Physics 19*, R.J. Keyes, ed., Springer-Verlag, New York (1977).
2. D. Long, "On generation-recombination noise in infrared detector materials," *Infrared Phys*. **7**, p. 169 (1967).
3. P.W. Kruse, "Indium antimonide photoconductive and photoelectromagnetic detectors," Chapter 2 of *Infrared Detectors, Semiconductors and Semimetals 5*, R.K. Willardson and A.C. Beer, eds., Academic Press, New York (1970).
4. T. Ashley, C.T. Elliott, and A.T. Harker, "Non-equilibrium modes of operation for infrared detectors," *Infrared Phys*. **26**, p. 303 (1986).
5. C.T. Elliott, "Non-equilibrium modes of operation of narrow-gap semiconductor devices," *Semicond. Sci. Technol*. **5**, p. 530 (1990).
6. J.M. Lloyd, *Thermal Imaging Systems*, Plenum, New York (1975).
7. G.C. Holst, *Testing and Evaluation of Infrared Imaging Systems*, JCD Publishing Co., Maitland, FL (1993).

# Chapter 2

# Fundamental Limits

## 2.1 Introduction

All infrared detectors are subject to performance limits arising from the statistical nature of the infrared radiation being absorbed. Photon detectors are subject to a limit associated with the statistical rate of arrival of photons from the radiating background to which the detectors are exposed; this is known as the BLIP (background limited infrared photodetector) limit. Thermal detectors are subject to a similar limit; the analysis is in terms of the statistical fluctuations in the incident radiant energy associated with the statistical fluctuations in the rate of arrival of photons from the radiating background.

Thermal detectors are also subject to temperature fluctuation noise, arising from temporal fluctuations in absorbed energy due to conduction or convection of heat from sources other than the radiating background. The detector consists of a sensitive area coupled to a substrate. Construction can be hybrid or monolithic. In either case, heat is exchanged by conduction between the sensitive area and the substrate. This gives rise to random fluctuations in the temperature of the sensitive area; this is known as temperature fluctuation noise. Even if the pixel and the substrate are at exactly the same temperature, temperature fluctuation noise will be present; it does not require heat flow from a warm pixel to a cool substrate. If the detector is not in an evacuated package, temperature fluctuation noise will also result from conduction and convection through the air surrounding the sensitive area. Thus background fluctuation noise can be seen as the ultimate manifestation of temperature fluctuation noise when thermal conduction and convection are negligible compared with radiation exchange between the detector and its surroundings.

In the design of uncooled infrared detectors and arrays, minimizing temperature fluctuation noise is of utmost importance. This is the reason why construction has shifted away from hybrid, with a relatively high thermal conductance through the bump bond, to monolithic, with far less conductance that can also be controlled through proper design of the “legs” supporting the sensitive area.

The analysis of the temperature fluctuation noise and background fluctuation noise limits in thermal detectors was presented by the author and colleagues in a book[1] long out of print. The analysis is reprinted below. It will be seen that different approaches in Secs. 2.2 and 2.3 give the same result.

## 2.2 Photon Noise Limitations of Thermal Detectors[1]

Because thermal detectors are sensitive to the absorbed radiant power intensity, whereas photon detectors respond to the rate of photon absorption, the analysis of the photon noise limitations of the two types differ. The photon noise limitation of thermal detectors is imposed by fluctuations in the absorbed power, because of the quasi-random arrival of the photons, whereas photon detectors are limited by fluctuations in the rate of photon absorption. Consider first the photon noise-limited thermal detector.

Assume a thermal detector that is coupled to its environment by radiation interchange alone, that is, there is no energy interchange through the mechanisms of convection or conduction. Assume that the detector is at a temperature $T_1$, surrounded by a uniform environment at a temperature $T_2$, and that it has an emissivity $\eta$ that is independent of $T_1$ and of wavelength. The noise spectrum of the power emitted by a radiating body in the optical frequency interval $d\upsilon\,\nu$ is

$$dP_p = 2Ah\upsilon M(\upsilon,T)\frac{\exp(h\upsilon/kT)d\upsilon}{[\exp(h\upsilon/kT)-1]}. \tag{2.1}$$

$M(\upsilon,T)$ is the power per unit area per unit optical frequency interval emitted by a radiating body.

$$M(\upsilon,T) \equiv \frac{2\pi h\upsilon^3/c_o^{\,2}}{[\exp(h\upsilon/kT)-1]}. \tag{2.2}$$

Also, $\upsilon$ is the optical frequency, $h$ is Planck's constant, $c_o$ is the speed of light, $T$ is the absolute temperature, $k$ is Boltzmann's constant, and $A$ is the emitting area, which is the pixel area $A_D$ multiplied by the fill factor $\beta$, i.e., the fraction of $A_D$ which has an emissivity $\eta$.

The noise power spectrum $P_p(f)$ represents the mean square deviation from the mean of the radiant power and is given by

$$P_p(f) \equiv \int_0^\infty dP_p = \int_0^\infty 2A_D\beta h\upsilon M(\upsilon,T)\frac{\exp(h\upsilon/kT)}{[\exp(h\upsilon/kT)-1]}d\upsilon. \tag{2.3}$$

Thus $P_p(f)$ is termed the mean square noise power per unit bandwidth of the emitted radiation. The integral is found to be

$$P_p(f) = 8A_D\beta\sigma kT_2^5\ ; \tag{2.4}$$

where the subscript 2 has been added to $T$ to refer to the emitting background. Note that the noise power spectrum is frequency independent or "white." The mean square noise power $\overline{P_p^2}$ in a bandwidth $B$ is therefore

$$\overline{P_p^2} = 8A_D\beta\sigma kT_2^5B\,. \tag{2.5}$$

Consider now the interaction of this radiation noise with the photon noise-limited thermal detector. $A_D\beta$ in this instance represents the receiving area of the pixel. Assume the detector is sensitive to all possible wavelengths and therefore can detect all the incident noise. Since it has an emissivity $\eta$, which is identical with the absorptivity, the received mean square noise power will be

$$\overline{P_p^2} = 8A_D\beta\eta\sigma kT_2^5B\,. \tag{2.6}$$

However, there will also be a contribution to the noise due to random fluctuations in the radiation power emitted by the pixel. The pixel is itself a radiating body, having an emissivity $\eta$ and a temperature $T_1$. The quasi-random emission of photons from it, which carry away heat, is known as photon noise. By the same argument as above, the mean square noise power of the emitted radiation in a bandwidth $B$ will be

$$\overline{P_p^2} = 8A_D\beta\eta\sigma kT_1^5B\,. \tag{2.7}$$

Thus the total mean square radiation noise power in the bandwidth $B$ is

$$\overline{P_p^2} = 8A_D\beta\eta\sigma k(T_1^5 + T_2^5)B\,. \tag{2.8}$$

In the particular instance in which the detector and the surroundings are in equilibrium and therefore are at the same temperature, the mean square noise power will be

$$\overline{P_p^2} = 16A_D\beta\eta\sigma kT^5B\,. \tag{2.9}$$

The rms noise power for values of $A$=1 mm$^2$, $\beta$=1, $\eta$=1, $T$=300 K, and $B$ = 1 Hz is

$$\left(\overline{P_p^2}\right)^{1/2} = 5.55\times10^{-12}\,\mathrm{W}. \tag{2.10}$$

The photon noise-limited detectivity of a photon noise-limited thermal detector will now be determined. The noise equivalent power, the incident radiant power required to give a signal voltage equal to the noise voltage in a specified bandwidth, will be numerically equal to $\left(\overline{P_p^{\,2}}\right)^{1/2} \big/ \eta$, since the thermal mechanism will transduce the photon noise equally as well as the radiation signal. Therefore D*, the square root of the detector area per unit noise equivalent power in a 1 Hz bandwidth, will be

$$\mathrm{D}^* = \frac{\eta}{[8\eta\sigma k(T_1^5 + T_2^{\,5})]^{1/2}} = \frac{\mathrm{cm(Hz)}^{1/2}}{\mathrm{W}}\,. \tag{2.11}$$

Note that D* is independent of $A_D\beta$, as is to be expected.

In many practical instances the temperature of the background, $T_2$, will be room temperature, 290 K. For many detectors, such as thermopiles and bolometers, the detector temperature will also be 290 K. Figure 2-1 shows the photon noise-limited detectivity for an ideal thermal detector having an emissivity of unity, operated at 290 K and lower, as a function of detector temperature $T_1$ and background temperature $T_2$. Note that Eq. (2.11) is symmetrical in $T_1$ and $T_2$. Thus $T_1$ and $T_2$ can be interchanged in Fig. 2-1.

It can be seen that the highest possible D* to be expected from a thermal detector operated at room temperature and viewing a background at room temperature is $1.98 \times 10^{10}$ cm Hz$^{1/2}$/W. Even if the detector or background, not both, were cooled to absolute zero, the detectivity would improve only by the square root of two. This is a basic limitation of all thermal detectors.

Note that Eq. (2.11) and Fig. 2-1 assume that background radiation falls upon the pixel from all directions when the detector and background temperatures are equal, and from the forward hemisphere only when the detector is at cryogenic temperatures. In the latter case, if the field of view is reduced by cold shielding, and the pixel remains background limited, the D* value will depend inversely upon the sine of the half angle of θ where θ is the included angle of the cold shield (see Fig. 2-2).

## 2.3 Temperature Fluctuation Noise in Thermal Detectors[1]

Another approach to determining the photon noise limited performance of thermal detectors is through the concept of temperature fluctuation noise. A thermal detector in contact with its environment by conduction and radiation exhibits random fluctuations in temperature, known as temperature fluctuation noise, because of the statistical nature of the heat interchange with its surroundings. If the conduction interchange is negligible compared to the

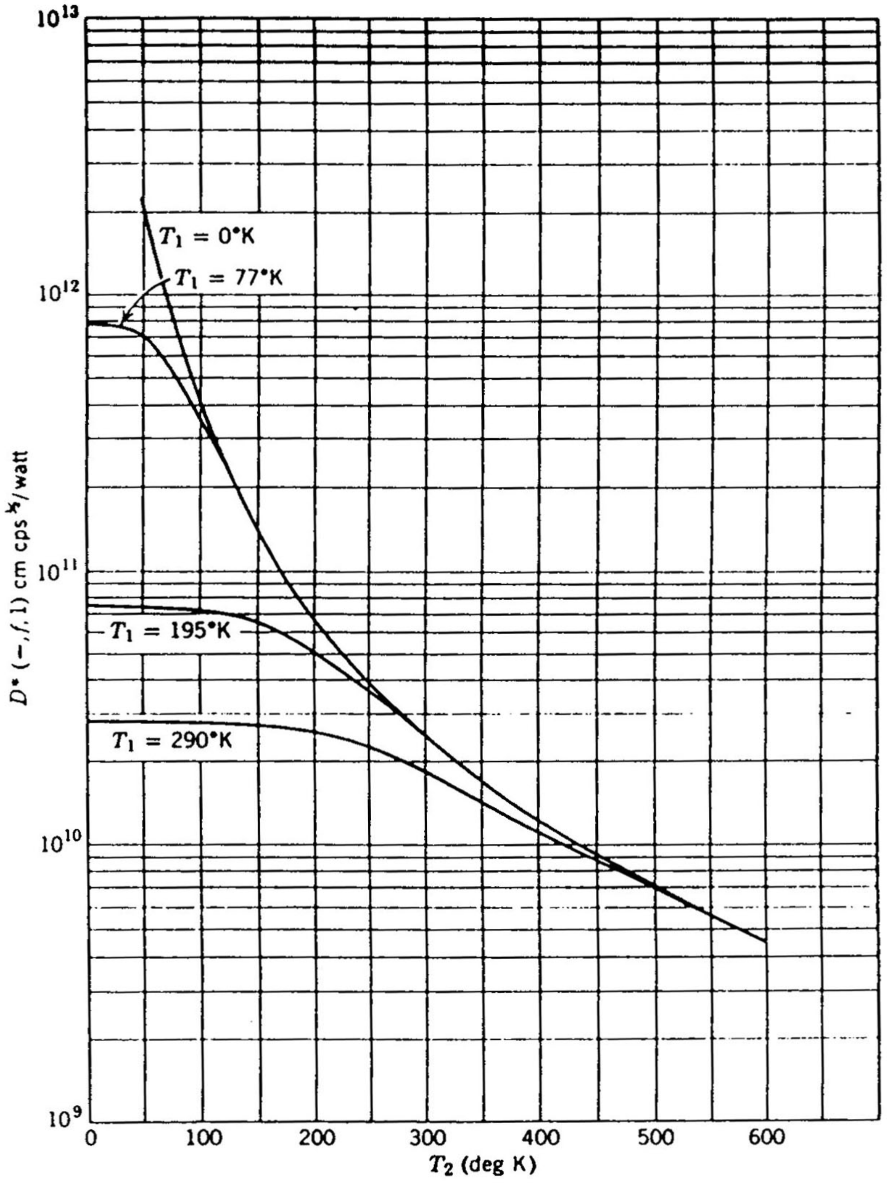

**Figure 2-1.** Photon noise-limited D* of thermal detectors as a function of detector temperature $T_1$ and background temperature $T_2$. Viewing angle of $2\pi$ steradians and unit absorptivity. From P.W. Kruse, L.D. McGlauchlin, and R.B. McQuistan.[1]

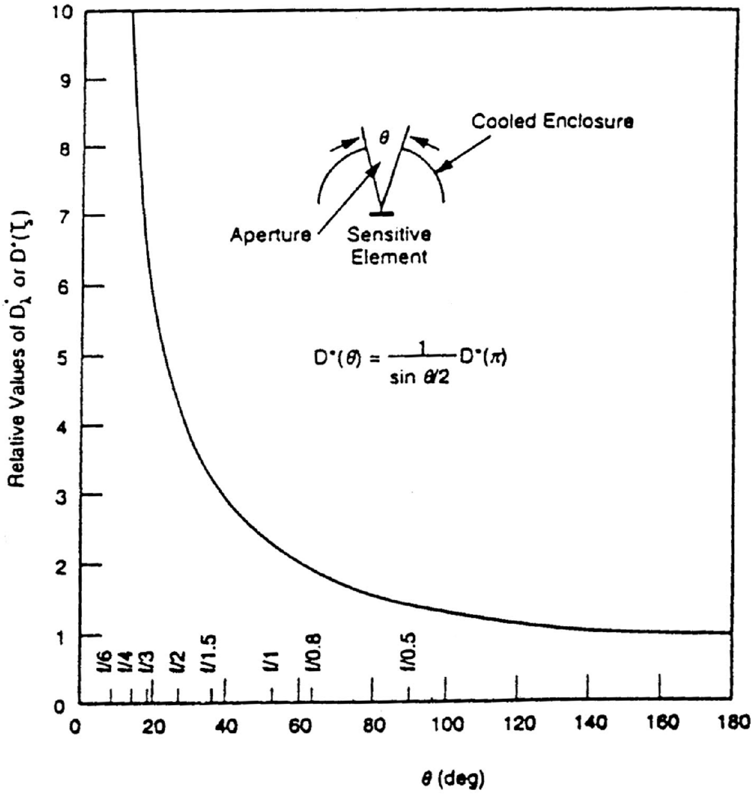

**Figure 2-2.** Relative increase in background fluctuation noise-limited $D^*_\lambda$ and $D^*(T)$ for photon and thermal detectors achieved by using cold aperture. From P.W. Kruse, L.D. McGlauchlin, and R.B. McQuistan.[1]

radiation interchange, temperature fluctuation noise would be expected to become identified with background fluctuation noise. The following discussion demonstrates this mathematically. Consider first of all the magnitude of the temperature fluctuations of the detecting material. The material, having a heat capacity $C$, changes its temperature $T$ by the incremental amount $\Delta T$ in response to the energy increment $\Delta E$ according to

$$\Delta E = C\,\Delta T. \tag{2.12}$$

The thermodynamic system composed of the material and surroundings possesses many degrees of freedom. Tolman[2] states that the mean square fluctuations in energy $\overline{\Delta E^2}$ of a system having many degrees of freedom is given by

$$\overline{\Delta E^2} = kT^2 C\,; \tag{2.13}$$

where $k$ is Boltzmann's constant. Therefore

$$\overline{\Delta T^2} = \frac{kT^2}{C}. \tag{2.14}$$

Einstein[3] showed that $C$ in this case is the harmonic mean of the heat capacities of the material and surroundings.

$$C = \frac{C_A C_B}{C_A + C_B}\,; \tag{2.15}$$

where $C_A$ and $C_B$ are the heat capacities of the body and surroundings, respectively. If the surroundings have a much greater heat capacity than the body, which is the usual situation, the harmonic mean heat capacity becomes that of the body.

Next consider the spectral content of the fluctuations. Let the detecting material be at an incremental temperature difference $\Delta T$ above its surroundings. Heat will flow from the material to the surroundings at a rate proportional to $\Delta T$, the proportionality constant being the heat transfer coefficient $G$ between the material and the surroundings. The heat transfer equation is

$$\frac{d(\Delta E)}{dt} = G\Delta T\,; \tag{2.16}$$

where $d(\Delta E)/dt$ is the rate of flow of heat. However, Eq. (2.12) shows that the rate of flow of heat can also be expressed as

$$\frac{d(\Delta E)}{dt} = C\frac{d(\Delta T)}{dt}\,. \tag{2.17}$$

If the material is at a higher temperature than its surroundings, heat flows from the material to the surroundings and $d(\Delta E)/dt$ is negative. Equating Eqs. (2.16) and (2.17), a differential equation describing the heat transfer is found to be

$$-C\frac{d(\Delta T)}{dt} = G\Delta T. \tag{2.18}$$

The solution of this is

$$\Delta T = \Delta T_0 \exp(-t/\tau_T)\,; \tag{2.19}$$

where $\Delta T_0$ is the value of $\Delta T$ at $t$=0 and $\tau_T \equiv C/G$. If heat is allowed to flow into the body from an external source—for example, a radiating background—the differential equation becomes

$$C\frac{d(\Delta T)}{dt} + G\Delta T = P(t)\,; \tag{2.20}$$

where $P(t)$ is the fluctuation in the power from the external source. In order to solve this equation, let

$$P(t) = P_f \exp(j2\pi f t)\,; \tag{2.21}$$

where $j \equiv \sqrt{-1}$. Assume that the mean square value of $P_f$, denoted $\overline{P_f^{\,2}}$, is independent of $f$ and can be written as

$$\overline{P_f^{\,2}} = P_0 B\,; \tag{2.22}$$

where $P_0$ is a constant. The modulus of the solution of Eq. (2.20) is

$$\overline{\Delta T_f^{\,2}} = \frac{\overline{P_f^{\,2}}}{G^2 + 4\pi^2 f^2 C^2} = \frac{P_0 B}{G^2 + 4\pi^2 f^2 C^2}. \tag{2.23}$$

The value $\overline{\Delta T_f^{\,2}}$ represents the frequency dependence of the mean square temperature fluctuations. To determine the value of $\overline{\Delta T^2}$, the mean square value of the fluctuations over all frequencies $f$, Eq. (2.23) is integrated over all frequencies, assuming $G$ and $C$ are frequency independent.

$$\overline{\Delta T^2} = P_0 \int_0^\infty \frac{df}{G^2 + 4\pi^2 f^2 C^2} = \frac{P_0}{4GC}. \tag{2.24}$$

In order to determine the value of $P_0$, the expressions for $\overline{\Delta T^2}$ found in Eqs. (2.14) and (2.24) are equated. Substituting the value obtained into Eq. (2.23), the expression for the spectrum of the mean square fluctuations in $\Delta T$ is found to be

$$\overline{\Delta T_f^{\,2}} = \frac{4GkT^2 B}{G^2 + 4\pi^2 f^2 C^2}\;. \tag{2.25}$$

The mean square value of the power fluctuations in the incident radiation can now be determined. The mean square power fluctuations, which are simply the quantity $\overline{P(t)^2}$, are found from Eqs. (2.23) and (2.25) to be

$$\overline{P_p^{\,2}} = 4kT^2GB. \tag{2.26}$$

Thus, the heat capacity $C$ does not enter into the expression for the power fluctuations. This is of fundamental importance, since it indicates that the temperature fluctuation noise-limited performance of a thermal detector is independent of detector material and volume.

The temperature fluctuation noise-limited D*, i.e., $\mathrm{D}^*_{TF}$, is determined by combining Eqs. (1.5) and (2.26). It is recognized that $\overline{P_p^{\,2}}$ of Eq. (2.26) is the square of the noise equivalent power $P_N$ of Eq. (1.5). Because the responsivity $\Re$ of Eq. (1.5) contains the absorptance η, it is included directly in $\mathrm{D}^*_{TF}$. Also Eq. (1.5) assumes a fill factor β of unity. It too is included in $\mathrm{D}^*_{\mathrm{TF}}$. Thus

$$\mathrm{D}^*_{TF} = \left(\frac{\eta^2\beta A_D}{4kT^2G}\right)^{1/2}. \tag{2.27}$$

In order to determine the value for the heat transfer coefficient $G$ for background fluctuation noise, recall that $G$ is defined as the proportionality constant between the rate of flow of energy and the temperature increment, see Eq. (2.16). For a gray body this becomes

$$G = 4\eta\sigma T^3 A_D\beta. \tag{2.28}$$

Substituting this into Eq. (2.26), the fluctuations in the power flow between the detecting material and source are given by

$$\overline{P_p^{\,2}} = 16A_D\beta\eta\sigma kT^5B. \tag{2.29}$$

Note that this is the same expression that was deduced for the photon noise in thermal detectors given by Eq. (2.9). Therefore, temperature noise in thermal detectors in thermal equilibrium with their surroundings, in which radiation exchange with their surroundings predominates, is identified with photon noise.

The background fluctuation noise-limited D*, i.e., $\mathrm{D}^*_{BF}$, is determined by combining Eqs. (1.5) and (2.29). It is recognized that $P_p^{\,2}$ of Eq. (2.29) is the square of the noise equivalent power $P_N$ of Eq. (1.5). Because the responsivity $\Re$ of Eq. (1.5) contains the absorptance η, it is included directly in $D^*_{BF}$. Thus

$$D^*_{BF} = \left[\frac{\eta}{8k\sigma(T_1^5 + T_2^5)}\right]^{1/2}. \tag{2.30}$$

## 2.4 Temperature Fluctuation Noise Limit to Focal Plane Array Performance[4]

The temperature fluctuation noise limit to the performance of a focal plane array is determined by assuming that all other pixel and system noise sources are negligible in comparison with temperature fluctuation noise in the pixel. Then, by substituting Eqs. (1.5) and (2.27) into Eq. (1.6), with $T_1$=$T_2$, the temperature fluctuation noise-limited NETD, i.e., NETD$_t$, is given by

$$\mathrm{NETD}_t = \frac{8F^2T_1(kGB)^{1/2}}{\tau_0\beta A_D\eta(\Delta P/\Delta T)_{\lambda_1-\lambda_2}} \tag{2.31}$$

## 2.5 Background Fluctuation Noise Limit to Focal Plane Array Performance[4]

The background fluctuation noise limit to the NETD, i.e, NETD$_b$, is found when radiation exchange is the dominant thermal exchange mechanism. In this case, the NETD is determined by substituting Eqs. (1.5) and (2.11) into Eq. (1.6).

$$\mathrm{NETD}_b = \frac{8F^2[2k\sigma B(T_1^5 + T_2^5)]^{1/2}}{\tau_0(\beta\eta A_D)^{1/2}(\Delta P/\Delta T)_{\lambda_1-\lambda_2}}. \tag{2.32}$$

The temperature fluctuation noise and background fluctuation noise-limited NETD of a focal plane array operating at 300 K against a 300 K background, determined from Eqs. (2.31) and (2.32), are illustrated in Fig. 2-3. Other parameters are listed on the figure. For comparison, the same limits for a thermal detector operating at 85 K, such as a high transition temperature superconducting bolometer,[5] are also shown.

Eqs. (2.11) and (2.30) and Fig. 2-3 assume that the spectral response of the thermal detector, determined by η, is wavelength independent. If η=0 for all wavelengths except between $\lambda_1$=$c/\upsilon_1$ and $\lambda_2$=$c/\upsilon_2$, and if η is independent of wavelength between $\lambda_1$ and $\lambda_2$, then Eq. (2.30) is replaced by[6]

$$\mathrm{D}_b^* = \left[ \frac{\eta}{8k\sigma T_1^5 + F(\upsilon_1, \upsilon_2)} \right]^{1/2}; \tag{2.33}$$

where

$$F(\upsilon_1, \upsilon_2) = 2\left[ \int_{\upsilon_1}^{\upsilon_2} h\upsilon M(\upsilon, T_2) \right] \left[ \frac{\exp(h\upsilon / kT_2) d\upsilon}{\exp(h\upsilon / kT_2)^{-1}} \right]. \tag{2.34}$$

Figure 2-4 illustrates Eq. (2.33) as a function of $\lambda$ for the case of a long wavelength cutoff $\lambda_0$, i.e., $\eta=1$ for $\lambda<\lambda_0$ and $\eta=0$ for $\lambda>\lambda_0$ and for the case of a short wavelength cutoff $\lambda_0$, i.e., $\eta=0$ for $\lambda<\lambda_0$ and $\eta=1$ for $\lambda>\lambda_0$. The background temperature is 300 K.

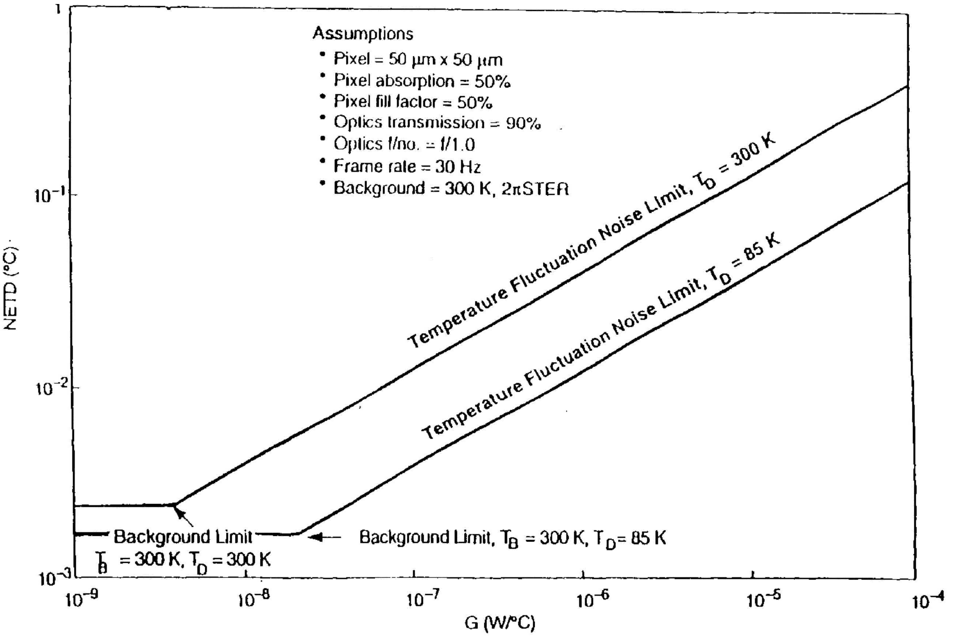

**Figure 2-3.** Temperature fluctuation noise limit and background fluctuation noise limit to NETD of uncooled and cryogenic thermal detector focal plane arrays as a function of thermal conductance *G*.

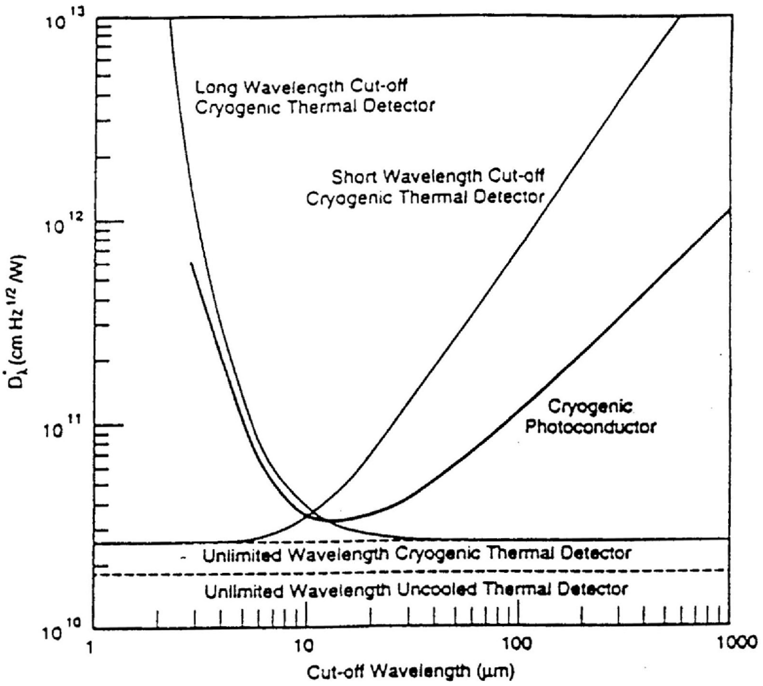

**Figure 2-4.** Dependence of $D^*_\lambda$ and $D^*(T_2)$ on long wavelength limit for thermal and photon detectors. From F.J. Low and A.R. Hoffman.[6]

## 2.6 Discussion

Equations (2.31) and (2.32) and their evaluation for selected values of their parameters in Fig. 2-3 are fundamental to an understanding of thermal detectors. It matters not whether they are bolometric, thermoelectric, pyroelectric or any other conceivable approach; they will be subject to temperature fluctuation noise and background fluctuation noise, which are fundamental limits. The sloping lines in Fig. 2-3 represent the temperature fluctuation noise limits for the values of the parameters listed. The horizontal lines represent the background fluctuation noise limits for the values of the parameters listed.

It can be seen from the figure that it is of paramount importance to have the smallest possible value of pixel thermal conductance $G$, subject to the condition that the pixel heat capacity is sufficiently small that the system thermal response time (i.e., the ratio of the pixel heat capacity to the pixel thermal conductance) requirement is met. Proper design of a thermal detector begins with the design of the thermal isolation structure. The temperature readout mechanism is designed subsequently. Primary emphasis on the temperature readout mechanism and secondary emphasis on the thermal isolation structure does not provide optimum performance.

## References

1. P.W. Kruse, L. D. McGlauchlin, and R. B. McQuistan, *Elements of Infrared Technology*, Chapter 9, John Wiley and Sons, Inc., New York (1962).
2. R. C. Tolman, *The Principles of Statistical Mechanics*, p. 632, Oxford University Press, London (1938).
3. A. Einstein, *Ann. Physik* **14**, p. 354 (1904).
4. P. W. Kruse, "A comparison of the limits to the performance of thermal and photon detector imaging arrays," *Infrared Phys. Technol.* **36**, p. 869 (1995).
5. B.R. Johnson and P.W. Kruse, "Silicon microstructure superconducting microbolometer infrared arrays," Proc. SPIE Vol. 2020, *Infrared Technology XIX* (1993).
6. F. J. Low and A. R. Hoffman, *Appl. Opt.* **2**, p. 649 (1963).

# Chapter 3

# Thermoelectric Arrays

## 3.1 Introduction

Although there are three thermoelectric effects observed in metals and semiconductors, only one, the "Seebeck effect," is employed in uncooled infrared arrays. Thus, the term "thermoelectric array" or "thermoelectric effect" herein refers only to the Seebeck effect.

The three thermoelectric effects are manifested in an electrical circuit that includes two dissimilar metals or semiconductors or a metal and semiconductor. These dissimilar metals must be electrically and mechanically joined, such as by soldering, at one or more points. An example is the joining of two wires of materials A and B at two points (see Fig. 3-1). Let wire A be cut and a high impedance voltmeter inserted at that point. If the two junctions are at the same temperature, no voltage will be measured. However, if one junction is warmer than the other, a voltage (referred to as the "Seebeck" voltage after its discoverer) will be detected. For small temperature differences such as are found in infrared arrays, the voltage depends linearly on the temperature difference between the two junctions.

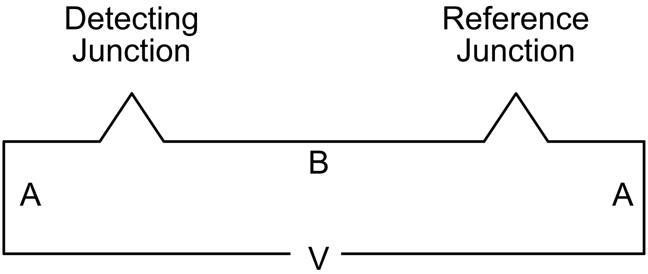

**Figure 3-1.** Radiation thermocouple.

The Seebeck effect in semiconductors is more complex than that in metals and in general far exceeds the value in metals. Consider a semiconductor wire to which a metal wire is connected at either end. Assume that the semiconductor is, say, p-type, and is operating in the extrinsic regime. Then, the free hole concentration at any point along the semiconductor wire is determined by the temperature at that point. That concentration is expressed in terms of the Fermi level, which therefore varies along the length of the wire. In effect, the temperature difference between the hot and cold junctions of the semiconductor tilts the energy bands and changes the Fermi potential with respect to the band edges along the semiconductor. Another way of explaining this is to say that the concentration of free holes (for a p-type semiconductor) at the hot end exceeds that at the cold. Therefore, free holes diffuse from the hot end toward the cold, causing the cold end to become positively charged with respect to the hot end. The internal electric field so established causes a drift of holes to flow from the cold to the hot end which balances the diffusion of holes from the hot to the cold. The spatially varying hole density is described in terms of the spatially varying Fermi potential.

A pair of dissimilar conductors joined in a region of unknown temperature and running to a reference temperature is termed a “thermocouple.” When the two temperatures differ, a voltage can be measured at the open end of the thermocouple. If the temperature difference is caused by the absorption of electromagnetic radiation, including infrared radiation, the device is known as a “radiation thermocouple.” The thermoelectric voltage can be increased by joining two or more junction pairs in series; this is known as a “thermopile.” When the absorption of electromagnetic radiation, including infrared radiation, is responsible for the temperature difference, it is known as a “radiation thermopile.”

If a battery or other dc voltage source replaces the voltmeter, then two other thermoelectric effects will be detected. Electrical current flowing through the circuit will cause one junction to heat and the other to cool. This is known as the “Peltier effect.” It is employed in thermoelectric coolers and temperature stabilizers. Whether a given junction heats or cools depends on the direction of the current through that junction. The “Thomson effect” occurs when an electrical current flows through a conductor, causing one end to become warmer than the other, depending on the direction of current flow.

It can be shown that only the Seebeck effect can be employed to detect infrared radiation. In comparison with the other principal uncooled detection mechanisms, i.e., the resistive bolometer and the pyroelectric detector/ferroelectric bolometer, its responsivity is low. On the other hand, like the pyroelectric detector, it does not require electrical bias, which means that no $1/f$ power law noise is observed. Furthermore, there is no “thermal pedestal” arising from Joulean heating which must be subtracted from the total heating to detect only the signal due to absorbed infrared radiation. Unlike the pyroelectric detector, the thermoelectric (Seebeck) detector has a dc response; thus it does not require a radiation chopper to detect stationary objects. Furthermore, the inherent linearity of the thermoelectric voltage with incident radiant power means that the thermoelectric detector has a large linear dynamic range. This is one reason why it is an attractive technology for imaging radiometers, which measure the temperature distribution within an image of a scene.

## 3.2 The Heat Flow Equation

Figure 3-2 is a cross-sectional view of one pixel of a thermoelectric thermal imaging array of monolithic construction. Two metals, A and B, are deposited on a silicon nitride ($Si_3N_4$) membrane spanning a cavity, made by anisotropic etching, in a silicon substrate. Infrared radiation falls upon the pixel, where it is absorbed by means of an absorbing layer (not shown). The membrane, of very small "thermal mass" (heat capacity), warms slightly. The silicon substrate, of very large thermal mass, does not. Thus a Seebeck voltage will be generated along the wire pairs. The voltage output of this wire pair is therefore a measure of the intensity of the absorbed radiation. Although the figure shows only one wire pair, usually there will be several, connected in series, thereby increasing the total signal voltage.

Figure 3-3 is a view of a monolithic pixel from above. It can be seen that the sensitive area of the pixel is connected to the substrate by "legs," a means to provide thermal isolation of the sensitive area. These legs are usually of silicon nitride; on them are deposited metals A and B connecting the thermocouples on the sensitive area with those on the substrate. Thermal conduction down the legs to the substrate is the principal mechanism by which heat is lost from the membrane. (The array is within a vacuum package to avoid heat loss by conduction through air.)

The pixel area is defined in terms of the center-to-center distance ("pitch") between adjacent pixels. Only the radiation falling on the membrane, i.e., the sensitive area, contributes to the signal. The ratio of the sensitive area to the total pixel area is termed the "fill factor."

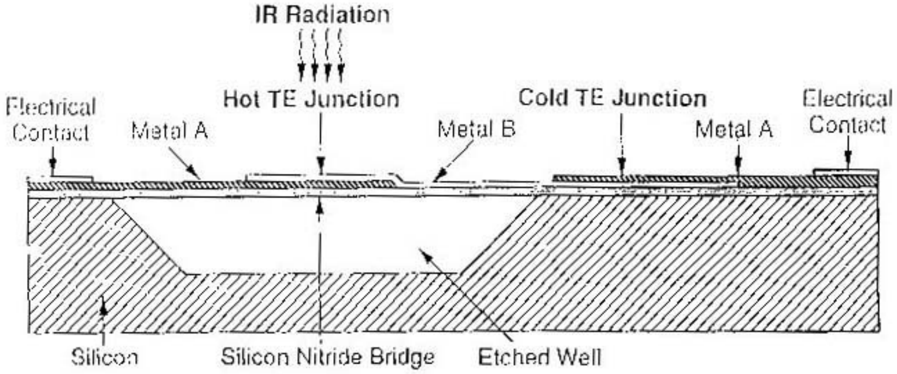

**Figure 3-2.** Monolithic thermoelectric pixel structure.

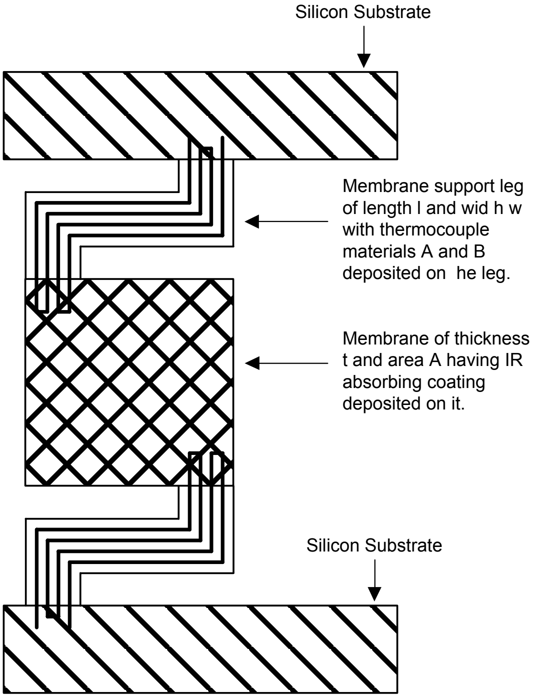
Silicon Substrate
Membrane support leg of length l and width w with thermocouple materials A and B deposited on the leg.
Membrane of thickness t and area A having IR absorbing coating deposited on it.
Silicon Substrate

**Figure 3-3.** Monolithic thermoelectric pixel. From M.C. Foote.[2] Provided through the courtesy of the Jet Propulsion Laboratory, California Institute of Technology, Pasadena, California.

The analysis of the performance of any thermal detection mechanism begins with a heat flow equation. Let temporally modulated thermal radiation fall upon a thermoelectric array and be absorbed by a pixel. The pixel is assumed to be square, having an area $A_D$, a pitch $A_D^{1/2}$, a fill factor $\beta$, and an optical absorption coefficient $\eta$, defined as the fraction of the radiant power falling on the sensitive area which is absorbed by that area. The heat capacity of the thermally isolated membrane (sensitive area) is $C$, expressed in J/°C. The thermal conductance of the principal heat loss mechanism, assumed to be conductance down the legs, is $G$, expressed in W/°C. Then

$$C\frac{d(\Delta T)}{dt} + G(\Delta T) = \eta\beta A_D P_o \exp(j\omega t)\,; \tag{3.1}$$

where $\Delta T$ is the difference in temperature of the hot and reference junctions, $P_o$ is the intensity (W/cm$^2$) of the temporally modulated radiation, $j \equiv \sqrt{-1}$, $\omega$ is the angular modulation frequency of the incident radiation ($\omega = 2\pi f$, where $f$ is the linear frequency) and $t$ is time.

The solution to Eq. (3.1) is

$$\Delta T = \frac{\eta\beta A_D P_o}{G(1+\omega^2\tau_T{}^2)^{1/2}}\,; \tag{3.2}$$

where $\tau_T$, known as the thermal response time or thermal time constant, is

$$\tau_T = \frac{C}{G}\,. \tag{3.3}$$

The units of $\tau_T$ are seconds.

Equation (3.2) shows that the dc temperature rise, i.e., that due to unmodulated radiation, is

$$\Delta T(\omega = 0) = \frac{\eta\beta A_D P_o}{G}\,. \tag{3.4}$$

This heat flow analysis shows that the membrane temperature rise due to the absorbed thermal radiation is inversely proportional to the thermal conductance of the legs. Although this is an especially simple heat flow equation, in that there is no Joulean heating due to a bias current, it will later be seen that even for resistive bolometers and ferroelectric bolometers, which require electrical bias, the temperature rise is inversely proportional to *G*. Attaining excellent thermal isolation is a requirement for attaining excellent performance in uncooled thermal imaging arrays.

## 3.3 Responsivity

Consider now the thermoelectric signal voltage $V_s$, given by

$$V_s = N(S_1 - S_2)\Delta T = N(\Delta S)\Delta T\,; \tag{3.5}$$

where $S_1$ and $S_2$ are the Seebeck coefficients of the materials comprising the junctions, expressed in V/deg K, $\Delta S$ is their difference, and *N* is the number of junction pairs per pixel. Combining Eqs. (3.2) and (3.5) results in

$$V_s = \frac{\eta\beta N(\Delta S) P_o A_D}{G(1+\omega^2\tau_T{}^2)^{1/2}}\,; \tag{3.6}$$

or

$$\Re = \frac{V_s}{P_o A_D} = \frac{\eta\beta N(\Delta S)}{G(1+\omega^2\tau_T{}^2)^{1/2}}\,; \tag{3.7}$$

where $\Re$ is the responsivity in V/W.

## 3.4 Noise

The only type of electrical noise in thermoelectric arrays is Johnson noise, the rms noise voltage $V_N$ of which is given by

$$V_N = (4kTRB)^{1/2}; \tag{3.8}$$

where $k$ is Boltzmann's constant (1.38×10$^{-23}$ J/°C), $R$ is the electrical resistance of the pixel, and $B$ is the electrical bandwidth of the signal processing electronics.

In principle, temperature fluctuation noise and background fluctuation noise can also be present. However, the responsivity of uncooled thermoelectric arrays is low, so that in practice these fundamental noise limits are not attained.

## 3.5 D*

The figure of merit D* is defined by Eq. (1.5) as

$$\mathrm{D}^* = \frac{(A_D B)^{1/2}\Re}{V_N}. \tag{1.5}$$

Inserting Eqs. (3.7) and (3.8) in (1.5) results in

$$\mathrm{D}^* = \frac{\eta\beta N(\Delta S)(A_D)^{1/2}}{2G(kTR)^{1/2}(1+\omega^2\tau_T{}^2)^{1/2}}. \tag{3.9}$$

## 3.6 Noise Equivalent Temperature Difference

The NETD, given by Eq. (1.6), is

$$\mathrm{NETD} = \frac{4F^2 V_N}{\tau_o A_D \Re(\Delta P/\Delta T)_{\lambda_1-\lambda_2}}; \tag{1.6}$$

which, in terms of D*, is

$$\mathrm{NETD} = \frac{4F^2(A_D B)^{1/2}}{\tau_o A_D \quad D^*(\Delta P/\Delta T)_{\lambda_1-\lambda_2}}. \tag{3.10}$$

Inserting Eqs. (3.7) and (3.8) into (1.6) results in

$$\mathrm{NETD} = \frac{8F^2 G(kTRB)^{1/2}(1+\omega^2 \tau_T{}^2)^{1/2}}{\tau_o A_D \eta \beta N(\Delta S)(\Delta P/\Delta T)_{\lambda_1-\lambda_2}}; \tag{3.11}$$

the dc value of which is

$$\mathrm{NETD} = \frac{8F^2 G(kTRB)^{1/2)}}{\tau_o A_D \eta \beta N(\Delta S)(\Delta P/\Delta T)_{\lambda_1-\lambda_2}}. \tag{3.12}$$

## 3.7 Pixel Design Optimization

Volklein, Wiegand, and Baier[1] and Foote,[2] among others,[3] have developed the conditions under which a thin film thermocouple or thermopile on a membrane has maximum D*. The discussion here follows Foote.[2] The conditions are twofold, the first of which is

$$\frac{A_A}{A_B} = \left(\frac{\sigma_B \rho_A}{\sigma_A \rho_B}\right)^{1/2}; \tag{3.13}$$

where $A_A$ is the cross-sectional area of material $A$ which is deposited upon a leg connecting the membrane to the substrate, and $A_B$ is the corresponding value for material $B$. Also $\sigma_A$ is the thermal conductivity of material $A$ and $\sigma_B$ is that of $B$. Also $\rho_A$ is the electrical resistivity of material $A$ and $\rho_B$ is that of material $B$. The second condition is

$$N(\sigma_A A_A + \sigma_B A_B) = 2\sigma_M t w; \tag{3.14}$$

where $\sigma_M$ is the thermal conductivity of the membrane material, e.g., $Si_3N_4$, and $t$ and $w$ are the thickness and width of the legs; it is assumed that there are two identical legs. Equation (3.14) states that the thermal conductance to the substrate through the thermoelectric lines is equal to that through the membrane material. Under these conditions, D* reaches its maximum value, given by

$$\mathrm{D}^* = \frac{Z^{1/2} \tau_T{}^{1/2} \eta \beta}{2^{3/2}(c_M t + c_{abs})^{1/2}(kT)^{1/2}}. \tag{3.15}$$

Here $Z$ is a thermoelectric materials figure of merit given by

$$Z \equiv \frac{\Delta S}{(\rho_A \sigma_A)^{1/2} + (\rho_B \sigma_B)^{1/2}}. \tag{3.16}$$

Also, $c_M$ is the heat capacity per unit volume of the membrane material and $c_{\text{abs}}$ is the heat capacity per unit surface area of the absorbing material. The $Z$ values of selected thermoelectric material pairs are listed in Table 3-1, from Foote.[2]

Furthermore, the thermal response time of the optimized configuration, defined as the ratio of the pixel heat capacity to the thermal conductance of the legs, becomes

$$\tau_T = \frac{C}{G} = \frac{(c_m t + c_{\text{abs}})A\ell}{4\sigma_M t w}; \tag{3.17}$$

where $\ell$ is the length of a leg.

In summary, optimization is in two parts: a) optimizing through choice of thermoelectric materials and b) optimizing through dimensions of the legs. In combination, a wide range of performance, expressed in terms of D*, is possible. In practice, however, for a monolithic array on a silicon substrate, practical considerations arising from silicon process compatibility limit the choices.

**Table 3-1.** *Z* values of thermoelectric junction pairs at 300 K. From M.C. Foote.[2] Provided through the courtesy of the Jet Propulsion Laboratory, California Institute of Technology, Pasadena, California.

| Junction Pair | *Z* |
|---|---|
| Chromel/Constantan | $1.0 \times 10^{-4}$/°C |
| Al/n-polySi or p-polySi | $1.1 \times 10^{-5}$/°C |
| n-polySi/p-polySi | $1.4 \times 10^{-5}$/°C |
| Bi/Sb | $1.8 \times 10^{-4}$/°C |
| $Bi_{0\,87}Sb_{0\,13}$/Sb | $7 \times 10^{-4}$/°C |
| n-PbTe/p-PbTe | $1.3 \times 10^{-3}$/°C |
| n-$Bi_2Te_3$/p- $Bi_2Te_3$ | $2 \times 10^{-3}$/°C |

## References

1. F. Volklein, A. Wiegand and V. Baier, "High-sensitivity radiation thermopiles made of Bi-Sb-Te films," *Sensors and Actuators* **A29**, p. 87 (1991).
2. M.C. Foote, "Microthermopile infrared sensors," Jet Propulsion Laboratory, Pasadena, CA (1998).
3. R.A. Smith, F.E. Jones, and R.P. Chasmar, *The Detection and Measurement of Infra-Red Radiation*, Chapter III, The Clarendon Press, Oxford (1957).

# Chapter 4
# Resistive Bolometers

## 4.1 Introduction

A bolometer is a temperature-sensitive electrical resistor. Its operation is based on its temperature rise caused by absorption of incident radiant energy. The change in temperature causes a change in electrical resistance, which is measured by an external electrical circuit. When the radiation is removed, the temperature of the bolometer returns to its initial value, which is determined by the ambient surroundings in which it is immersed. If the resistance increases with increasing temperature, such as is found with metals, the bolometer is said to have a positive temperature coefficient of resistance; if it decreases with increasing temperature, as is found in semiconductors under most operating conditions, it is said to have a negative temperature coefficient of resistance.

Modern bolometer arrays employ a pixel structure originally developed by Honeywell, Inc. (see Fig. 4-1). It is termed a monolithic structure and is prepared by silicon micromachining. The detecting area is defined by a thin membrane, usually made of silicon nitride ($Si_3N_4$), upon which is deposited a thin film of the detecting material, which is usually semiconducting vanadium oxide ($VO_x$). The membrane is supported above a silicon substrate by means of "legs" made of silicon nitride upon which is an electrically conductive film. The preparation of this structure employs a sacrificial layer of silicon dioxide, later removed, the thickness of which determines the height of the membrane above the substrate. A reflective layer on the substrate below the membrane causes incident infrared radiation that is not completely absorbed by the detecting material to be reflected back through the material, thereby increasing the amount absorbed. This is most effective when the spacing between the absorbing layer and the reflecting layer is one-fourth of the wavelength of the incident radiation. Assuming the incident radiation wavelengths are in the 8–12-µm spectral interval, the spacing is 2.5 µm.

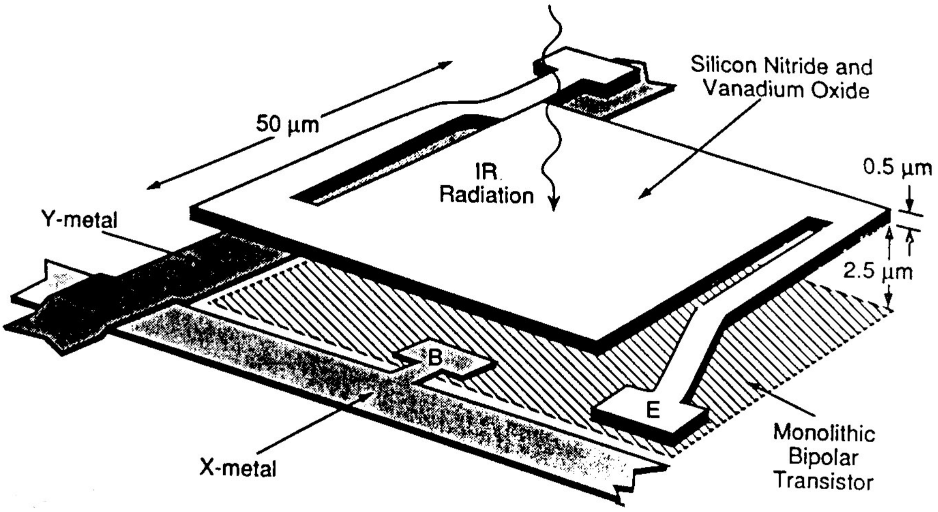
50 µm
IR Radiation
Silicon Nitride and Vanadium Oxide
0.5 µm
2.5 µm
Y-metal
B
E
X-metal
Monolithic Bipolar Transistor

**Figure 4-1.** Microbolometer pixel structure. From R.A. Wood.[2]

## 4.2 Responsivity

A complete and accurate representation of a resistive bolometer pixel is a complex and difficult task. It is also hard to fully grasp the influence and interaction of the various parameters. The analysis below attempts to clarify the operation by describing three cases of increasing complexity.

### 4.2.1 Case I: No Joulean heating; constant bias

Two inputs to the bolometer model are the heat flow equation and the nature of the electrical bias, whether continuous or pulsed. The simplest model, which is widely used, assumes a heat flow equation that omits the Joulean heating of the bias current and also assumes a constant (as opposed to pulsed) electrical bias. This model computes the temperature difference between the silicon substrate and the thermally isolated, radiatively heated, resistive thin film deposited upon a membrane. Heat flows down legs supporting the membrane.

The heat flow equation in this case is that already presented for thermoelectric detectors in Eqs. (3.1) through (3.4). The signal voltage $V_s$, however, is given by

$$V_s = i_b \alpha R \Delta T \; ; \tag{4.1}$$

where $R$ is the electrical resistance, $i_b$ is the bias current, and $\alpha$, the temperature coefficient of resistance, is given by

$$\alpha \equiv \frac{1}{R}\frac{dR}{dT}. \tag{4.2}$$

The thermal response time $\tau_T$ is the same as for thermoelectric detectors, i.e.,

$$\tau_T = \frac{C}{G}. \tag{3.3}$$

The responsivity $\Re$ is obtained by combining the expression for the temperature rise, Eq. (3.2), with that for the signal voltage, Eq. (4.1), then dividing through by the incident radiant power $P_o A_o$, resulting in

$$\Re = \frac{\eta \beta i_b \alpha R}{G(1+\omega^2 \tau_T^2)^{1/2}}; \tag{4.3}$$

The dc responsivity is determined by setting $\omega$=0. It is

$$\Re(\omega = 0) = \frac{\eta \beta i_b \alpha R}{G}. \tag{4.4}$$

Note that the responsivity is inversely proportional to the thermal conductance, which was also true for thermoelectric arrays, see Eq. (3.7).

## 4.2.2 Case II: Joulean heating; constant bias[1]

An increased complexity is introduced when the heat flow equation includes the Joulean heating due to the electrical bias. Furthermore, a load resistor is introduced into the simple circuit (battery, bolometer, load resistor) in order to distinguish between voltage source operation ($R_L$>>$R_B$, where $R_L$ is the load resisitance and $R_B$ is the bolometer resistance) and current source operation ($R_L$ << $R_B$), see Fig. 4-2.

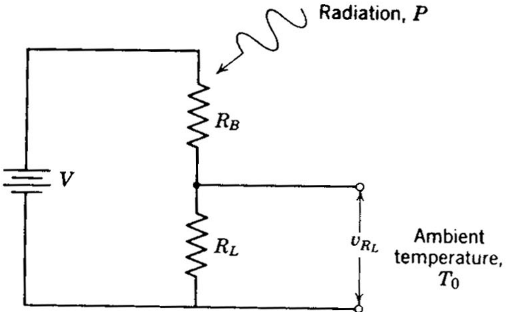

**Figure 4-2.** Bolometer circuit.

The bolometer is in series with $R_L$, the load resistor, and the bias supply of voltage $V$. If the circuit is opened so that no current flows, and if no signal radiation is present, the bolometer is at the ambient temperature $T_o$. Closing the circuit causes current to flow, such that the Joulean heating in the bolometer element $R_B$ increases its temperature to $T_1$. At the same time its resistance changes to a value characteristic of that at $T_1$. If radiation now falls upon the bolometer, its temperature changes by $\Delta$T to the new value $T$. This results in a resistance change in the bolometer, causing a change in the voltage appearing across $R_L$.

The dynamic analysis of the operation is based on use of the heat transfer equation for the bolometer. In the absence of radiation, but with current flowing in the circuit, the equation is

$$C\frac{dT}{dt}+G_o(T_1-T_o)=i^2R_B\,. \tag{4.5}$$

The first term in Eq. (4.5) represents the influence of the heat capacity $C$ on the rate of change of bolometer temperature, and is zero in the steady state condition. The second term represents heat conduction from the bolometer at temperature $T_1$ to its surroundings at $T_o$ through a medium of average thermal conductance $G_o$. In most cases this conduction will be to the substrate, although in ideal operation it represents only radiation interchange with the surroundings. In the latter case, $G_o$ will be a function of $T$. The term on the right is the Joulean heating of the bolometer.

In the presence of signal radiation such that $P_o$ W per unit area are incident upon it, the bolometer changes its temperature to $T$ by the incremental amount $\Delta T$. The heat transfer equation becomes

$$C\frac{d(\Delta T)}{dt}+G(\Delta T)=\frac{d(i^2R_B)}{dT}\Delta T+\eta\beta A_D P_o\exp(j\omega t)\,. \tag{4.6}$$

Here $G$ is the thermal conductance when the bolometer pixel is at temperature $T$, $A_D$ is the pixel area, $\eta$ is the optical absorption coefficient, $\beta$ is the fill factor, $P_o$ is the amplitude of the incident radiation power density which is modulated at angular frequency $\omega$, and $j\equiv\sqrt{-1}$. The first term on the right is

$$\frac{d(i^2R_B)}{dT}\Delta T=\frac{d}{dT}\left[\frac{V^2R_B}{(R_B+R_L)^2}\right]\Delta T=\frac{V^2(R_L-R_B)}{(R_L+R_B)^3}\frac{dR_B}{dT}\Delta T\,. \tag{4.7}$$

The quantity $\alpha$ describing the dependence of bolometer resistance upon temperature is defined as

$$\alpha \equiv \frac{1}{R_B}\frac{dR_B}{dT}. \tag{4.8}$$

For a semiconductor at room temperature, $R_B$ is approximated by

$$R_B = R_{B0}\exp(b/T). \tag{4.9}$$

Thus, for a semiconductor at room temperature,

$$\alpha = -b/T^2. \tag{4.10}$$

For a metal that has a linear dependence of resistance on temperature, that is,

$$R_B = R_{B0}[1+\gamma(T-T_o)], \tag{4.11}$$

$\alpha$ is given by

$$\alpha = \frac{\gamma}{1+\gamma(T-T_o)}. \tag{4.12}$$

Introducing Eqs. (4.7) and (4.8) into (4.6) results in

$$C\frac{d(\Delta T)}{dt} + G\Delta T = \frac{V^2 R_B \alpha}{(R_L+R_B)^2}\left(\frac{R_L-R_B}{R_L+R_B}\right)\Delta T + \eta\beta A_D P_o \exp(j\omega t). \tag{4.13}$$

However, the Joulean heating in the bolometer in the steady state is related to the thermal conduction losses by

$$\frac{V^2 R_B}{(R_L+R_B)^2} = G_o(T_1-T_0). \tag{4.14}$$

Therefore, Eq. (4.13) becomes

$$C\frac{d(\Delta T)}{dt} + G_e\Delta T = \eta\beta A_D P_o \exp(j\omega t); \tag{4.15}$$

where $G_e$, which is referred to as the "effective $G$," is defined as

$$G_e \equiv G - G_o(T_1-T_0)\alpha\left(\frac{R_L-R_B}{R_L+R_B}\right). \tag{4.16}$$

The solution to Eq. (4.15) is

$$\Delta T = \Delta T_o \exp\left(-\frac{G_e}{C}t\right) + \frac{\eta\beta A_D P_o \exp(j\omega t)}{G_e + j\omega C}. \tag{4.17}$$

The first term in Eq. (4.17) represents a transient, whereas the second is a periodic function. If $G_e$ is positive, i.e., if

$$G > G_o(T_1 - T_0)\alpha\left(\frac{R_L - R_B}{R_L + R_B}\right), \tag{4.18}$$

then the transient term goes to zero with time and only the periodic function remains. However, if

$$G < G_o(T_1 - T_0)\alpha\left(\frac{R_L - R_B}{R_L + R_B}\right), \tag{4.19}$$

then the first term in Eq. (4.17) increases exponentially with time, and the bolometer overheats and burns up. If $R_L$ is much greater than $R_B$ and the thermal conductance does not change greatly with temperature, that is, $G \approx G_o$, then the unstable burnout condition is attained when

$$\alpha(T_1 - T_0) > 1. \tag{4.20}$$

For metals, in which α increases with temperature, the inequality described by Eq. (4.20) is not fulfilled and "self-burnout" does not occur. However, for semiconductors, self-burnout can occur at large bias currents. The inequality for self-burnout is

$$\frac{-b}{T_1^2}(T_1 - T_0) > 1. \tag{4.21}$$

Returning to the discussion of Eq. (4.17), it can be seen that under conditions in which the transient term goes to zero, the steady state solution of $\Delta T$ is

$$\Delta T = \frac{\eta\beta A_D P_o}{(G_e^{\,2} + \omega^2 C^2)^{1/2}}. \tag{4.22}$$

The change in bolometer resistance $\Delta R_B$ corresponding to the temperature change $\Delta T$ is, from the definition of α,

$$\Delta R_B = \alpha R_B \Delta T = \frac{\alpha R_B \eta b A_D P_o}{(G_e{}^2 + \omega^2 C^2)^{1/2}}. \tag{4.23}$$

The signal voltage $V_{R_L}$ appearing across the load resistor is

$$V_{R_L} = \frac{d(i_b R_L)}{dR_B} \Delta R_B = -\frac{V}{(R_B + R_L)} \cdot \frac{R_L \Delta R_B}{(R_B + R_L)}. \tag{4.24}$$

Assuming that $R_L >> R_B$, then the bias current $i_b$ does not depend on $R_B$ and $\Delta R_B$. In that case, Eq. (4.24) becomes

$$V_{R_L} = i_b \Delta R_B. \tag{4.25}$$

Because the voltage $V_{R_L}$ depends on $\Delta R_B$ and $\Delta R_B$ depends on the incident power $P_o$, $V_{R_L}$ is the signal voltage, defined as $V_s$. Combining Eqs. (4.25) and (4.24) results in the expression for $V_s$

$$V_s = \frac{\alpha\beta\eta A_D i_b R_B P_o}{(G_e{}^2 + \omega^2 C^2)^{1/2}}. \tag{4.26}$$

The responsivity $\Re$ is given by

$$\Re = \frac{V_s}{P_o A_D} = \frac{\alpha\beta\eta i_b R_B}{(G_e{}^2 + \omega^2 C^2)^{1/2}}; \tag{4.27}$$

or

$$\Re = \frac{\alpha\beta\eta i_b R_B}{G_e (1 + \omega^2 \tau_e{}^2)^{1/2}}; \tag{4.28}$$

where $\tau_e$ is defined as

$$\tau_e = \frac{C}{G_e}. \tag{4.29}$$

Here, $\tau_e$ is known as the “effective thermal response time.” The dependence of $G$ and $\tau$ on temperature due to bias current heating is termed the “electrothermal effect.”

What is the importance of this? It is that $G_e$ is the difference in two terms [see Eq. (4.16)]. The second term must be less than the first or $G_e$ is negative and the bolometer temperature increases exponentially with time, reaching burnout [see Eq. (4.19)]. Equations (4.20) and (4.21) show that this can happen with semiconductors but not with metals. As long as $G_e$ remains positive, increasing the bias current $I_b$ will increase the second term without changing the first. This will reduce the value of $G_e$, thereby increasing the signal voltage and the responsivity. On the other hand, as $G_e$ decreases, the effective response time $\tau_e$ increases, which for some applications may be undesirable.

### 4.2.3 Case III: Joulean heating; pulsed bias

The greatest complexity occurs when the heat transfer equation includes the electrical bias (Joulean) heating and the heating due to the incident absorbed radiant power, but the electrical bias is pulsed rather than continuous. This is frequently the case when large focal plane bolometer arrays are employed. It turns out that the heat transfer equation then is nonlinear, and numerical solutions must be obtained, see Wood[2] and Jansson et al.[3] However, Wood[2] points out that if $\alpha(T_1 - T_0) << 1$, the dc bias equations (i.e., Case II above) and room temperature parameter values (i.e., ignoring the temperature dependence of the parameters due to Joulean heating) "produce numerical results that agree acceptably well—for many applications—with numerical calculations that take into account the full time dependence of the microbolometer parameters." Wood's Fig. 17, reproduced below as Fig. 4-3, provides an example of the results of a numerical calculation using the parameter values listed in his Table II, reproduced below as Table 4-1. The following quote is his description of the data.

> "As an example, Fig. 4-3 shows computed values of some microbolometer parameters, assuming the parameters summarized in Table 4-1 and assuming a net radiation power of 1 nW is absorbed within the microbolometer. The numerical calculations of Fig. 4-3 were performed using a BASIC program and an EXCEL™ spreadsheet, with 10 μsec time increments over an elapsed time of 30 msec, assuming a microbolometer initial temperature of 300 K: the time interval plotted in Fig. 4-3 covers only the last 200 μsec of the 30 msec period, at the end of which the second of two 100-μsec applied bias pulses is assumed to occur. The microbolometer temperature changes very rapidly during the bias pulse—at a rate of VI/C≈50,000°C per second. However, the 100-μsec duration of the bias pulse limits the total temperature increase to about 5°C. During the interval between bias pulses (30 msec) the microbolometer cools, and it reaches about 300.2 K—close to the substrate temperature (300 K)—by the time the next bias pulse begins. At any instant the effective $G$ value is $G_e = P_o A_D / \Delta T$, where $\Delta T$ is the temperature perturbation caused by the presence of $P_o A_D$. This is computed and shown in Fig. 4-3. In the initial part of the time period plotted in Fig. 4-3, $G_e$ is slightly greater than its assumed physical value of $1 \times 10^{-7}$ W/deg K (Table 4-1), because insufficient time has elapsed (30

msec) for the microbolometer to reach the final equilibrium temperature expected from $P_oA_D$. The rapid decrease in $G_e$ to values less than $G$ during the bias pulse is due to the electrothermal effect. The time-dependent microbolometer responsivity is computed and shown in Fig. 4-3. The current responsivity $\Re_I = dI/dP_oA$ is plotted rather than the voltage responsivity $\Re_V$, because, in this example, the microbolometer is assumed to be operated at a constant voltage ($R_L$=0, Table 4-1) during a bias pulse."

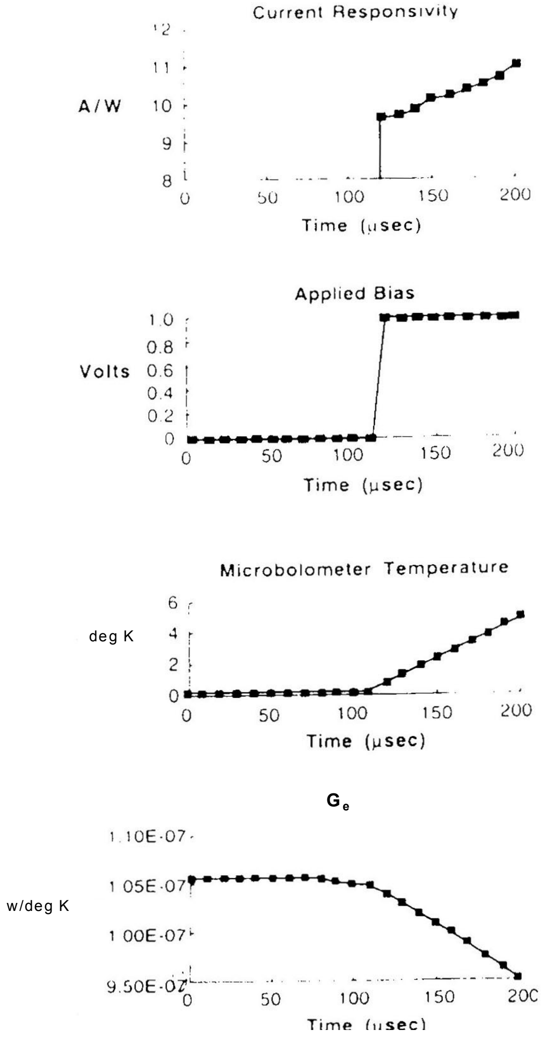

**Figure 4-3.** Numerical calculations made assuming the parameters in Table 4-1 as discussed in the text. $G_e$, effective value of thermal conductance of microbolometer to substrate. From R.A. Wood.[2]

**Table 4-1.** Assumed parameter values for Fig. 4-3. From R.A. Wood.[2]

| Parameter | Value |
|---|---|
| $R(T_s)$ | 20 K Ω |
| $R_L$ | 0 |
| $V_b$ | 1 V |
| $\Delta t$ | 100 μsec |
| $1/F$ | 30 msec |
| $T_s$ | 300 K |
| α | $-0.02\ \mathrm{K}^{-1}$ at 300 K |
| $C$ | $1.0\times10^{-9}$ J/deg K |
| $G$ | $1.0\times10^{-7}$ W/deg K |

## 4.3 Noise

There are four sources of noise in bolometers: Johnson noise, $1/f$ power law noise, temperature fluctuation noise, and background fluctuation noise. These four types of noise are uncorrelated; they add in quadrature, i.e., the total noise voltage is the square root of the sum of the squares of the noise voltages of the four sources. The magnitude of the noise voltage depends on the noise bandwidth. When using pulsed bias, an integrator is employed which limits the noise bandwidth to the frequency interval from 0 Hz to the reciprocal of the integration time, which is chosen to be equal to the pulse duration. In this way, the noise bandwidth $B$ is given by

$$B=\frac{1}{2\Delta t}; \tag{4.30}$$

where $\Delta t$ is the bias pulse duration.

The Johnson noise component of the total noise is given by $V_J$, where

$$V_J=(4kTR_BB)^{1/2}; \tag{4.31}$$

where $k$ is Boltzmann's constant and, as before, $T$ is the bolometer temperature, $R_B$ is the bolometer resistance, and $B$ is the bandwidth corresponding to the integration time.

The $1/f$ power law noise component is approximated by

$$V_{1/f}=(V^2n/f)^{1/2}; \tag{4.32}$$

where

$$V = i_b R_B\,; \tag{4.33}$$

$f$ is the frequency at which the noise is measured, and $n$ is the $1/f$ noise parameter. There is no accurate analytical expression for that parameter. Because $1/f$ power law noise decreases with increasing frequency, the integrated noise over the bandwidth $B$ turns out to be

$$\int_B V_{1/f}\,df = V^2 n \ln\left(\frac{f_2}{f_1}\right). \tag{4.34}$$

Here $f_2$ is the upper frequency limit and $f_1$ is the lower frequency limit. Although $1/f$ power law noise is the dominant noise at low frequencies, it falls below Johnson noise at higher frequencies; the crossover is termed the "knee."

It turns out that for large focal plane arrays that are read out in a serial manner by pulsed bias, the bandwidth $B$ [see Eq. (4.3)], can be sufficiently large that the Johnson noise over that bandwidth is much greater than the $1/f$ power law noise, provided that the $1/f$ power law noise parameter $n$ is sufficiently small. This is true for the standard VOx material for which $\alpha$=0.02/°C used in 240 × 320 pixel bolometer arrays operated at 30 Hz frame time, which are read out in the original Honeywell manner.[2]

In addition to Johnson noise and $1/f$ power law noise, a third form of noise is temperature fluctuation noise, $V_{TF}$ (see Chapter 2). The mean square temperature fluctuations are given by

$$\overline{\Delta T_f^2} = \frac{4kT^2B}{G(1+\omega^2\tau_T^2)^{1/2}}\,. \tag{2.25}$$

These temperature fluctuations cannot be distinguished by the readout mechanism from temperature changes caused by incident radiation that is absorbed by the pixel.

In many cases, the bandwidth $B$ is large enough to include the $\omega\tau_T$ rolloff. In these cases, the mean square temperature fluctuations are given by Eq. (2.24).

$$\overline{\Delta T^2} = \frac{P_o}{4GC}\,. \tag{2.24}$$

Thus the mean square temperature fluctuation noise voltage is

$$\overline{V_{N,TF}^2} = \frac{4kTG\Re^2}{\eta}\,. \tag{4.35}$$

Similarly, the mean square background noise voltage is given by

$$\overline{V_{N,BF}^2} = 8A_D\eta\sigma k(T_D{}^5 + T_B{}^5)\Re^2 . \tag{4.36}$$

Here $T_D$ and $T_B$ are the pixel temperature and the background temperature. The field of view is assumed to be 2π steradians.

The total mean square noise voltage is obtained by adding together the four contributions

$$\overline{V_{N,Tot}^2} = \overline{V_{N,J}^2} + \overline{V_{N,1/f}^2} + \overline{V_{N,TF}^2} + \overline{V_{N,BF}^2} . \tag{4.37}$$

## 4.4 Noise Equivalent Temperature Difference

The NETD is determined by inserting $\left[\left(\overline{V_{N,\mathrm{Tot}}^2}\right)\right]^{1/2}$ for $V_N$ in the NETD expression, employing the appropriate expressions for the responsivity $\Re$ from Cases I, II, and III. The NETD is given by

$$\mathrm{NETD} = \frac{4F^2 V_N}{\tau_o A_D \Re(\Delta P/\Delta T)_{\lambda_1-\lambda_2}} ; \tag{1.6}$$

where $V_N$ is the total noise voltage over the array readout electrical bandwidth, $\tau_o$ is the transmittance of the optics, and $(\Delta P/\Delta T)_{\lambda_1-\lambda_2}$ is the change with respect to temperature of the power per unit area emitted by a blackbody at temperature $T$, measured within the spectral bandwidth between $\lambda_1$ and $\lambda_2$. For $\lambda_1$=8 μm, $\lambda_2$=14 μm, and $T$=295 K, the value for $(\Delta P/\Delta T)_{8-14}$ is $2.62 \times 10^{-4}$ W/cm$^2$ deg K. $F$ is given by

$$F = \frac{1}{2\sin\theta} ; \tag{1.7}$$

where θ is the half angle of the cone of convergence of radiation focused by the optics to the focal point where the array is located.

In practice, assumptions are made about the noise in order to reduce the complexity. The Johnson noise is always included. For Cases I and II in which the bias is constant, $1/f$ power law noise should be included. For Case III, pulsed bias, the readout electrical bandwidth is large; in practice it turns out that $1/f$ power law noise is limited to low frequencies, so that the Johnson noise may exceed $1/f$ power law noise over the bandwidth. Temperature fluctuation noise is included in all cases. As of this writing, background fluctuation noise has not yet been of consequence; that will change as the technology matures.

## 4.5 Choice of Resistive Materials

### 4.5.1 Vanadium oxide

The standard resistive material has been vanadium oxide, VOx, made by sputtering a thin film of the mixed oxides on a $Si_3N_4$ microbridge substrate. The material was developed originally at Honeywell, see Wood.[2] The temperature coefficient of resistance (TCR) versus resistivity is shown in Fig. 4-4. Figure 4-5 illustrates the resistance as a function of temperature for a typical VOx thin film.

The temperature coefficient of resistance, α, is usually quoted as −0.020/°C (2%/°C), yet it can be seen from Fig. 4-4 that higher values can be attained. There are two reasons for not using compositions (x-values) with substantially higher temperature coefficients. First, the scatter in the data shows that reproducibility of properties suffers in the higher x-value films. Second, $i^2R$ heating becomes a problem with high resistivity films. This exacerbates the nonlinear temperature versus time problem during the pulse duration, see Wood.[2]

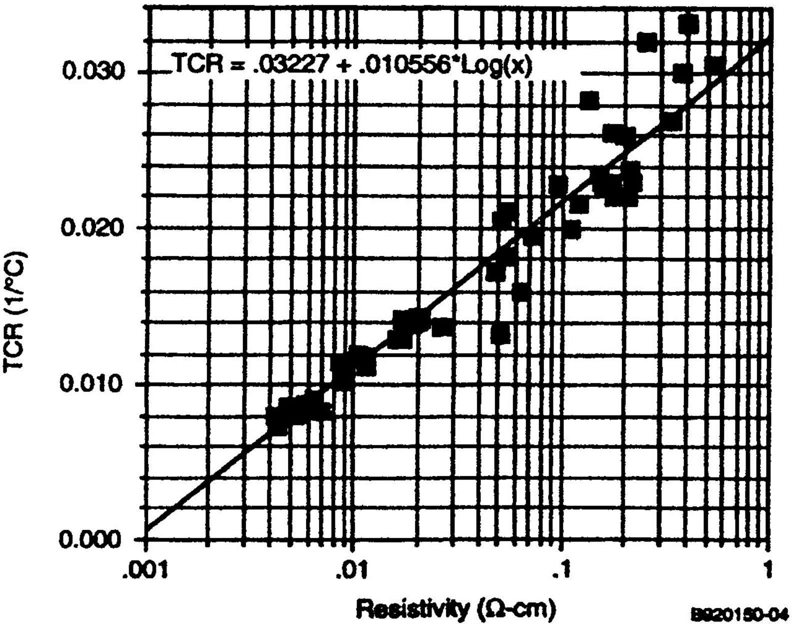

**Figure 4-4.** Temperature coefficient of resistance (TCR) versus resistivity for thin films of mixed vanadium oxides. From R.A. Wood.[2]

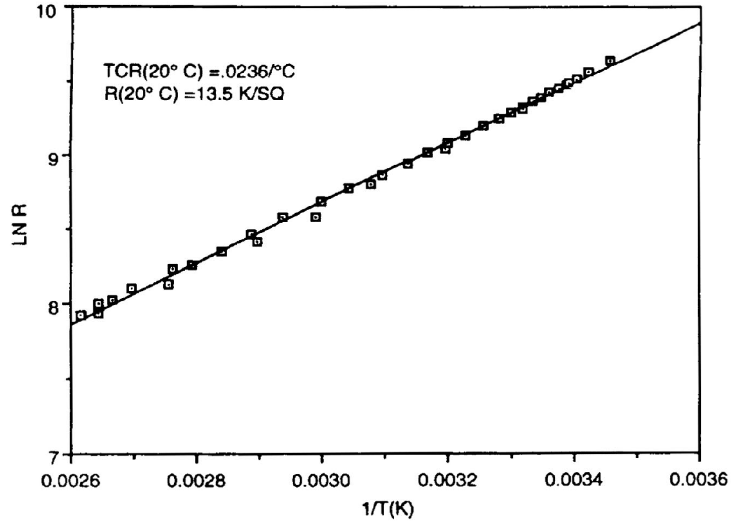

**Figure 4-5.** Resistance versus temperature for thin films of mixed vanadium oxides. From R.A. Wood.[2]

## 4.5.2 Amorphous silicon

Thin-film bolometers based on the use of amorphous silicon (a-Si) have been investigated for at least 15 years. Liddiard[4] has reported room temperature TCR values ranging from $-0.025°C^{-1}$ for doped, low resistivity films to $-0.08°C^{-1}$ for high resistivity materials. Tissot[5] illustrates the relationship between the TCR and the resistivity of a-Si, see Fig. 4-6.

Although high TCR values are attainable, e.g., $-0.08°C^{-1}$, they are accompanied by "an unacceptable level of $1/f$ noise" according to Liddiard.[4] This is not surprising, given the high resistivity of the films. The properties of the films depend upon the method of preparation and the type of dopant, e.g., hydrogen, such films being designated a-Si:H. Non-hydrogenated amorphous silicon films have been prepared with room temperature resistivities in the 500–1000 ohm cm range, but the TCR was about $-0.02°C^{-1}$. Amorphous silicon can be deposited by photo-enhanced chemical vapor deposition (PECVD), a process that is compatible with epitaxy.[6]

Because the typical resistivity of amorphous silicon films is several orders of magnitude higher than that of VOx, a-Si finds application in uncooled arrays in which the bias is continuous rather than pulsed. That is because the signal in bolometers depends on $i_b \alpha R$. where $i_b$ is the bias current, whereas the power dissipation, which causes the rise in pixel temperature, depends on $i_b^2 R$. This is, of course, an oversimplified argument, because pulsed bias is on a given pixel for a very short time, typically a few microseconds, whereas continuous bias is always on each pixel. Nevertheless, design tradeoffs dictate some advantage for a-Si in certain instances.

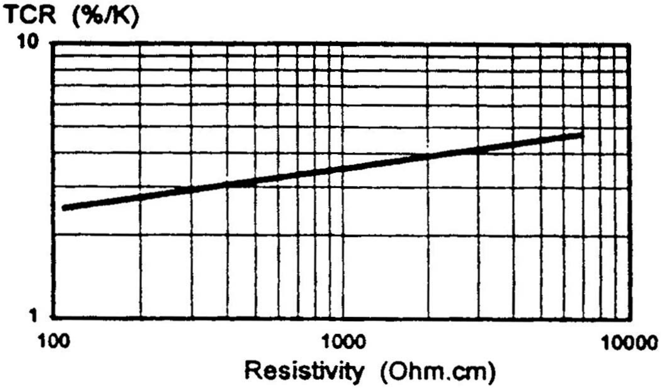

**Figure 4-6.** Evolution of the TCR as a function of the electrical resistivity of a-Si. From Tissot.[5]

## 4.5.3 Thermistor materials

Thermistor (from "thermally sensitive resistor") materials first developed at Bell Laboratories during World War II, are oxides of manganese, cobalt, and nickel that crystallize in the spinel structure. They are semiconductors that exhibit negative temperature coefficient of resistance. Single pixel thermistor bolometers have been commercially available for about 50 years. The principal material investigated is $(MnNiCO)_3O_4$, which has a negative temperature coefficient of resistance of about $0.04°C^{-1}$ at room temperature, and a bulk resistivity of 250 ohm cm.[7]

Because they exhibit a large amount of $1/f$ power law noise arising at grain boundaries, thermistor thin films have not been found to be useful in uncooled bolometer thermal imaging arrays.

## 4.5.4 Titanium

Titanium (Ti) is a metal that in thin film form has a temperature coefficient of resistance of 0.004°C. Although low values of $1/f$ power law noise are found, its very low temperature coefficient of resistance causes it to be of little use in uncooled bolometer arrays.

## 4.5.5 P-N junction diodes

Mitsubishi Electric Corp. has developed an uncooled bolometer array in which the "resistive" material is actually a p-n junction diode that is forward biased. The diodes are deposited in thin film form on silicon-on-insulator thin films. The diodes have low $1/f$ power law noise. A 320 × 240-pixel array has been reported.[8] Low manufacturing cost is said to be a principal advantage.

## References

1. P. W. Kruse, L. D. McGlauchlin, and R. B. McQuistan, *Elements of Infrared Technology*, pp. 345-349, John Wiley and Sons, Inc., New York (1962).
2. R.A. Wood, "Monolithic silicon microbolometer arrays," Chapter 3 of *Uncooled Infrared Imaging Arrays and Systems*, *Semiconductors and Semimetals 47*, P. W. Kruse and D. D. Skatrud, eds., Academic Press, San Diego (1997).
3. C. Jansson, U. Ringh, and K. Liddiard, "Theoretical analysis of pulse bias heating of resistance bolometer infrared detectors and effectiveness of bias compensation," Proc. SPIE Vol. 2552, p. 644 (1995).
4. K.C. Liddiard et al., "Progress of Swedish-Australian research collaboration on uncooled smart IR sensors," Proc. SPIE Vol. 3436, *Infrared Technology and Applications XXIV*, p. 478 (1998).
5. J-L Tissot et al., "LETI/LIR's amorphous silicon uncooled microbolometer development," Proc. SPIE Vol. 3379, *Infrared Detectors and Focal Plane Arrays III* (1994).
6. J.F. Brady, "Advances in amorphous silicon uncooled IR systems," Proc. SPIE Vol. 3698, *Infrared Technology and Applications XXV*, p. 161 (1999).
7. R. Dannenberg, A. Doctor, and S. Baliga, "Electrical and optical properties of $Mn_{1\ 56}CO_{0\ 96}Ni_{0\ 48}O_4$, Proc. SPIE Vol. 3379, p. 16 (1998).
8. T. Ishikawa et al., "Low-cost 320×240 uncooled IRFPA using conventional silicon IC process, Proc. SPIE Vol. 3698, *Infrared Technology and Applications XXV*, p. 556 (1999).

# Chapter 5
# Pyroelectric Arrays

## 5.1 Introduction

Of the three principal uncooled detection mechanisms, the pyroelectric is of the most recent origin. It was originally proposed as an infrared detector by Chynoweth[1] in 1956, and reduced to early practice by Cooper,[2] Putley,[3] and others. Tompsett[4] proposed its use in an uncooled thermal imaging camera tube, which was the first practical application. Uncooled pyroelectric array technology was first developed by Hopper[5] in the U.S. and by Putley,[3] Whatmore,[6] and Porter[7] in the U.K. All of the early pyroelectric arrays were of hybrid construction; the emphasis is now on monolithic construction[8–11] with its superior thermal isolation.

The pyroelectric effect is found in materials such as, but not limited to, ferroelectrics. This discussion emphasizes ferroelectrics; that is the only class that has been widely exploited. Ferroelectrics, such as barium strontium titanate ($Ba_xSr_{1-x}TiO_3$), strontium barium niobate ($Sr_{1-x}Ba_xNb_2O$), lithium tantalate ($LiTaO_3$), and lead titanate ($PbTiO_3$), exhibit internal spontaneous electric polarization, which can be measured as a voltage at electrodes placed on opposite faces of a sample of the ferroelectric material. At a constant temperature of the sample, this internal polarization is neutralized by mobile charges on the surface of the sample; thus there is no voltage difference measured by the electrodes. If the temperature is suddenly changed to a new value, the internal polarization will change, resulting in a measurable voltage difference, which will then be neutralized again by a changed distribution of surface charge. Thus pyroelectric detectors based on ferroelectric materials have no dc signal. The surface temperature must be modulated in time. This is usually accomplished by means of a radiation chopper, but it also can be achieved by constantly moving the infrared image across the material, such as has been employed with pyroelectric vidicon thermal imaging camera tubes.

This chapter deals with the classic pyroelectric effect, which does not employ electrical bias. However, hybrid pyroelectric array technology usually employs an electrical bias to enhance the signal, see Hanson.[8] These hybrid pyroelectric arrays are operated at a temperature just below the Curie temperature, above which the material loses its ferroelectric properties. Just below it, the temperature dependence of the internal polarization has its greatest value. Furthermore, the dielectric constant of the ferroelectric material changes rapidly with temperature near the Curie temperature. Under electrical bias, this provides an addition to the pyroelectric signal; operation in this mode is referred to as a “bias-enhanced pyroelectric detector,” or as a “ferroelectric bolometer.” Arrays operating in this mode require temperature stabilization just below the Curie temperature, which in barium strontium titanate of the optimum composition is about 25°C, a value determined by controlling the barium to strontium ratio during preparation.

Operating the pyroelectric effect at a temperature far below the Curie point greatly reduces the pyroelectric signal if hybrid construction is employed. However, by employing a thin film of pyroelectric material on a silicon microstructure, i.e., a monolithic construction (see Fig. 5-1), the thermal isolation is greatly enhanced, thereby causing the temperature rise to be much greater compared with a hybrid construction. Here hybrid refers to joining together, usually by bump bonding, an array of ferroelectric pixels to an array of silicon pixels that constitute the readout integrated circuit (ROIC) (see Fig. 5-2). Furthermore, the temperature fluctuation noise limit is also greatly reduced, i.e., improved, compared with a hybrid construction. As a result, modern pyroelectric array development is oriented toward silicon microstructure monolithic arrays operated without bias in materials in which the Curie temperature is far above room temperature.[9–12] That is the subject of the following analysis.

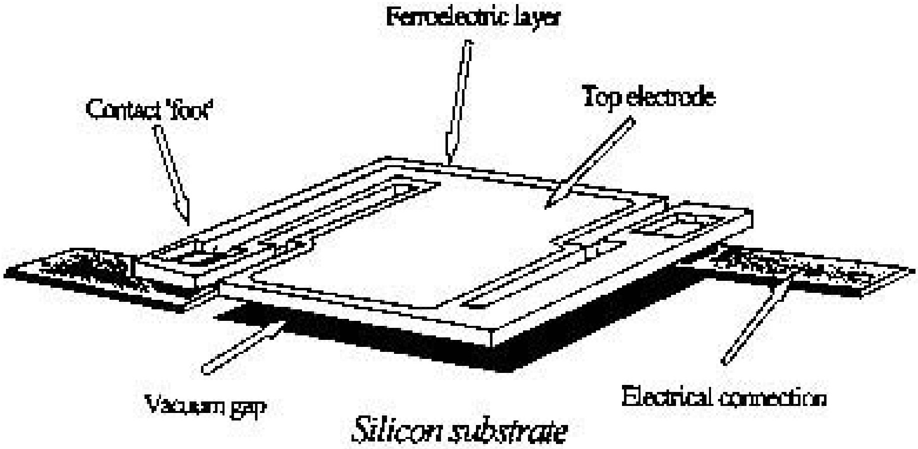

**Figure 5-1.** Ferroelectric monolithic array structure. From R.K. McEwen and P.A. Manning.[12]

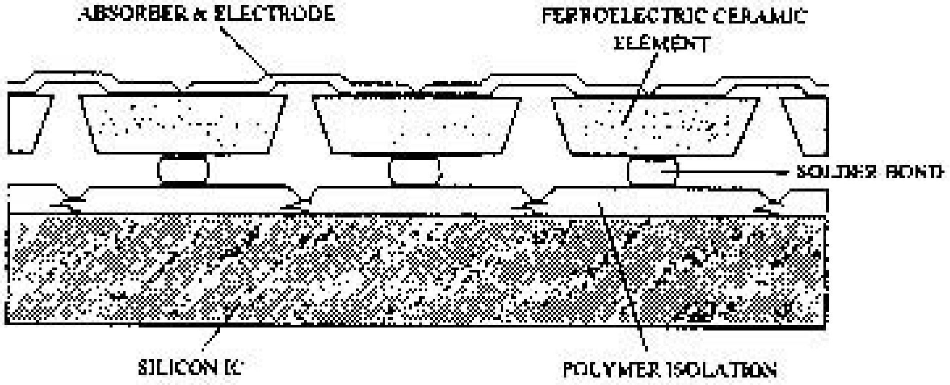

**Figure 5-2.** Ferroelectric hybrid array structure. From R.K. McEwen and P.A. Manning.[12]

## 5.2 The Heat Flow Equation

Because the true pyroelectric effect does not employ electrical bias, the heat flow equation is of the same form as that of the thermocouple. The applicable equation is

$$C\frac{d(\Delta T)}{dt}+G(\Delta T)=\eta\beta A_D P_o \exp(j\omega t), \tag{5.1}$$

where $C$ is the pixel heat capacity, $G$ is the thermal conductance of the heat loss mechanism, $\Delta T$ is the temperature rise due to the absorbed radiant energy, $\eta$ is the pixel absorptance, $\beta$ is the pixel fill factor, $A_D$ is the pixel area, $P_o$ is the amplitude of the sinusoidally modulated incident radiant power, $\omega$ is the angular modulation frequency, $t$ is time and $j\equiv\sqrt{-1}$. The solution of Eq. (5.1) is

$$\Delta T=\frac{\eta\beta A_D P_o \exp(j\omega t)}{G+j\omega C}. \tag{5.2}$$

The rms value of $\Delta T$ is

$$\Delta T=\frac{\eta\beta A_D P_o}{G(1+\omega^2\tau_T^2)^{1/2}}; \tag{5.3}$$

where

$$\tau_T = \frac{C}{G}. \tag{5.4}$$

## 5.3 Responsivity

The internal electric charge difference between opposite faces of the pyroelectric pixel, $\Delta Q$, is given by

$$\Delta Q = pA_D \Delta T; \tag{5.5}$$

where $p$ is defined as the pyroelectric coefficient. If the opposite faces are electrically connected externally, a short circuit current will flow, given by

$$i_s = \frac{d(\Delta Q)}{dt} = pA_D \frac{d(\Delta T)}{dt}. \tag{5.6}$$

From Eq. (5.2)

$$\frac{d(\Delta T)}{dt} = \frac{j\omega\eta\beta A_D P_o \exp(j\omega t)}{G + j\omega C}. \tag{5.7}$$

Substituting Eq. (5.7) into Eq. (5.6) gives

$$i_s = \frac{j\omega\eta\beta p A_D{}^2 P_o \exp(j\omega t)}{G + j\omega C}, \tag{5.8}$$

the rms amplitude of which is

$$i_{s,\mathrm{rms}} = \frac{\eta\beta p A_D{}^2 \omega P_o}{\sqrt{2}G(1+\omega^2\tau_T^2)^{1/2}}, \tag{5.9}$$

where the factor $\sqrt{2}$ is introduced to account for the use of a radiation chopper.

The geometry of a pyroelectric pixel is that of a parallel plate capacitor having electrodes on the upper and lower surfaces. The capacitance is $C_E$. As with all non-ideal capacitors, an internal leakage current flows, the properties of which are characterized by a loss resistance, $R_L$, expressed in terms of a loss tangent, $\tan\delta$, defined as

$$R_L = \frac{1}{\omega C_E \tan\delta}. \tag{5.10}$$

The pixel loss resistance and capacitance together define an electrical response time, $\tau_E$, given by

$$\tau_E = R_L C_E; \tag{5.11}$$

so that

$$\tau_E = \frac{1}{\omega \tan \delta}. \tag{5.12}$$

Although it may seem strange to express a response time in terms of an angular frequency and a loss tangent, capacitive materials are frequently described in that way. The loss tangent is the tangent of the angle between the resistance and the capacitive reactance of a capacitor. The angle should be very small; otherwise the capacitor is "lossy." It will be seen that Johnson noise is associated with the loss resistance.

The output of a pyroelectric pixel is coupled to the input of an amplifier, characterized by an input resistance $R_A$ and an input capacitance $C_A$. These are in parallel with the loss resistance and loss capacitance. The parallel resistance $R_p$ is given by

$$R_p = \frac{R_A R_L}{R_A + R_L}. \tag{5.13}$$

Usually the input capacitance can be neglected with respect to the pixel capacitance.

The short circuit signal current $i_s$ flowing through the parallel resistance $R_p$ generates a signal voltage $V_s$ at the input to the amplifier given by

$$V_s = \frac{i_s R_p}{(1 + \omega^2 R_p{}^2 C_E{}^2)^{1/2}}. \tag{5.14}$$

Combining Eqs. (5.9) and (5.14) gives

$$V_s = \frac{\eta \beta p A_D{}^2 \omega P_o R_p}{\sqrt{2} G (1 + \omega^2 \tau_T{}^2)^{1/2} (1 + \omega^2 \tau_E{}^2)^{1/2}}. \tag{5.15}$$

Equation (5.15) shows that the signal voltage of a pyroelectric pixel exhibits two response times: thermal, based on the pixel heat capacity and thermal conductance of the structure, and electrical, based on the pixel loss resistance in parallel with the amplifier input resistance and the pixel electrical capacitance in parallel with the amplifier input capacitance. The numerator of the equation shows a dependence on angular modulation frequency. This is unique to the pyroelectric effect.

The responsivity $\Re$ of the pyroelectric pixel is given by

$$\Re = \frac{V_s}{P_o A_D} = \frac{\eta \beta p A_D \omega R_p}{\sqrt{2} G (1+\omega^2 \tau_T{}^2)^{1/2} (1+\omega^2 \tau_E{}^2)^{1/2}}. \tag{5.16}$$

This dependence of responsivity on angular modulation frequency is depicted in Fig. 5-3. It is assumed that $\tau_E > \tau_T$, which is the usual case. Note that there is no dc responsivity. At low modulation frequencies, the responsivity rises with frequency due to the factor ω in the numerator of Eq. (5.16). When $\omega^2\tau_E{}^2$ becomes larger than unity, but $\omega^2\tau_T{}^2$ remains smaller than unity, the responsivity reaches a plateau. At higher frequencies at which $\omega^2\tau_T{}^2$ becomes larger than unity, the responsivity becomes inversely proportional to frequency.

In practice, the sharp corners and the flat plateau are not seen. Rather, the responsivity rises, rounds off, and decreases smoothly.

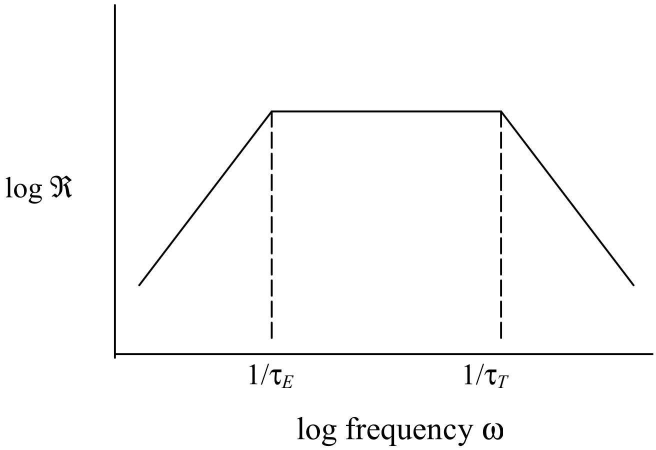

**Figure 5-3.** Pyroelectric detector responsivity as a function of frequency.

## 5.4 Johnson Noise

In resistive materials, Johnson noise is "white," i.e., independent of electrical frequency. In capacitive materials, including pyroelectric materials, Johnson noise is associated with the loss resistance. That noise is not white; it exhibits a frequency dependence due to the product of the loss resistance and the capacitance. The mean square Johnson noise voltage associated with the loss resistance, integrated over all frequencies, and expressed as $\overline{V_{N,LR}}$, is

$$\overline{V_{N,LR}^2} = \frac{kT}{\omega C_E \tan\delta}. \tag{5.17}$$

where $k$ is Boltzmann's constant.

## 5.5 Temperature Fluctuation Noise

The mean square temperature fluctuation noise, $\overline{V_{N,TF}^2}$, is given by

$$\overline{V_{N,TF}^2} = \frac{kT^2 G \Re^2}{C}. \tag{5.18}$$

## 5.6 Noise Equivalent Temperature Difference

The noise equivalent temperature difference is given by Eq. (1.6),

$$\text{NETD} = \frac{4F^2 V_N}{\tau_o A_D \Re (\Delta P / \Delta T)_{\lambda_1 - \lambda_2}}. \tag{1.6}$$

The expression for $V_N$ is $\left(\overline{V_{N,T}^2}\right)^{1/2}$, obtained by adding in quadrature all the noise sources, including Johnson noise, temperature fluctuation noise and background fluctuation noise, then taking the square root.

Common practice is to design the pixel and input electronics so that $\tau_E$ is about 1 sec and so that $\tau_T$ is about 1/3 of the frame time of the array. In the U.S., the TV frame time is 33 msec, so $\tau_T$ is designed to be 11 msec. Thus the system bandwidth extends from approximately dc to $(2\tau_T)^{-1}$, which is 45 Hz.

Furthermore, the input resistance is usually chosen to be orders of magnitude smaller than the leakage resistance, so that $R_p \approx R_A$. Thus the responsivity and Johnson noise in this case are approximated by

$$\Re \approx \frac{\eta \beta p A_D R_A}{\sqrt{2} G \tau_E}, \tag{5.19}$$

$$V_N \approx (4kTR_A B)^{1/2}. \tag{5.20}$$

Introducing Eqs. (5.20) and (5.21) into Eq. (1.6) gives an approximate solution to the NETD of a pyroelectric pixel limited by Johnson noise from the amplifier input.

$$\mathrm{NETD} \approx \frac{8\sqrt{2}F^2 G\tau_E}{\tau_o {A_D}^2 \eta\beta p(\Delta P/\Delta T)_{\lambda_1-\lambda_2}}\left(\frac{kTB}{R_A}\right)^{1/2}. \tag{5.21}$$

As with the other detection mechanisms, that of the pyroelectric must satisfy the fundamental limits set by temperature fluctuation noise, Eq. (2.31) and background fluctuation noise, Eq. (2.32).

## References

1. A. G. Chynoweth, *J. Appl. Phys*. **27**, p. 78 (1956).
2. J. Cooper, *Rev. Sci. Instr*. **33**, p. 92 (1962).
3. E. H. Putley, “The pyroelectric detector,” in *Semiconductors and Semimetals V, Infrared Detectors*, R. K. Willardson and A. C. Beer, eds, Academic Press, New York (1970).
4. M. F. Tompsett, U.S. Patent 3,646,247 (1969).
5. G. S. Hopper, U.S. Patent 4,080,532 (1978).
6. R. W. Whatmore, *Rep. Progr. Phys*. **49**, p. 1335 (1986).
7. S. G. Porter, *Ferroelectrics* **33**, p. 193 (1981).
8. C. M. Hanson, “Hybrid pyroelectric-ferroelectric bolometer arrays,” Chapter 4 of *Uncooled Infrared Imaging Arrays and Systems, Semiconductors and Semimetals 47*, P.W. Kruse and D. D. Skatrud, eds., Academic Press, San Diego (1997).
9. P. W. Kruse, U.S. Patent 5,293,041 (1994).
10. C. M. Hanson et al., “Advances in monolithic ferroelectric uncooled IRFPA technology,” Proc. SPIE Vol. 3379, *Infrared Detectors and Focal Plane Arrays V*, p. 60 (1998).
11. S. G. Porter, R. Watton, and R. K. McEwen, “Ferroelectric arrays: the route to low cost uncooled infrared imaging,” Proc. SPIE Vol. 2552, p. 573 (1995).
12. R.K. McEwen and P.A. Manning, “European uncooled thermal imaging sensors,” Proc. SPIE Vol. 3698, p. 322 (1999).

# Chapter 6

# State of the Art and Technical Trends

## 6.1 Introduction

This chapter presents the state of the art of the principal uncooled focal plane array technologies and the systems that employ them. All data are from current technical publications, rather than manufacturers' literature. Systems based on the three principal detection mechanisms are included (see Chapters 3, 4, and 5). The chapter concludes with a brief review of technical trends in the military and commercial markets for uncooled imagers and imaging radiometers.

## 6.2 Resistive Bolometer Arrays and Their Applications in Thermal Imagers and Imaging Radiometers

### 6.2.1 The Honeywell silicon microstructure resistive bolometer array and thermal imager

Most modern resistive bolometer array technology derives from the pioneering efforts of a team under the direction of R. Andrew Wood at the Honeywell Technology Center that began in 1982. The basis was the following:

- It had been realized for twenty years[1] that the key to bolometer performance was not the resistive material but the thermal isolation structure.
- Silicon micromachining technology, which was under development at Honeywell for low cost, low power sensors of various types, was an ideal technology for providing excellent thermal isolation structures.
- The U.S. Department of Defense, especially DARPA (Defense Advanced Research Projects Agency) and NVESD (U.S. Army Night Vision and Electronic Sensors Directorate) was a source of the many millions of dollars of funding and for technical guidance and military requirements definition, necessary for the full development of uncooled imaging array technology.

As a result, Honeywell Technology Center received military contracts beginning in 1985 which led to the successful development of an uncooled microbolometer array containing 336 columns × 240 rows of 50 × 50-μm pixels operating at the U.S. TV frame rate of 30 Hz.

The chosen resistive material was vanadium oxide, which was known to have a high temperature coefficient of resistance at room temperature and which was process compatible with silicon technology. It was deposited on a "microbridge" of silicon nitride ($Si_3N_4$) by ion beam sputtering, resulting in a mixture of several forms of vanadium oxide, symbolized by VOx. The properties of VOx are shown in Figs. 4-4 and 4-5. Currently, it remains the material of choice, with amorphous silicon emerging as a strong contender.

The original Honeywell approach employed a front-side anisotropic etchant (see Fig. 6-1). This required the electronics to be alongside the sensitive area, thereby reducing the pixel "fill factor," i.e., the fraction of the pixel area that responded to the incident radiation. To improve the fill factor, Honeywell developed a two-level structure (see Fig. 6-1), with the electronics buried in the silicon beneath the bridge. This was achieved through the deposition of a silicon oxide sacrificial layer, 2.5-μm thick, which was removed after the microbridge layer had been deposited, thereby leaving a 2.5-μm gap between the substrate and the microbridge. Figure 6-2 illustrates the process steps. A reflecting layer was deposited on the surface of the silicon below the microbridge. Radiation incident upon the microbridge, whose thickness was less than 1 μm, was not fully absorbed. That part that was transmitted was reflected by the mirror back to the microbridge. The choice of 2.5 μm as the distance from the microbridge to the mirror was driven by the desire to have a resonant optical cavity tuned to the middle of the 8–14-μm spectral interval, where the spectral emittance of the earth peaks and where there is an atmospheric window. In this manner, the optical absorption of the microbridge exceeded 80% throughout the 8–14-μm spectral interval.

A two-level structure requires electrical contacts from the upper level to the lower. This was achieved through "legs" (see Fig. 4-1). These legs reduce the fill factor. On the other hand, they determine the thermal conductance *G*, and therefore the thermal response time for a given pixel size with a standard microbridge thickness, therefore with a standard heat capacity *C*.

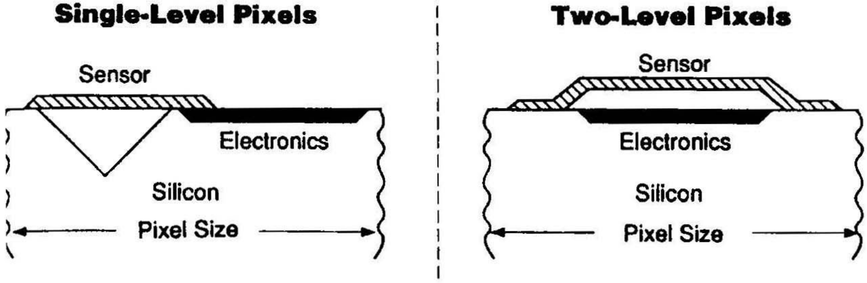

**Figure 6-1.** Illustration of one-level and two-level microbolometer designs. From R.A. Wood.[3]

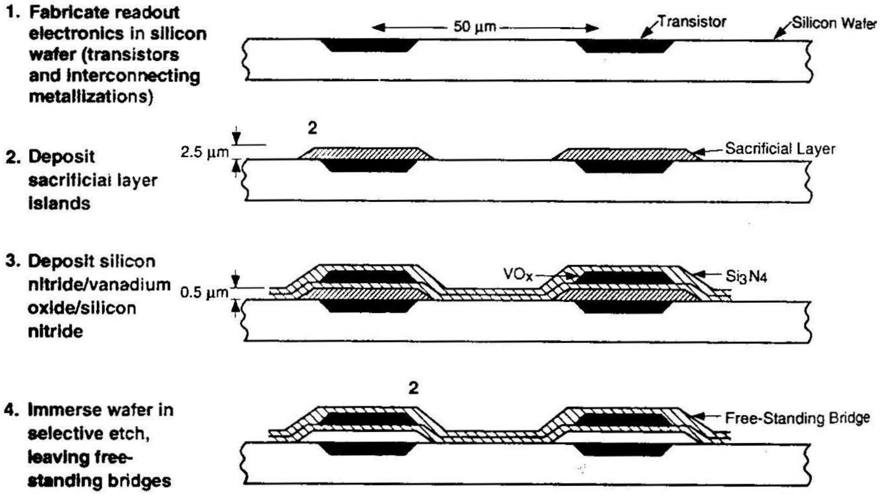
1. Fabricate readout electronics in silicon wafer (transistors and interconnecting metallizations)
50 µm
Transistor
Silicon Wafer
2. Deposit sacrificial layer islands
2.5 µm
2
Sacrificial Layer
3. Deposit silicon nitride/vanadium oxide/silicon nitride
0.5 µm
VOx
Si3N4
4. Immerse wafer in selective etch, leaving free-standing bridges
2
Free-Standing Bridge

**Figure 6-2.** Fabrication sequence for two-level microbolometers. From R.A. Wood.[3]

Another issue that was faced by Honeywell was the need to read out the signal by accessing the pixels sequentially. The method chosen was by pulsing the electrical bias to the pixels sequentially, as described in Sec. 4.2.3 of Chapter 4. The switching was accomplished by implanting a bipolar transistor underneath each pixel. When a bias voltage was applied for about 100 µsec between a given row and column, only that pixel was switched to an "on" state. Bipolar transistors were the best solution to the switching problem given the design rules in place at Honeywell during the late 1980s. Today, CMOS (complementary metal oxide semiconductor) circuits are the usual choice, including at Honeywell.

There were two problems with the switching. First, the pulse current was required to be so high during the pulse that the pixel temperature rose several degrees C during the 100 µsec pulse duration (see Fig. 4-3). On top of that pulse rode the signal, which was of the order of a few thousandths of a degree centigrade. That pulse bias temperature rise had to be subtracted from the total rise to leave only the signal. Nonuniformity in resistance from pixel to pixel required the subtracted amount to vary from pixel to pixel. Furthermore, the radiation falling on the pixel originated not only through the lens but also from the interior of the vacuum package in which the array was mounted. The approach to this problem was to employ a temperature stabilizer upon which the array was mounted within a vacuum package (Fig. 6-3).

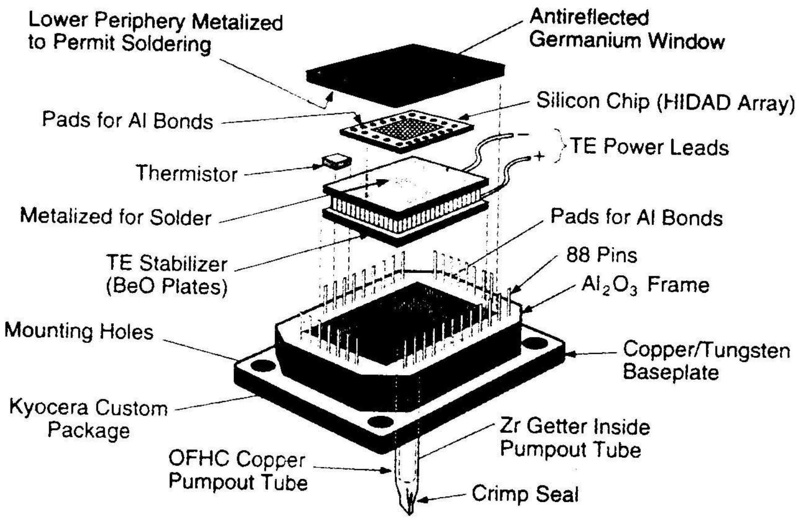

**Figure 6-3.** Construction of a sealed vacuum package for 240 × 336 microbolometer arrays. From R.A. Wood.[3]

The second problem with the switching had to do with the dynamic range and cycle speed of analog-to-digital (ADC) converters available in the late 1980s. In order to correct for pixel nonuniformities and to have a large dynamic range, a 14-bit ADC was required. The cycle speed of those available at the time would not allow 332 × 240, or 80,640, pixels to be digitized 30 times a second. Accordingly, the array was divided into 12 column groups, with 12 parallel outputs, which were then combined into a single frame. Figure 6-4 is a block diagram of the Honeywell imager. The iris is momentarily closed automatically as the focal plane array temperature drifts, so as to renormalize the pixel signals. When the original classified contracts under which the microbolometer was developed became declassified in 1992, Honeywell revealed the details of the development.[2] Subsequently there have been several Honeywell papers, see, for example, the chapter by Wood.[3] The performance at that time is summarized in Fig. 6-5 and Table 6-1.

It is instructive to compare the data of Table 6-1 with the temperature fluctuation noise calculation of Eq. (2.29), plotted in Fig. 2-3. Using the values listed, the temperature fluctuation noise limited NETD [see Eq. (2.29)] is 0.0052°C. The histogram, Fig. 6-5, shows that the mean NETD is 7.5 times that, although the best pixels are only about 5 times that. (All the NETD measurements reported in this chapter and others are for 300 K blackbody sources, *f*/1 optics, and 30-Hz bandwidth unless otherwise specified.)

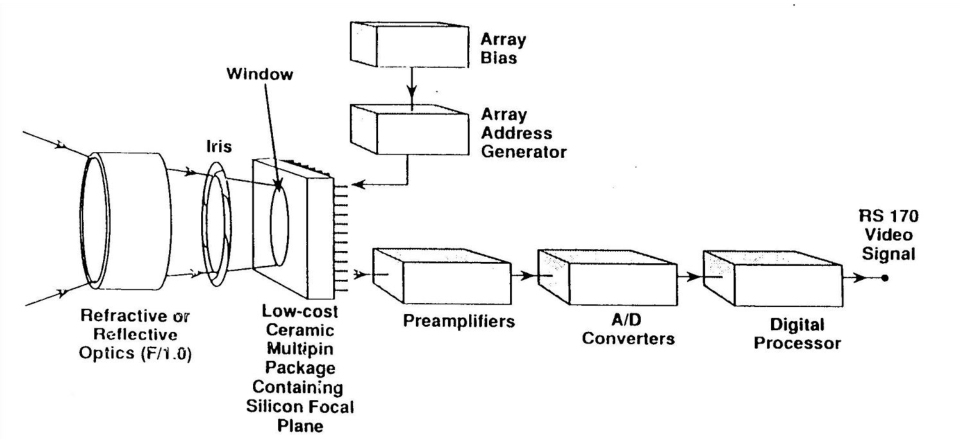

**Figure 6-4.** Block diagram of Honeywell uncooled bolometer imager. From R. A. Wood.[3]

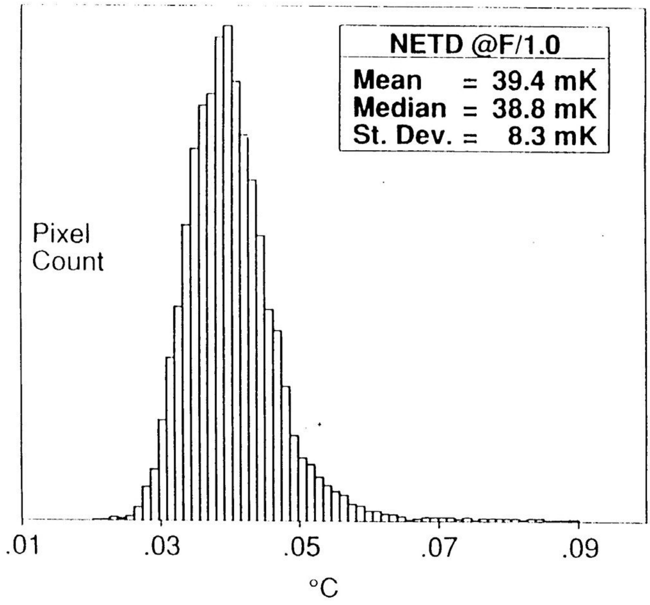

**Figure 6-5.** Measured NETD of 240 × 336 two-level microbolometer arrays of Table 6-1. From R.A. Wood.[3]

**Table 6-1.** Summary of 240 × 336 two-level microbolometer array parameters. From R.A. Wood.[3]

| Parameter | Value |
|---|---|
| Array size | $240 \times 336$ |
| Pixel size | 50 μm |
| Design | Two layer |
| Bridge | $35 \times 35 \times 0.8$ μm $Si_3N_4$ |
| Legs | $50 \times 2 \times 0.8$ μm $Si_3N_4$ |
| Fill factor | 0.70 |
| Package | Vacuum |
| Thermal stabilization | Thermoelectric stabilizer |
| Nominal operating temperature | 25°C |
| Thermal capacity | $3 \times 10^{-9}$ J/deg K |
| Thermal conductance | $2 \times 10^{-7}$ W/deg K (in vacuum) |
| Time constant | 15 msec (in vacuum) |
| Absorptance | 80% mean, 8–14 μm |
| TCR material | 500 Å VOx, TCR = $-0.023$ (deg K)$^{-1}$ |
| Pixel resistance | 20 KΩ |
| Readout | Pulsed constant-voltage, bipolar transistor under each pixel, 14 pixels in parallel, 14 bipolar preamplifiers |
| Field rate | 30 Hz |
| Frame rate | 30 Hz |
| Offset compensation | Intermittent shutter |
| Bias | 5 μsec 250 μA pulses |
| NETD | 0.039°C, *f*/1, 8–14 μm, 300 K target |

When the uncooled bolometer effort began at the Honeywell Technology Center, Honeywell Inc. owned a division that developed and manufactured infrared systems. That division was to have been the recipient of the uncooled technology developed at the Center. However, Honeywell sold that division and the Technology Center decided to license the technology. There were originally four licensees. Following acquisitions and mergers within the defense and aerospace industries, there are now three: British Aerospace (the original Honeywell division), Raytheon, and Boeing, with other licenses pending. The technology advances made by these corporations and others worldwide, including the Honeywell Technology Center, are described below.

## 6.2.2 Improvements on the Honeywell VOx 240 × 332 pixel bolometer array

Currently there remains a great deal of activity on VOx bolometer arrays having a modified Honeywell microbolometer support structure. The improvements fall into the following categories.

### 6.2.2.1 Increase in fill factor

The Honeywell microbridge employed two supporting legs for electrical contact and thermal isolation. The pixel area taken up by the legs reduced the fill factor. Efforts to increase the fill factor include reducing the size of the contacts (“posts”) and use of “buried” legs[4] on an intermediate level between the level of the sensitive area and that of the substrate. However, the buried legs must not interfere with the increased absorption provided by the resonant optical cavity.

### 6.2.2.2 CMOS ROIC

Honeywell employed a bipolar transistor as its pixel switch. Horizontal and vertical pixel addressing circuitry was integrated with the array but most of the analog readout circuitry was off-chip. Because of the lack of availability of A/D converters having sufficient speed (inverse of cycle time) with 14-bit accuracy, the array was segmented into 14 column groups with 14 parallel outputs.

Most of the approaches today employ CMOS silicon circuitry for which the power dissipation is much less than that of bipolar. More of the readout electronics has been moved onto the chip, where it is referred to as the readout integrated circuit (ROIC). The ROIC incorporates parallel column circuitry, consisting of amplifiers, integrators and sample-and-hold circuits with a column multiplexer which provides a single channel output.[5,6] With the improved A/D converters now available, only one is needed. It is usually off-chip but efforts are under way to move it on-chip.

### 6.2.2.3 Smaller pixels

Honeywell employed 50 × 50-μm pixels. It is desirable to reduce the pixel size in order to reduce the cost of the optics. (For a given *f*/no., on which the NETD depends, the cost of the optics made of Ge, the standard material, depends approximately upon the square of the diameter.) However, the NETD is inversely proportional to the pixel area, see Eq. (1.6). Thus, if the pixel size were reduced to 25 × 25 μm, and everything else remained the same, the NETD would increase by a factor of four. Improvements in the readout electronics are needed to compensate for this. A 240 × 320 pixel array with 25-μm pixels having an NETD of 0.052 K (52 mK) is under development.[7]

#### 6.2.2.4 640 × 480 pixel arrays

The development of a 640 × 480 pixel array employing 25 × 28-μm pixels is under way.[8] A focal plane array has been built and tested. The NETD is 0.113 K.

#### 6.2.2.5 160 × 120 pixel arrays

Thermal imagers with 160 × 120 pixel arrays with 50 × 50-μm VOx pixels have been developed[9,10] with NETD values <0.1 K. The principal advantage of these smaller arrays over 320 × 240 arrays is cost reduction. More than four times as many small arrays can be obtained from one processed silicon wafer; the yield is higher and the off-chip electronics are simpler. In addition, the imagers require less electrical power and have smaller optics.

#### 6.2.2.6 Removal of temperature stabilizer

The original Honeywell VOx bolometer array incorporated a thermoelectric temperature stabilizer to simplify the problem of pixel nonuniformity correction. However, the stabilizer consumes power and adds weight. Therefore, for some applications, such as that of unattended ground sensors, it is desirable to remove the temperature stabilizer. This has been achieved by calibration of each pixel over the expected range of ambient temperature.[11]

### 6.2.3 Use of amorphous silicon rather than vanadium oxide as the resistive material

Section 4.5.2 of Chapter 4 described the properties of amorphous hydrogenated silicon (a-Si:H) as a substitute for VOx in uncooled focal plane arrays. The presumed advantage of amorphous silicon is that its resistivity is sufficiently high that it can be continuously biased, rather than pulse biased, without excessive Joulean heating of the focal plane array.

Progress in the development of amorphous hydrogenated silicon uncooled focal plane arrays in the U.S.[12] and in France[13,14] has been reported. Amorphous hydrogenated silicon has a metastable state caused by defects arising from prolonged illumination. This is an undesirable feature that requires a specific annealing cycle during preparation. If not removed, it adversely affects long-term reliability.[14] Nevertheless, 320 × 240 uncooled arrays have been developed with an average NETD of 0.070 K.

### 6.2.4 Use of diodes rather than resistive materials

Instead of a resistive material as the temperature sensing element, Ishikawa et al.[15] have investigated the use of p-n junction diodes fabricated on silicon-on-insulator (SOI) substrates. The temperature dependence of the forward characteristic of the diode is measured. Rather than a microbridge structure, an absorbing film over the diode is employed. A 320 × 240 array using 40 × 40-μm pixels has been constructed. The NETD is reported to be 0.2 K.

### 6.2.5 Thermal imagers employing uncooled VOx bolometer arrays

Examples of thermal imagers employing 320 × 240 pixel VOx bolometer arrays now being marketed are Raytheon's AE-189[7] and Sanders Lockheed Martin's (now British Aerospace) LTC500.[16] Table 6-2 lists the performance parameters of the AE-189. Table 6-3 lists the performance parameters of the LTC500. These have been chosen as examples of derivatives of the original Honeywell work and not as product recommendations.

Boeing is marketing packaged 320 × 240 pixel VOx bolometer arrays (the product name of which is the V3000[17]) and is developing the V4000.[18] Thermal imagers employing 160 × 120 pixel VOx bolometer arrays have been developed[19,20] and are entering the marketplace. Again, these are not product recommendations. This is a rapidly evolving technology and market in which uncooled bolometric thermal imagers from worldwide suppliers are emerging.

### 6.2.6 Imaging radiometers based on 320 × 240 pixel uncooled VOx bolometers

An imaging radiometer is an imager with the additional capability of measuring the temperature of any point of a scene. It finds applications in the commercial and industrial world, principally in predictive and preventive maintenance and in process control.

Until the advent of uncooled imagers, imaging radiometers largely employed cryogenic focal plane arrays such as (Hg,Cd)Te (mercury cadmium telluride) and InSb (indium antimonide). With the advent of uncooled bolometer arrays and imagers, uncooled imaging radiometers have been developed. Because of the requirement for a large, linear dynamic temperature range, hybrid pyroelectric or hybrid ferroelectric bolometer arrays may be unsuitable for imaging radiometers. Uncooled thermoelectric arrays are suitable, and their application to imaging radiometers is discussed later in this chapter.

**Table 6-2.** Summary of performance characteristics of AE-189 microbolometer FPA. From W. Radford et al.[7]

| **Performance Parameter** | **Capability (*f*/1.0 and 300 K Scene)** |
|---|---|
| Array configuration | 320 × 240 |
| Pixel size | 50 × 50 μm |
| Overall chip dimensions | 18.1 × 17.1 mm |
| Spectral response | 8–14 μm |
| Signal responsivity | $> 5 \times 10^6$ V/W or 10 mV/$K_{scene}$ |
| NETD @ *f*/1 | < 100 mK |
| Output offset nonuniformity | < 300 mVp-p |
| Output noise | 1.0 mV RMS |
| Intrascene dynamic range @ *f*/1 | > 200 K |
| Uncorrected responsivity nonuniformity | < 4% (sigma/mean) |
| Pixel operability | > 99.5% |
| Crosstalk (nearest neighbor) | < 1% (combined optical and electrical) |
| Power dissipation | 75 mW |
| Nominal operating temperature | 20°C |

**Table 6-3.** Sanders Lockheed Martin LTC500 thermal imager technical specifications. From T. Breen et al.[16]

| **LTC500 Camera Technical Specifications** | |
|---|---|
| Standard imaging module | SIM100 |
| Spectral response | 8–14 μm |
| Available horizontal FOV | 4.3°–50.6° |
| IFOV for 5.6° system | 0.3 mrad |
| Video output | RS-170/NTSC or PAL |
| Digital output options | 15 bit real time |
| Array format | 327 × 245 |
| NETD (*f*/1, 30 Hz) | < 100 mK |
| Frame update rate | 60 Hz |
| Size (including 40° lens) | 4.5 in. (H) × 5.0 in. (W) × 12.6 in. (L) |
| Weight (including 40° lens) | 5.5 pounds |
| Power | 4-29 V DC, < 10 W |

Uncooled imaging radiometers employing resistive bolometer arrays are basically uncooled imagers that have calibrated pixels, the calibration coefficients having been stored in memory and stored algorithms employed with a microprocessor to calculate temperature by means of the output signal from each pixel. The calibrations must provide a continuous curve of the output voltage of every pixel as a function of temperature from a standard blackbody over a wide dynamic range. Furthermore, each of these pixel calibrations must be in terms of the ambient temperature of each pixel over a range of ambient temperatures. A description is provided by Meyer and Hoelter.[21] The present technology is based on 320 × 240 VOx arrays.

### 6.2.7 Summary

The de facto standard resistive microbolometer array, a derivative of the original Honeywell array, has the following features:

- Silicon microstructure
- VOx resistive material
- 50 × 50-μm pixels
- Response time of 12 msec
- 30-Hz frame rate
- 8–14 μm spectral response
- NETD of 0.05 K (blackbody temperature = 300 K, frame rate = 30 Hz, *f*/1 optics)

These arrays are employed in commercially available uncooled thermal imagers and imaging radiometers.

VOx uncooled thermal imagers employing 160 × 120, 50 × 50-μm pixels with NETD < 0.1 K (blackbody temperature = 300 K, frame rate = 30 Hz, *f*/1 optics) are becoming available commercially.

Under development are 640 × 480 pixel arrays having 28 × 28-μm pixels. The NETD of 0.113 K is expected to improve substantially.

Alternative materials, especially hydrogenated amorphous silicon, are candidates to replace VOx.

## 6.3 Pyroelectric and Ferroelectric Bolometer Uncooled Arrays and Thermal Imagers that Employ Them

### 6.3.1 Introduction

The worldwide development of pyroelectric and ferroelectric bolometer arrays stems principally from efforts at two corporations, namely, Texas Instruments (now Raytheon) in the U.S. and GEC Marconi (now British Aerospace) in the United Kingdom. The U.S. effort, funded by DARPA and U.S. Army CECOM

NVESD, which was the larger effort, will be the principal subject of this discussion.

### 6.3.2 The Texas Instruments (now Raytheon) hybrid ferroelectric bolometer array and imagers

In contrast to the Honeywell effort that employed a silicon microstructure for thermal isolation, the Texas Instruments effort employed a hybrid structure. In this approach, a silicon substrate with embedded electronics at each pixel was prepared separately from the detecting material, which was then bump-bonded to the substrate at each pixel. The detecting material was barium strontium titanate, a ceramic whose ferroelectric properties, including the Curie temperature, could be adjusted by the barium-to-strontium ratio. Rather than operating as a pyroelectric detector, this focal plane array was operated as a ferroelectric bolometer, also known as a bias-enhanced pyroelectric detector. Like the Honeywell resistive bolometer development, the Texas Instruments ferroelectric bolometer development was an outstanding success. On the other hand, the hybrid structure (in which the thermal isolation capability is limited by the thermal conductance of the bump bonds) has limited the potential for performance improvement, especially a better (lower) NETD.

The description of the pyroelectric effect in Chapter 5 did not include electrical bias enhancement. The reasons are twofold: the subject is extremely complex, and future developments will most likely be limited to pyroelectric detectors without bias enhancement on silicon microstructure substrates. The best source of information on the hybrid ferroelectric bolometer is the chapter by Hanson[22] who led the Texas Instruments ferroelectric bolometer development. Like the Honeywell resistive bolometer development, that effort was classified until mid-year 1992. A brief description of the operation is presented here.

In contrast to the pyroelectric effect on silicon microstructures, in which the Curie temperature is far above the operating temperature of the pyroelectric effect, the hybrid ferroelectric effect is stabilized at a temperature just below the Curie temperature. (Recall that the Curie temperature is the temperature above which a material loses its ferroelectric properties). As Fig. 6-6 shows, the slope of the ferroelectric polarization versus temperature is highest at that point. (Recall that the ferroelectric polarization is the electric dipole moment per unit volume of material; the pyroelectric coefficient is the slope of the polarization versus temperature curve at the operating temperature; and the pyroelectric current is proportional to the pyroelectric coefficient and the rate of change of temperature with respect to time.)

Consider now the dependence of the dielectric permittivity with temperature on either side of the Curie temperature. The pyroelectric pixel is a capacitor; like all capacitors, its capacitance depends on its dielectric constant or relative permittivity. Figure 6-7 shows that near the Curie temperature, the relative permittivity changes rapidly with temperature. If only the change in relative

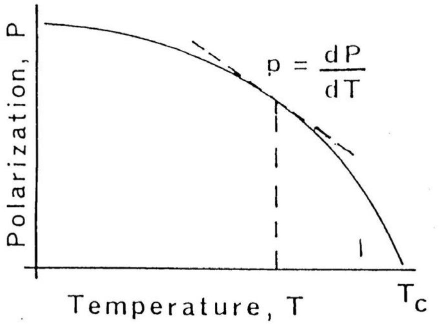

$$i_s = pA\frac{dT}{dt}$$

$P$ = Polarization = electric dipole moment per unit volume of material (Coul/cm$^2$)
Electric dipole moment = surface charge multiplied by average distance between positive and negative charges (Coul cm)

$p$ = Pyroelectric coefficient (Coul/cm$^2$ °C)

$T$ = Temperature (°C)

$T_c$ = Curie temperature (°C)

$t$ = Time (sec)

$A$ = Area of pyroelectric sample (cm$^2$)

**Figure 6-6.** The pyroelectric effect.

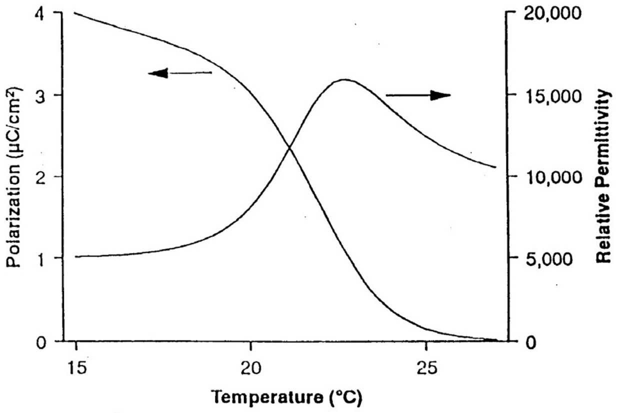

**Figure 6-7.** Temperature dependence of spontaneous polarization and dielectric permittivity for ferroelectric ceramic barium strontium titanate (BST). From C. M. Hanson et al.[23]

permittivity with temperature is monitored, which can only be done by means of an electrical bias, the device is termed a “dielectric bolometer.” Operation in this mode has been explored by Noda et al.[24] On the other hand, if simultaneous operation in both the pyroelectric and dielectric bolometer modes is employed, the detector is referred to as a “ferroelectric bolometer” or a “bias-enhanced” pyroelectric detector. Figure 6-8 illustrates the dependence of responsivity on temperature and applied voltage of a Texas Instruments barium strontium titanate ferroelectric bolometer.

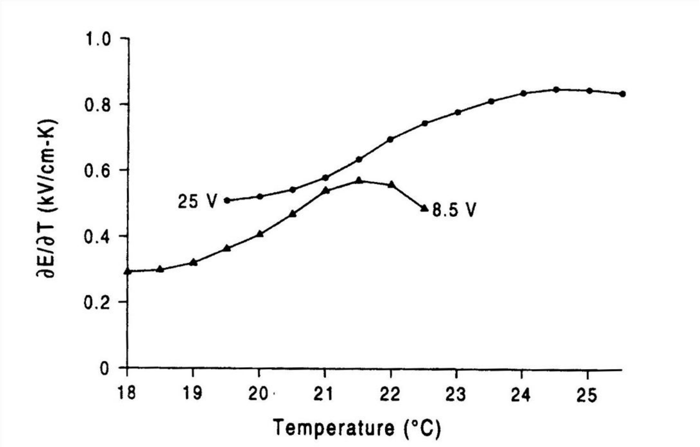

**Figure 6-8.** Pyroelectric material responsivity figure of merit [$\partial E/\partial T)_D = p/\varepsilon\varepsilon_o$] for a ceramic $Ba_{0.67}Sr_{0.33}TiO_3$ (barium strontium titanate) sample 25-μm thick, at two different bias voltages. From C. M. Hanson.[23]

The construction and performance of the Texas Instruments hybrid ferroelectric bolometer array has also been described by several authors.[25,26] Figure 6-9 shows the construction of the array. Under each pixel is the readout integrated circuit (ROIC) illustrated in Fig. 6-10. As pointed out in Eq. (5.16), there is both a thermal and an electrical time constant for a pyroelectric detector. The combination of these with the ROIC effectively limits the noise (and signal) of the Texas Instruments hybrid ferroelectric bolometer from about 1 Hz to about 200 Hz. Of course, there is no dc signal; a radiation chopper must be employed.

How well did the Texas Instruments ferroelectric bolometer operate when declassified in 1992? The best NETD measured was about 0.04°C for a 300 K blackbody and *f*/1 optics, essentially the same as that of the Honeywell resistive bolometer. How can this be, since the Honeywell monolithic resistive bolometer has superior thermal isolation compared with the Texas Instruments hybrid ferroelectric bolometer? The reason is that the Texas Instruments device is almost temperature fluctuation noise limited whereas the Honeywell one is not. Referring to Eq. (2.29), it can be seen that for a Texas Instruments thermal conductance $G$ of about $2\times10^{-6}$ W/deg K, the 300 K temperature fluctuation noise limit is about 0.020 K, whereas for a Honeywell $G$ value of about $1\times10^{-7}$ W/deg

K, the temperature fluctuation noise limit is about 0.005 K. In other words, excess electrical noise in the wider electrical bandwidth (compared with Texas Instruments) and a responsivity limited by the Joulean heating of the pixels by the bias current prevented the Honeywell device from being at the temperature fluctuation noise limit.

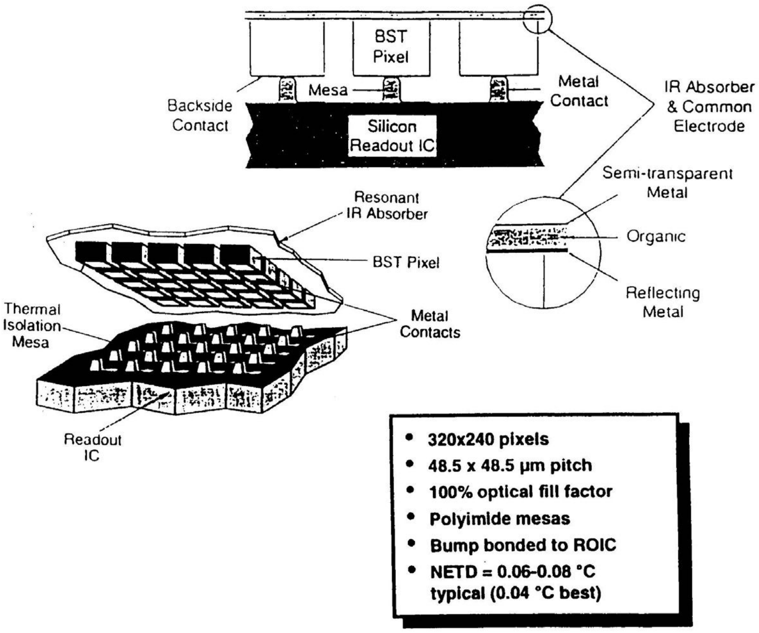

- **320x240 pixels**
- **48.5 x 48.5 μm pitch**
- **100% optical fill factor**
- **Polyimide mesas**
- **Bump bonded to ROIC**
- **NETD = 0.06-0.08 °C typical (0.04 °C best)**

**Figure 6-9.** The Texas Instruments (now Raytheon) hybrid ferroelectric bolometer array. From C. M. Hanson et al.[23]

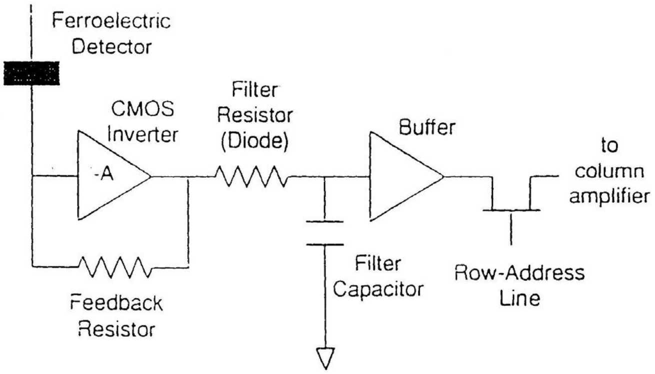

**Figure 6-10.** Read-out integrated circuit for Texas Instruments (now Raytheon) hybrid ferroelectric array. From C. M. Hanson et al.[23]

Even though the hybrid design limits the performance of the Texas Instruments (now Raytheon) ferroelectric bolometer, its performance is good enough for many applications. These include use by the police, by firefighters, for drivers' vision enhancement and many others. Currently it is more widely used than resistive bolometer systems, although this will probably change in the near future.

### 6.3.3 Monolithic pyroelectric array development

Because the hybrid design is difficult to improve, Raytheon[27] and British Aerospace[28] are developing monolithic pyroelectric arrays (see Fig. 6-11). These devices are in early development; whether they will be competitive in performance and cost with the monolithic resistive bolometer arrays remains to be seen. Their need for a radiation chopper may limit their use in some applications.

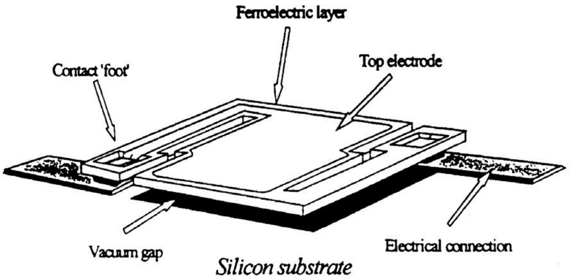

**Figure 6-11.** Silicon microstructure monolithic pyroelectric array. From R. K. McEwen and P. A. Manning.[28]

## 6.4 Uncooled Thermoelectric Arrays and Thermal Imagers and Imaging Radiometers that Employ Them

### 6.4.1 Introduction

Although uncooled thermoelectric arrays can have D* values comparable to uncooled pyroelectric, ferroelectric bolometer, and resistive bolometer arrays, much less effort has been made in their development. The reason is that their responsivity (and also their noise) is orders of magnitude less. Thus their application in thermal imaging systems requires very low-noise electronics to realize their performance potential. Because the signal-to-noise ratio is a function of system bandwidth, which is directly related to imager frame rate, they have found almost no use as matrix arrays in TV frame rate imagers. Instead, they are employed as linear arrays that are mechanically scanned to form an image of stationary or nearly stationary objects. Their inherent linearity with incident radiant power, and their very large dynamic range, are attractive features for industrial radiometry, such as in predictive and preventive maintenance. They also find application in space systems such as horizon scanners and planetary imagers where their unbiased operation minimizes system power drain.

The state of the art of thermoelectric arrays and their applications is discussed below, as reflected by the scientific and engineering literature. The first example is that of high performance monolithic linear arrays. That is followed by a description of an imaging radiometer employing a linear array.

## 6.4.2 Monolithic linear arrays

Foote and colleagues[29] have described the preparation and performance of bismuth tellurium (Bi-Te) and bismuth antimony tellurium (Bi-Sb-Te) monolithic linear arrays of several geometrics. Common to all is the use of a silicon nitride membrane over a cavity in a silicon substrate. Table 6-4, from Foote and Jones,[30] lists the parameters of four types of arrays shown in Figs. 6-12(a) through (d) which differ in pixel size and number of thermocouples per pixel. Compared with most other thermoelectric arrays, their D* values are exceptionally high. Figure 6-13, from Foote and Jones,[30] compares the performance of their arrays with 12 others reported in the literature.

**Table 6-4.** Geometry and measured performance of four thermopile arrays shown in Figs. 6-12(a) through (d). From M.C. Foote and E.W. Jones.[30]

| **Parameter** | **Device Type 1** | **Device Type 2** | **Device Type 3** | **Device Type 4** |
|---|---|---|---|---|
| Detector length (μm) | 1,500 | 184 | 176 | 70 |
| Pixel pitch (μm) | 75 | 104 | 104 | 54 |
| Number of thermocouples per pixel | 11 | 1 | 5 | 1 |
| Number of devices tested | 126 | 21 | 31 | 19 |
| Resistance (Ω) | 40,000 | 2,900 | 12,000 | 1,650 |
| dc infrared responsivity (V/W) | 1,100 | 1,120 | 1,060 | 866 |
| Response time (ms) | 99 | 83 | 23 | 15 |
| D* (1000 K, 0 Hz) ($10^8$ cm $Hz^{1/2}$/W) | 14 | 22 | 9.8 | 9.7 |

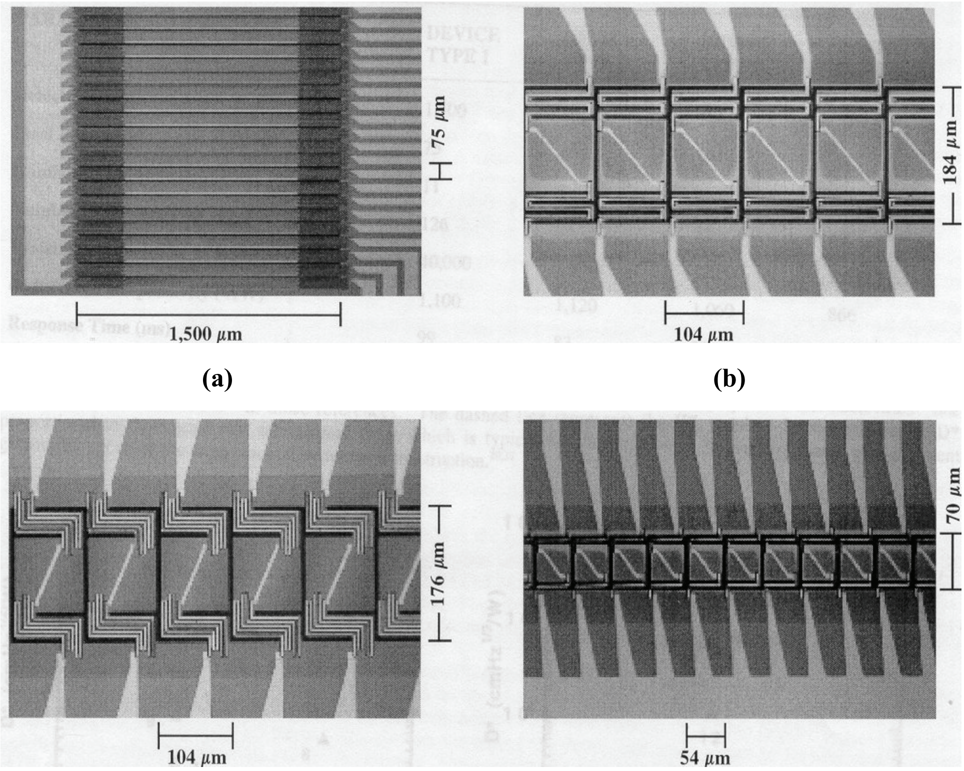

(a) (b)

(c) (d)

**Figure 6-12.** Four types of uncooled thermopile arrays: (a) Array of type 1 thermopile devices. The 0.6-µm thick device membranes connect to the silicon substrate at the left and right sides. Each pixel has 11 Bi-Te/Bi-Sb-Te thermocouples in series. These long, thin devices were designed to geometrically match a spectrometer. (b) Array of type 2 thermopile devices. The 0.6-µm thick device membranes connect to the silicon substrate at the top and bottom. Each pixel has one Bi-Te/Bi-Sb-Te thermocouple. (c) Array of type 3 thermopile devices. The 0.6-µm thick device membranes connect to the silicon substrates at the top and bottom. Each pixel has five Bi-Te/Bi-Sb-Te thermocouples in series. (d) Array of type 4 thermopile devices. The 0.6-µm thick device membranes connect to the silicon substrate at the top and bottom. Each pixel has one Bi-Te/Bi-Sb-Te thermocouple. From M.C. Foote and E.W. Jones.[30] Provided through the courtesy of the Jet Propulsion Laboratory, California Institute of Technology, Pasadena, California.

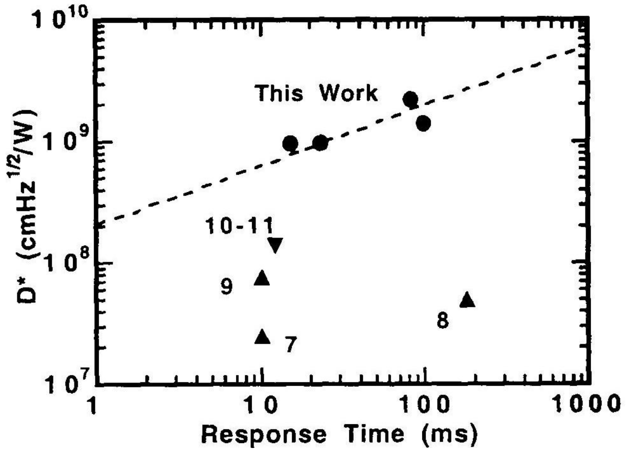

Figure 6-13. Representative data from the literature showing reported D* values as a function of response time for thin film thermopile linear arrays. Thermoelectric materials are Bi-Te/Bi-Sb-Te (this work) (ℓ), constantan/chromel (↔), and silicon (←). The dashed line represents the Foote and Jones results. Its slope indicates D* proportional to the square root of response time, which is typical for thermopiles or bolometers with different geometries and the same material system. From M.C. Foote and E.W. Jones.[30] See Foote and Jones[30] for identification of the numbered data points. Provided through the courtesy of the Jet Propulsion Laboratory, California Institute of Technology, Pasadena, California.

## 6.4.3 Imaging radiometer employing linear thermoelectric arrays

McManus and Mickelson[31] and Kruse[32] have described the construction, performance, and applications of an imaging radiometer that employs a 120-pixel linear array of chromel-constantan thermopiles, each thermopile consisting of three series-connected thermocouples with a pitch of 50 μm (see Table 6-5). These thin-film thermocouples are deposited on a silicon nitride membrane over an etch pit in a silicon substrate (see Fig. 3-2). To provide a thermal image of a scene, a stepper motor drives the vertically oriented linear array across the focal plane of a germanium lens in 1.4 s. The resultant image, displayed in false colors, representing temperature variation, on a color liquid crystal display, contains 120 × 120 pixels. A cursor is employed to read out the temperature at any point of the image. A removable PCMCIA memory card stores 144 images for recall and later transfer to a computer. An RS-232 port provides an interface to a personal computer. Operation is controlled by a built-in 386EX microprocessor. The specifications are listed in Table 6-6. (Description of this imaging radiometer is not meant to be a product recommendation.)

**Table 6-5.** Specifications of thermoelectric linear arrays employed in IR SnapShot® imaging radiometer. From P.W. Kruse.[32]

| | |
|---|---|
| Number of pixels | 128 |
| Number of pixels accessed | 120 |
| Pixel size (μm) | 50 |
| Number of junctions per pixel | 3 |
| Resistance at 300 K (Ohms) | 2,380 |
| Thermal response time (msec) | 12 |
| Responsivity (V/W) | 265 |
| D* (cm $\mathrm{Hz}^{1/2}$/W) | $1.7 \times 10^8$ |

**Table 6-6.** IR SnapShot® imaging radiometer specifications.

| | |
|---|---|
| Detector | 120 element linear array of uncooled thermoelectric detectors, 50-μm square pixels |
| System dynamic range | 12 bits usable with digitizing resolution of 16 bits |
| Field of view | 17.2 deg horizontal and 17.2 deg vertical |
| Lens | germanium 20 mm, F/0.8 |
| Spectral band | 8 to 12 μm |
| NETD | <0.1°C @ 30°C |
| Accuracy | 2°C or 2% of reading |
| Measurement temperature range | 0 to 350°C (custom range available) |
| Operating temperature | 0 to 40°C |
| Power input | camcorder battery |
| Image scan time | <1.5 s |
| Battery operating time | >60 min. with 3 AH battery |
| Image storage | 144 images |
| Communication | RS-232 |
| Display | active matrix color LCD |
| Video output | selectable NTSC/PAL |
| Setup menu options | emissivity, background temperature, temperature units, color palette, autoscale and fixed ranges, focus width, time, date, RS-232 baud rate, NTSC/PAL select |
| Size | 9.4 × 3.9 × 5.1 in., not including lens |
| Weight | 4.4 lbs with lens and battery |

## 6.5 Status and Trends of Uncooled Arrays

This section presents the status and technical trends of uncooled arrays, divided between those in production and under development for military and for commercial applications.

### 6.5.1 Status and trends of uncooled arrays for military systems

Table 6-7 illustrates the status and trends of uncooled arrays for military applications. Both resistive bolometers and ferroelectric bolometers are employed today for uncooled thermal imaging military systems. The arrays have 320 × 240 pixels, each 50-μm square. The NETD requirement, which is being met, is 0.1°C. The frame rate is 30 Hz in the U.S.

**Table 6-7.** Status and trends of military uncooled arrays.

**Military Requirements Emphasize High Performance**

| Status | Trends |
|---|---|
| Resistive bolometer, ferroelectric bolometer | Resistive bolometer |
| 320 × 240 pixels | 640 × 480 pixels |
|  | 160 × 120 pixels |
| 0.1°C NETD | 0.01°C NETD |
| 50 × 50-μm pixel size | 35 × 35-μm pixel size |
|  | 25 × 25-μm pixel size |
| 30-Hz frame rate | 30-Hz frame rate |

Under development are resistive bolometer arrays containing 640 × 480 pixels. The pixel size is being reduced to 25 × 25 μm; 35 × 35 μm is an intermediate objective. The NETD goal is 0.01°C for high performance applications. Lower cost/lower performance applications, such as fieldable perimeter security sensors, use 160 × 120 pixels, 50 × 50 μm, and an NETD of 0.1°C. The frame rate remains 30 Hz in the U.S.

Because the NETD depends inversely on the pixel sensitive area, it will be difficult to reduce both the pixel size and the NETD in the same array. The 640 × 480 pixel arrays will use small pixels, i.e., less than 50 × 50 μm, in order to reduce the optics cost. Thus the NETD of these larger arrays will remain at 0.1°C for the near future.

### 6.5.2 Status and trends of commercial uncooled arrays and systems

Table 6-8 illustrates the status and trends of uncooled arrays for commercial applications. The systems in use today including resistive bolometer imagers and imaging radiometers and ferroelectric bolometer imagers are derivatives of military systems and are too costly for widespread use. Imaging radiometers employing linear thermoelectric arrays operating in the snapshot mode are less costly than the TV-rate imaging radiometers employing resistive bolometer arrays.

As the commercial markets for uncooled imagers and imaging radiometers expand, and as the military environmental requirements are replaced by commercial requirements that are easier to meet, the cost of commercial systems will inevitably decrease. If the drivers' vision enhancement system market undergoes explosive growth, as appears possible, thermal imager costs will dramatically decrease.

**Table 6-8.** Status and trends of commercial uncooled arrays.

**Commercial Markets Emphasize Low Cost***

| Status | Trend |
|---|---|
| Commercial marketing of military thermal imagers | Development of new, low-cost thermal imagers and imaging radiometers |
| Overspecified for commercial applications | Designed for specific commercial applications and meeting commercial requirements |
| 320 × 240 pixel, 50 × 50 μm, bolometer arrays for thermal imagers that cost \$15,000–\$20,000, and imaging radiometers that cost \$20,000–\$50,000 | 160 × 120 pixel, 50 × 50 μm, bolometer arrays for thermal imagers which cost < \$3,000, imaging radiometers that cost < \$5,000, and drivers' vision enhancement systems that cost < \$2,000 |
| 120 × 1 pixel, 50 × 50 μm, thermoelectric arrays for imaging radiometers that cost \$15,000 | Same performance but cost \$7,500 |
| 320 × 240 pixel, 50 × 50 μm, hybrid ferroelectric bolometer array imagers for drivers' vision enhancement that cost \$2,000–\$4,000 in extremely large volumes | 160 × 120 pixel, 50 × 50 μm, bolometer arrays for drivers' vision enhancement that cost \$1,000 in extremely large volumes |

*The term "cost" refers to what the buyer pays.

## References

1. P.W. Kruse, L.D. McGlauchlin and R.B. McQuistan, *Elements of Infrared Technology*, Chapter 9, John Wiley and Sons, New York, (1962).
2. R.A. Wood, C.J. Han, and P.W. Kruse, "Integrated uncooled infrared detector imaging array," Proc. IEEE Solid State Sensor and Actuator Workshop, Hilton Head Island, SC, pp. 132-135 (1992).
3. R.A. Wood, "Monolithic silicon microbolometer arrays," in *Uncooled Infrared Imaging Arrays and Systems*, Vol. 47 of *Semiconductors and Semimetals*, P.W. Kruse and D.D. Skatrud, eds., Academic Press, New York (1997).
4. R.S. Balcerak, "Uncooled infrared sensors: rapid growth and future perspective," Proc. SPIE Vol. 4028, *Infrared Detectors and Focal Plane Arrays VI*, p. 36 (2000).
5. P.E. Howard et al., "Advances in microbolometer focal plane array technology at Boeing," Proc. SPIE Vol. 3379, *Infrared Detectors and Focal Plane Arrays V*, p. 47 (1998).
6. P.E. Howard et al., "Advanced high-performance 320×240 VOx microbolometer uncooled IR focal plane," Proc. SPIE Vol. 3698, *Infrared Technology and Applications XXV*, p. 131 (1999).
7. W. Radford et al., "Sensitivity improvements in uncooled microbolometer FPAs," Proc. SPIE Vol. 3698, *Infrared Technology and Applications XXV*, p. 119 (1999).
8. R. Murphy et al., "Recent developments in uncooled IR technology," Proc. SPIE Vol. 4028, *Infrared Detectors and Focal Plane Arrays VI*, p. 12 (2000).
9. P.W. Kruse et al., "Infrared imager employing 160×120 pixel uncooled bolometer array," Proc. SPIE Vol. 3436, *Infrared Technology and Applications XXIV*, p. 572 (1998).
10. J.L. Heath et al., "160×128 uncooled FPA performance review," Proc. SPIE Vol. 3698, *Infrared Technology and Applications XXV*, p. 256 (1999).
11. Personal communication from Infrared Solutions, Inc.
12. J.F. Brady et al., "Advances in amorphous silicon uncooled IR systems," Proc. SPIE Vol. 3698, *Infrared Technology and Applications XXV*, p. 161 (1999).
13. C. Vedel et al., "Amorphous-silicon-based uncooled microbolometer IRFPA," Proc. SPIE Vol. 3698, *Infrared Technology and Applications XXV*, p. 276 (1999).
14. E. Mottin et al., "320×240 microbolometer uncooled IRFPA," Proc. SPIE Vol. 4028, *Infrared Detectors and Focal Plane Arrays VI*, p. 40 (2000).
15. T. Ishikawa et al., "Low cost 320×240 uncooled IRFPA using conventional silicon IC process," Proc. SPIE Vol. 3698, *Infrared Technology and Applications XXV*, p. 556 (1999).

16. T. Breen et al., “Applications of uncooled microbolometer sensors,” Proc. SPIE Vol. 3379, *Infrared Detectors and Focal Plane Arrays V*, p. 145 (1998).
17. P.E. Howard, “Advances in microbolometer focal plane technology at Boeing,” Proc. SPIE Vol. 3379, *Infrared Detectors and Focal Plane Arrays V*, p. 47 (1998).
18. P.E. Howard et al., “Advanced high-performance 320×240 VOx microbolometer uncooled IR focal plane array,” Proc. SPIE Vol. 3698, *Infrared Technology and Applications XXV*, p. 131 (1999).
19. P.W. Kruse et al., “Infrared imager employing 160×120 pixel uncooled bolometer array,” Proc. SPIE Vol. 3436, *Infrared Technology and Applications XXIV*, p. 572 (1998).
20. J.L. Heath et al., “160×128 uncooled FPA performance review,” Proc. SPIE Vol. 3698, *Infrared Technology and Applications XXV*, p. 256 (1999).
21. B. Meyer and T. Hoelter, “Uncooled radiometric camera performance,” Proc. SPIE Vol. 3379, *Infrared Detectors and Focal Plane Arrays V*, p. 69 (1998).
22. C. M. Hanson, “Hybrid pyroelectric-ferroelectric bolometer arrays,” Chapter 4 in *Uncooled Infrared Imaging Arrays and Systems*, *Semiconductors and Semimetals 47*, Paul W. Kruse and David D. Skatrud, eds., Academic Press, New York (1997).
23. C.M. Hanson et al., Proc. SPIE Vol. 1735, p. 17 (1992).
24. M. Noda et al., “Simple detector pixel of dielectric bolometer mode and its device structure for an uncooled IR image sensor,” Proc. SPIE Vol. 3698, *Infrared Technology and Applications XXV*, p. 565 (1999).
25. R. Owen et al., “Producibility advances in hybrid uncooled infrared devices-II,” Proc. SPIE Vol. 2746, *Infrared Detectors and Focal Plane Arrays V*, p. 23 (1996).
26. S.B. Evans and T. Hayden, “High MTF hybrid ferroelectric IRFPA,” Proc. SPIE Vol. 3379, *Infrared Detectors and Focal Plane Arrays V*, p. 36 (1998).
27. J.F. Belcher et al., “Uncooled monolithic ferroelectric IRFPA technology,” Proc. SPIE Vol. 3436, *Infrared Technology and Applications XXIV*, p. 611 (1998).
28. R.K. McEwen and P.A. Manning, “European uncooled thermal imaging sensors,” Proc. SPIE Vol. 3698, *Infrared Technology and Applications XXV*, p. 322 (1999).
29. M.C. Foote, E.W. Jones and T. Caillat, “Uncooled thermopile infrared detector linear arrays with detectivity greater than $10^9$ cmHz$^{1/2}$/W,” *IEEE Trans. Electron Dev.* **45**, p. 1896 (1998).
30. M.C. Foote and E.W. Jones, “High performance micromachined thermopile linear arrays,” Proc. SPIE Vol. 3379, *Infrared Detectors and Focal Plane Arrays V*, p. 192 (1998).
31. T. McManus and S. Mickelson, “Imaging radiometers employing linear thermoelectric arrays,” Proc. SPIE Vol. 3698, *Infrared Technology and Applications XXV*, (1999).

32. P. W. Kruse, "Application of uncooled monolithic thermoelectric linear arrays to imaging radiometers," in *Uncooled Infrared Imaging Arrays and Systems*, P. W. Kruse and D. D. Skatrud, eds., *Semiconductors and Semimetals 47*, R.K. Willardson and E.R. Weber, eds, Academic Press, San Diego (1997).

# Chapter 7

# Choosing the Proper Technical Approach for a Given Application

## 7.1 Introduction

The user of uncooled infrared arrays and systems employing them who is unfamiliar with the technology is confronted with choosing between unfamiliar items. The purpose of this chapter is to assist in making the appropriate choice. The chapter begins with a description of thermal imaging applications. It is followed by a comparison of the principal uncooled thermal detector technologies.

## 7.2 Thermal Imaging Applications

Table 7-1 illustrates the principal thermal imaging applications as a function of three user communities, namely, military, paramilitary, and commercial. The systems can be either uncooled or cryogenic. The applications fall into four broad categories: surveillance, imaging radiometry, imaging spectroradiometry, and drivers' vision enhancement. Although drivers' vision enhancement can be considered to be a subset of surveillance, its potential market is so large that it can dominate all others; thus it is listed separately.

Surveillance refers to a very broad category of applications in which the user employs a thermal imager to view objects, personnel, buildings, terrain and so on, usually at night but sometimes during daylight. The military distinguishes between surveillance, reconnaissance, and target acquisition, but here these three functions are combined into one. Those military surveillance systems [which are frequently referred to as FLIRs (forward looking infrared)] that are listed in Table 7-1 include weapon sights; examples include those used on an individual weapon such as a rifle, or on a crew-served weapon, such as a two-person missile launcher. They also include the night sight used to acquire and engage targets for the main gun of a tank and the night sight used by a helicopter gunner to acquire and engage targets for missiles carried by the helicopter. Other FLIR examples include the thermal night vision system used by the pilot of a helicopter at night and an emerging technology of finding explosive mines, either lying on the surface of a battlefield or else buried in shallow holes.

**Table 7-1.** Thermal imaging applications.

| | Military | Paramilitary | Commercial |
|---|---|---|---|
| Surveillance | • Weapon sights individual crew-served tank main gun helicopter<br>• Helicopter pilotage<br>• Mine detection | • Border patrol/ FBI/DEA<br>• Police/sheriff<br>• Helicopters<br>• Fixed wing aircraft<br>• Squad cars | • Perimeter surveillance<br>• Warehouse interior surveillance<br>• Firefighter's helmet<br>• Firebomber aircraft |
| Imaging radiometry | • None | • None | • Predictive/preventive maintenance<br>• Quality control<br>• Process control<br>• Nondestructive testing |
| Imaging spectroradiometry | • Chemical agent detection and identification | • Narcotics detection and identification | • Quality control<br>• Process control<br>• Laboratory instrumentation<br>• Space instrumentation |
| Drivers' vision enhancement | • Tanks<br>• Armored personnel carriers<br>• Trucks | • Squad cars | • Automobiles<br>• Trucks |

Paramilitary surveillance applications in the U.S. include those carried out by the Border Patrol, the Federal Bureau of Investigation, and the Drug Enforcement Agency. Among others, these organizations protect U.S. borders against illegal immigration, illegal drug and other contraband smuggling, and other crimes against federal laws committed within the U.S. Thermal imaging systems, whether ground-based or air-based, play an increasingly important role in detecting federal law violators. At the state and local level, police and sheriffs use thermal imaging systems to detect violations of state and local laws, with hand-held, airborne, and squad-car-mounted equipment.

Commercial applications of thermal imaging surveillance systems are also emerging. They include exterior and interior surveillance of large buildings, such as warehouses, to prevent theft. An emerging application for surveillance systems is in fire fighting, enabling fire fighters to see through smoke, whether viewed from airborne platforms searching for forest fires or hand-held or helmet-mounted applications by fire fighters searching for occupants of burning buildings. The hand-held and helmet-mounted applications are unique to uncooled thermal imaging systems.

All of these surveillance applications require that the user be able to obtain a thermal image of a scene at night or through smoke. The other major category of thermal imaging surveillance systems is drivers' vision enhancement. Whether the application is military (tanks and other military vehicles), paramilitary (squad cars) or commercial, this application is largely filled by uncooled thermal imaging systems. Although the present military market is large and growing, it is the commercial market that will be the dominant application of uncooled thermal imaging equipment. In the U.S., the Cadillac Division of General Motors has pioneered this application, selling thermal imagers to the customer for just under $2000. (This price may increase because the manufacturing cost now is higher than $2000.) The worldwide market is enormous, but the retail price must be very low. Thus the unit profit is small and the risks are large.

Radiometry refers to measuring the temperature of an object by its thermal emittance. Imaging radiometry refers to measuring the temperature at all points within a scene by means of the thermal emittance from those points. There are no uniquely military and paramilitary applications of imaging radiometry. However, the commercial markets, including predictive and preventive maintenance, quality control, process control, and nondestructive testing, are increasing rapidly. The key to rapid market growth is uncooled thermal imaging with its substantially lower cost than cryogenic systems. In general, imaging radiometer systems require more complex hardware and software than thermal imaging surveillance systems. Although the focal plane arrays are essentially the same, the radiometric systems require calibration of the output of every pixel with respect to the target scene temperature and the ambient imaging radiometer temperature. That calibration either must remain unchanged for months or years, or the imaging radiometer must have an internal means of automatic recalibration of every pixel. Furthermore, the dynamic range of scene temperature measurement must be very large and the error in temperature measurement must be very small. Finally, the cost to the final user must be sufficiently low so as to allow sufficient market volume. Here again, uncooled thermal imagers have an opportunity to dominate over cryogenic systems.

The final application is imaging spectroradiometry, technically the most complex of all the applications. Here it is necessary to measure the absolute spectral radiant emittance, i.e., the radiant emittance within selected wavelength bands within a scene. Therefore the thermal imaging radiometer must possess the capability of dividing the radiant emittance of a scene into selected wavelength bands by means of a prism, grating, filters, or other means. Every spectral band over the entire wavelength band must be radiometrically calibrated and must also meet all the other requirements imposed on a thermal imaging radiometer.

The market for imaging spectroradiometers is small relative to that for imaging radiometers. Other than the detection and identification of chemical warfare agents, there is no other military application. Detection and classification of narcotics is a potential paramilitary application. Commercial applications include spaceborne imaging radiometry, and industrial process control and quality control. There are also miscellaneous chemical laboratory applications. These systems, especially spaceborne systems, can be very costly.

## 7.3 Comparison of the Principal Types of Uncooled Thermal Detectors

Table 7-2 compares the performance and availability of five classes of uncooled thermal detectors, including resistive bolometers, monolithic pyroelectric detectors, hybrid pyroelectric detectors, hybrid ferroelectric bolometers (also known as hybrid bias-enhanced pyroelectric detectors), and thermoelectric detectors. The performance parameters include responsivity, whether electrical bias is required, whether a dc frequency response can be obtained, whether a radiation chopper is required (true only if there is no dc response), the response time expressions, the dynamic response linearity, i.e., the magnitude of the region over which the output signal is linear with input radiant power, and the suitability for use in an imaging radiometer or spectroradiometer. The final three items describe whether arrays are commercially available, the production status of the array, and the possibility of performance improvement.

All of the values shown in this matrix reflect the current status. Four of the parameters, including "bias required," "dc response," "chopper required," and "response time" are factual; the others are judgmental. They reflect the following views of the author:

- Of the five types of detectors shown, the hybrid pyroelectric/ferroelectric bolometer detector was the first to enter production, and is the most widely used type.
- On the other hand, there is little or no room for improvement in the performance (NETD) of the hybrid pyroelectric/ferroelectric bolometer detector because the thermal conductance between the detecting material and the silicon substrate through the bump interface already limits the performance to the temperature fluctuation noise limit.
- The hybrid ferroelectric bolometer detector also requires a radiation chopper because it has no dc response. This is a potential drawback in applications that require no moving parts.
- There are only two major manufacturers of hybrid ferroelectric bolometer detectors, one in the U.S. and one in the U.K.
- The hybrid pyroelectric detector is not commercially available. It appears unlikely that it will be, since it suffers from the same thermal conductance and chopper problems as the hybrid ferroelectric bolometer detectors, yet has a lower responsivity.
- The monolithic pyroelectric detector technology overcomes the performance limit of the hybrid approach, but there is little development effort under way. Like the hybrid pyroelectric detector, it requires a radiation chopper.

Table 7-2. Comparison of principal types of uncooled thermal detectors.

| | **Monolithic resistive bolometer** | **Monolithic pyroelectric detector** | **Hybrid pyroelectric detector** | **Hybrid ferroelectric bolometer** | **Monolithic thermoelectric detector** |
|---|---|---|---|---|---|
| Responsivity | High | High | High | High | Low |
| Bias required | Yes | No | No | Yes | No |
| DC response | Yes | No | No | No | Yes |
| Chopper required | No | Yes | Yes | Yes | No |
| Response time | C/G** | C/G***, $rC_e$*** | C/G***, $rC_e$*** | C/G***, $rC_e$*** | C/G* |
| Dynamic range linearity | High | Unknown | Low | Low | High |
| Radiometric capability | Excellent | Unknown | Poor | Poor | Excellent |
| Array availability | Yes | No | No | Yes | Yes |
| Production status | Medium | No | No | High | Medium |
| Possibility of performance improvement | High | High | Low | Low | Medium |

| | |
|---|---|
| * | See Chapter 3 |
| ** | See Chapter 4 |
| *** | See Chapter 5 |

- It seems likely that monolithic resistive bolometer technology will become dominant in the near future and will remain so into the foreseeable future. It does not require a radiation chopper and it has a very low thermal conductance, therefore a high responsivity and a low NETD. There is room for growth in the selection of new bolometric thin films that have a higher temperature coefficient of response than the standard vanadium oxide, such as the emerging amorphous hydrogenated silicon. Furthermore, changes in the shape of the legs of the monolithic construction allow trade-off between speed of response and noise equivalent temperature difference.
- Monolithic thermoelectric arrays find application in imaging radiometers, where their intrinsic linearity over a very wide dynamic range makes calibration easier than that of monolithic resistive bolometers. However, only linear arrays are commercially available, and only in limited quantities. Thus, at present a two-dimensional image can only be formed by scanning the linear array over the scene. Their simplicity of calibration means that the selling price of imaging radiometers based upon linear thermoelectric arrays should remain less than those based on two-dimensional resistive bolometer arrays. However, because of the need for one-dimensional scanning, imaging radiometers employing thermoelectric arrays today do not operate at TV frame rates, whereas those employing monolithic resistive bolometer arrays do.

# Index

Applications
  commercial, 84
  military, 83
  paramilitary, 84

Comparison of principal types of uncooled thermal detectors, 86

Detection mechanisms
  photon, 2
  thermal, 4
  wave interaction, 6

Figures of merit: definitions
  detectivity D*, 7
  electrical response time, 53
  minimum resolvable temperature difference, 9
  noise equivalent power, 7
  noise equivalent temperature difference, 8
  responsivity, 7
  thermal response time, 9

Fundamental limits
  background fluctuation noise, 11, 20
  temperature fluctuation noise, 14, 20

Heat flow equations
  Case I: unbiased, 27, 34, 61
  Case II: continuous bias, 35
  Case III: pulse bias, 40

Noise
  background fluctuation, 12, 20
  Johnson, 30, 42, 54
  1/f power law, 42
  temperature fluctuation, 14, 20, 43, 55

Pixel structure
  monolithic, 27, 33, 50, 58
  hybrid, 68

Pyroelectric and ferroelectric bolometer arrays
  hybrid ferroelectric bolometer arrays, 67
  monolithic pyroelectric arrays, 49, 72

Resistive bolometer arrays
  materials, 45, 64
  theory, 33

State-of-the-art
  ferroelectric bolometer imager, 67
  resistive bolometer imagers, 57
  thermoelectric imaging radiometer, 75

Technical trends
  commercial, 78
  military, 77

Thermal detector comparison, 86

Thermoelectric arrays
  materials, 32
  theory, 25

**Paul W. Kruse with his wife, Margaret.**

Paul W. Kruse received his PhD in Physics from the University of Notre Dame in 1954. Most of his career has been spent at the Honeywell Technology Center where he was Chief Research Fellow prior to his retirement in 1993. He then became a founder and Chief Scientist of Infrared Solutions, Inc. He has now retired from Infrared Solutions and is a consultant on infrared technology. He has more than 45 years experience in the development of detectors and focal plane arrays including not only those based on photon effects, but also uncooled thermal effects. In addition to being the author of Uncooled Thermal Imaging Arrays, Systems, and Applications, he is the co-author of Elements of Infrared Technology, co-editor of Uncooled Infrared Imaging Arrays and Systems, and author of more than 100 other scientific publications. He is a Fellow of the American Physical Society and the Optical Society of America.

# UNCOOLED THERMAL IMAGING

## Arrays, Systems, and Applications

Paul W. Kruse

The development of uncooled infrared focal plane arrays can be traced to the military need to see the battlefield at night without the need for any form of illumination, whether from natural sources (moonlight, starlight, airglow) or from artificial sources. While the early arrays involved use of cryogenic systems, a new class of detection mechanism that didn't require cryogenic operation was developed in the United States in the 1980s.

Paul W. Kruse has been involved in the evolution of this technology since that time, and his Tutorial Text provides an introduction to the subject for both professionals and students.

*Uncooled* refers to arrays that are operated without any type of cryogenic system. *Infrared focal plane array* refers to an assemblage of individual infrared detector picture elements ("pixels") located at the focal plane of an infrared imaging system. Building on these key elements, Kruse covers topics including uncooled thermal detection mechanisms; fundamental performance limits; theoretical performance of thermoelectric, resistive bolometric and pyroelectric detection mechanisms; state-of-the-art of uncooled arrays, imaging systems, and applications and trends.

SBN 978 0 8194 4122 5
90000
9 780819 441225

SPIE

P.O. Box 10
Bellingham, WA 98227-0010

ISBN-10: 0819442118
ISBN-13: 9780819441225
SPIE Vol. No.: TT51